이학박사 학위논문

Observation of the resonance-assisted dynamical tunneling in a deformed microcavity

변형된 미소 공진기에서 공진 사슬에 의한 동적 터널링 관측

2013년 8월

서울대학교 대학원

물리·천문학부

곽 호 정

Observation of resonance-assisted dynamical tunneling in a deformed microcavity

by

Hojeong Kwak

A Dissertation Submitted in Partial Fulfillment of the Requirements for the Degree of

Doctor of Philosophy
(Physics and Astronomy)
at the
Seoul National University

Abstract

The interaction among the unperturbed-basis modes is a main feature of the non-integrable Hamiltonian system. So, the interaction has attracted a lot of interests and has been studied in a deformed microcavity system. However, the previous researches have mainly focused on the outcomes of the interaction. In this thesis, we try to apply the resonance-assisted dynamical tunneling (RADT) theory to a deformed microcavity for understanding the unperturbed-basis mode interaction.

The interactions in an asymmetric cavity can be qualitatively classified into two kinds of interactions by the coupling strength, strong interactions and weak interactions. For strong interactions, the Husimi functions of the interacting unperturbed-basis modes at the closest encounter are strongly localized along the stable or the unstable periodic orbit on the phase space. It implies that the strong interaction is related to the RADT. Also, the difference between the angular mode indices of the unperturbed basis modes is the integer multiple of the number of the island of the non-linear resonance structure on the PSOS. This *selection rule* is one of the predictions of the RADT theory.

The RADT theory also predicts that the coupling strength of the interaction related to the RADT is proportional to the square of the phase space area associated with the non-linear resonance structure. We experimentally confirmed this prediction. For this purpose, the AC gaps between $l = 2$

and $l = 3$ modes as varying the cavity deformation are experimentally measured using the cavity-modified fluorescence spectroscopy, exploiting the continuously deformation tunable liquid jet cavity. Additionaly, using the numerical method, we found that the coupling strength of the resonance-assisted interaction related to the identical non-linear resonance structure on the phase space is proportional to the size parameter.

Key Words : deformed microcavity; liquid jet cavity; phase space structure; resonance-assisted dynamical tunneling; unperturbed mode interaction;

Contents

List of Figures

List of Tables

Chapter 1

Introduction

For a decade, optical microcavities have attracted a lot of interests for the various applications due to the high-Q factor and its small size [1, 2, 3, 4, 5, 6, 7, 8]. Additionally, dielectric optical resonators are prominent tools for studying the correspondence between the classical phase space structure of the underlying system and the wave mechanical mode characteristics. Specifically, the directionality is effected by the phase space structure. The existence of the stable island near the critical line modifies the output directionality, called as "dynamical eclisping" [9, 10]. Also, the universal directionality was observed [11, 12], which is the manifestation of the unstable manifold structure near the critical line.

It is well known that the dynamical tunneling, which is the tunneling between modes localized on the classically seperated regions, is influenced by the underlying phase space structure. The prominent example is the chaos-assisted tunneling. The modes localized on the symmetry-related regular region in the chaotic sea can be coupled strongly to the mode on the

other regions assisted by the chaotic modes spread over the chaotic region [13, 14, 15]. The chaos-asssited tunneling is experimentally studied in cold atom systems [16, 17] and a microwave cavity [47]. In optical microcavities, it is theoretically studied [18] and the chaos-assisted decay is experimentally observed [19, 20].

Also, the non-linear resonance structure can enhance the tunneling between modes localized along the invariant tori. In an integrable multidimensional system, classical trajectories appear as invariant tori on the Poincarè surface of section (PSOS). The phase-space projections of quantum eigenstates are then localized along these tori. In the presence of perturbation, invariant tori are deformed following the Kolmogrov-Arnold-Moser (KAM) scenario and some orbits evolve into a *chain*-like nonlinear resonance structure qualitatively distinguished from the KAM tori. The nonlinear resonance structure can then strongly enhance a tunneling process between the modes localized along nearby invariant tori when specific conditions are satisfied. This type of enhanced dynamical tunneling is known as the resonance-assisted dynamical tunneling (RADT) [39, 40].

RADT is a universal phenomenon occurring in any weak-perturbed systems of near-integrable or mixed phase space since the theory of RADT does not depend on the details of the Hamiltonian. RADT has thus been theoretically studied in various systems such as periodic-driven pendula [41], Rydberg atoms under periodic perturbation [42], quantum accelerator modes [43] and multidimensional molecules [44, 45]. RADT has also been extensively studied in one-dimensional time perodic qunatum maps such as the kicked Harper model and the kick rotor [38, 39, 46, 49, 50]. However,

the RADT is not studied in an optical microcavity system and to the best of our knowledge, there exist no experiments yet confirming the prediction of the RADT theory.

In this thesis, we apply the RADT theory to a mircrocavity system. This gives the underlying semiclassical origin of the interactions between unperturbed modes. Also, the RADT theory is experimentally confirmed by the avoided-crossing (AC) gap measurement. The thesis consists of following chapters.

Chapter 2 gives the introduction of an asymmetric microcavity. At first, the general properties of optical microcavities are introduced and the properties of circular cavity is briefly explained. Then, the numerical tools for studying a deformed microcavity are introduced such as the PSOS for studying the underlying classical phase space structure and the boundary element method (BEM) for numerically calculating the eigenvalues and the eigenvector of a mocricavity. Also, the experimental tool, the dye doped ethanol jet system is reviewed. In chapter 3, we review the RADT theory. The semi-classical perturbation theory for multi-dimensional systems is studied and from the result, the RADT theory is derived following the standard secular perturbation theory. The RADT theory gives two predictions, the selection rule and the phase space structure dependence of the coupling strength between unperturbed-basis modes.

In chapter 4, we apply the RADT theory to our optical microcavity. At first, it is found that strong interactions are related to the non-linear resonance structure, Then, for these interactions, we can confirm that the angular mode index difference is an integer multiple of the number of the

island in the associated non-linear resonance structure and the coupling strength is proportional to the square of the area of the non-linear resonance chain from the experiment and the numerical calculation. In chapter 5, we discuss the proportionality constant between the coupling strength and the phase space area. Also, we study how to deriving the AC gap of higher order interactions and how to reconstructing the interaction Hamiltonian.

In appendix B, although not being directly related to a deformed microcavity, an acoustic cavity is introduced. By using the schlieren method, which uses the refraction of collimated light passing through a transparent medium with its refractive index spatially modulated, the spatial mode distribution in a ultrasonic cavity can be visualized non-destructively. Exploiting this method, the interactions between 'inner' modes and 'shell' modes are studied in a circular shell acoustic cavity.

Chapter 2

Deformed optical microcavity

2.1 Microcavity

2.1.1 Whispering gallery type microcavity

Cavity resonators are fundamental components for optical applications, such as lasers and amplifier. The most widely used optical resonator is Fabry-Perot type, Fig. 2.1(a). Two opposite mirrors are metal coated and confine the light between themselves. The quality factor of the confined light is determined by the reflectance of the coated mirrors and the absorption of the intervening medium. It is very important to reduce resonators size and the increase the mode Q-factor for optoelectronic applications and QED study, but it is very hard to reach these condition for the Fabry-Perot resonator.

Another types of cavities employ the total internal reflection at the interface between two different dielectric medium. The light of incident angle above the critical angle can only leak out by the tunneling due to the cavity

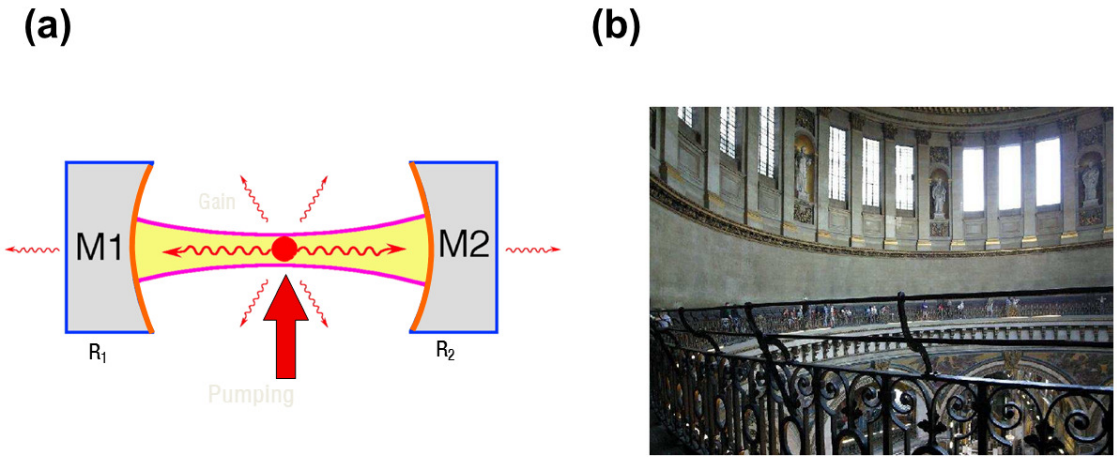

Figure 2.1: (a) Fabry-Perot Type resonator. Each mirror, M_1 and M_2, is coated by metal of reflectance R_1 and R_2. (b) Whispering gallery in St. Paul Cathedral in London.

boundary curvature. This type of resonators is called as whispering gallery type resonators named after the acoustic wave studied by Lord Rayleigh [21]. Two people at the opposite position close to the wall can communicate with each other through whisper in the gallery of the St. Paul's Cathedral in London 2.1(b). The sound from one can be transmitted to other by repeated reflections along the smooth curved wall of the gallery. These resonator can be manufactured small and the confined modes can maintain the high Q-facotor.

2.1.2 Wave equation for a microcavity

The whispering gallery modes in a microcavity can be studied by solving the Maxwell's equations. If the cavity of the refractive index n_1 is surrounded by the medium of refractive index n_2 ($n_2 < n_1$), the Maxwell's equations can be written as

$$\nabla \times \boldsymbol{E}_j + \frac{\partial}{\partial t}\boldsymbol{B}_j = 0 \qquad \nabla \cdot \boldsymbol{D}_j = 0 \tag{2.1}$$

$$\nabla \times \boldsymbol{H}_j + \frac{\partial}{\partial t}\boldsymbol{D}_j = 0 \qquad \nabla \cdot \boldsymbol{B}_j = 0 \tag{2.2}$$

where the subscript $j = 1$ ($j = 2$) means the inside (outside) the cavity [22].

Assuming the harmonic time dependence $\exp(iwt)$ and combining two equations for a homogeneous dielectric medium of the refractive index n we can derive the Helmholtz equatins,

$$\nabla^2 \boldsymbol{E}_j(\boldsymbol{r}) + n_j^2 k^2 \boldsymbol{E}_j(\boldsymbol{r}) = 0 \tag{2.3}$$

$$\nabla^2 \boldsymbol{B}_j(\boldsymbol{r}) + n_j^2 k^2 \boldsymbol{B}_{j(\boldsymbol{r})} = 0 \tag{2.4}$$

where k is the wavevector given by w/c.

For simplicity, we assume that the fields are independent on z, that is the conserved z-component momentum $k_z = 0$. Then, B_z and E_z fields are not mixed with each other. It is called as transverse magnetic (TM) field when $B_z = 0$ and transverse electric (TE) field when $E_z = 0$. In this condition, the system can be considered as the effective 2D system and the above equations can be described by the scalar equations,

$$\nabla^2 \psi_j(x, y) + n^2 k^2 \psi_j(x, y) = 0 \tag{2.5}$$

where $\psi(x, y)$ is the electric field (magnetic field) for the TM (TE) polarization [23, 24]. Also, the boundary conditions are given at the interface between two media,

$$\psi_1(x, y) = \psi_2(x, y) \tag{2.6}$$

and

$$\frac{\partial \psi_1}{\partial \nu} = \frac{\partial \psi_2}{\partial \nu} \tag{2.7}$$

for TM polarization or

$$\frac{1}{n_1^2}\frac{\partial \psi_1}{\partial \nu} = \frac{1}{n_2^2}\frac{\partial \psi_2}{\partial \nu} \tag{2.8}$$

for TE polarization, where ν means the boundary normal.

Applying the outgoing boundary condition, the general solution for the scalar vector can be expressed as,

$$\psi_1(r, \theta) = \sum_{m=-\infty}^{\infty} A_m J_m(kr) \exp(im\theta) \tag{2.9}$$

$$\psi_2(r, \theta) = \sum_{m=-\infty}^{\infty} B_m H_m^{(1)}(kr) \exp(im\theta) \tag{2.10}$$

where $J_m(kr)$ is the first kind Bessel function, $H_m^{(1)}(kr)$ is the first kind Hankel function, A_m's and B_m's are the unknown expansion coefficients and (r, θ) is the cylindrical coordinate. The resonant states are determined by finding the expansion coefficients satisfying the above boundary conditions.

2.1.3 Circular microcavity

For a circular cavity, the eigenstate can be simply described as

$$\psi_j(r, \theta) = \Phi(r) \exp(\pm im\theta) \tag{2.11}$$

where $\Phi_1(r) = J_m(kr)$ and $\Phi_2(r) = H_m^{(1)}(kr)$. The angular mode index m is proportional to the angular momentum up to the planck constant $\hbar$, and is equal to the half of the intensity node of the spatial mode distribution along the boundary. For the given m, we can rewritten eq. (2.5) in terms of the radial coordinate of the cylindrical coordinate,

$$\frac{d^2\Phi(r)}{dr^2} + \frac{1}{r}\frac{d\Phi(r)}{dr} + [n^2k^2 - (\frac{m^2}{r^2})]\Phi(r) = 0. \tag{2.12}$$

For the given angular mode number, k satisfying the boundary condition is an eigenvalue and by applying that k to eq. 2.11, the radial solution can be derived. For $\Phi_1(r)$, the intensity node of the spatial distribution along the radial direction is referred to the radial mode number l (fig. 2.2). So, the eigenvalue and the eigenstate are parametrized by two mode index l and m.

The eigenstates of a circular comprise the complete set of the 2D system, so any general solution for the arbitrary boundary shape can be constructed by superposing circular states such as eq. (2.10). On the other hand, while the cavity boundary becomes slightly deformed from the circle, the eigenstate also change from the eq. (2.11) to the eq. (2.10), but the (l, m) state remains dominantly.

2.1.4 Analogy between quantum mechanics and electrodynamics

Both the electric (magnetic) field of the Maxwell equation and the quantum mechanical wave function of the time-dependent Schrödinger equation can

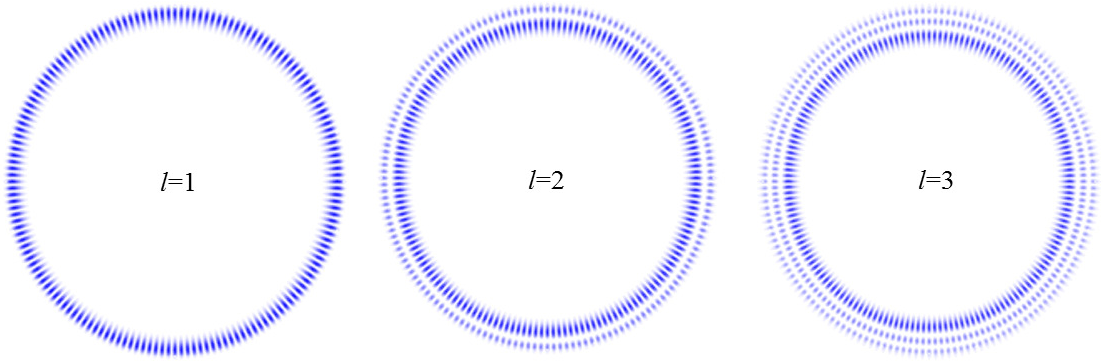

Figure 2.2: Eigenstates of a circular cavity for $m = 80$. The radial mode number l is the number of the intensity maximum.

be described by the Helmholtz equation. The similarity becomes clear by comparing the eq. 2.12 with the radial Schrödinger equation describing the wave equation of a particle under a position dependent potential,

$$-\frac{\hbar^2}{2\mu}\left(\frac{d^2\Phi(r)}{dr^2}+\frac{1}{r}\frac{d\Phi(r)}{dr}-\frac{m^2}{r^2}\Phi(r)\right)+V(r)\Phi(r)=E\Phi(r), \tag{2.13}$$

where μ is the reduced mass of a particle, $V(r)$ is a potential and E is the total energy [25, 26].

Then, by replacing the energy $\frac{2\mu}{\hbar^2}=k^2$ and the potential $\frac{2\mu}{\hbar^2}=k^2(1-m^2)$, we can find the eq. (2.12) from the eq. (2.13), that is, the electric (or magnetic) field and the matter wave function are described by the identical equation. From this, WGMs in a microcavity can be considered as eigenstates of a Schrödinger equation under the potential. Also, we can define

the effective potential as

$$V_{eff}(r) = k^2(1 - n^2) + \frac{m^2}{r}, \tag{2.14}$$

the sum of the potential and the centrifugal potential with rescaling $\frac{\hbar}{2\mu} = 1$. Then, WGMs are thought as the bounded stated of the effective potential of the given m. The ith excited bound state corresponds to the WGM of the radial mode number $l = i+1$ and the angular mode m. However, unlike the quantum mechanics, the effective potential of a microcavity is dependent of the total energy $E \sim k$.

Fig. 2.3 shows the effective potential of a circular microcavity in air, where the refractive index is a constant n in $r = a$ for the cavity radius a and $n = 1$ outside the cavity. In the figure, we define the unit length equal to the radius, as a result $a = 1.0$. Also, for the given m, bound modes of several l are plotted. The bound states can be formed in the classically allowed region enclosed by the effective potential and can escape through the classically forbidden barrier. It corresponds to the evanescent leakage of WGMs in a dielectric mircrocavity.

2.2 Deformed microcavity

For a circular 2D cavity, there exist two conserved quantities, the angular momentum and the total energy. Eigenstates of a circular cavity can be described by using two mode indices and the corresponding classical dynamics is trivial. However, as the cavity boundary shape becomes deformed,

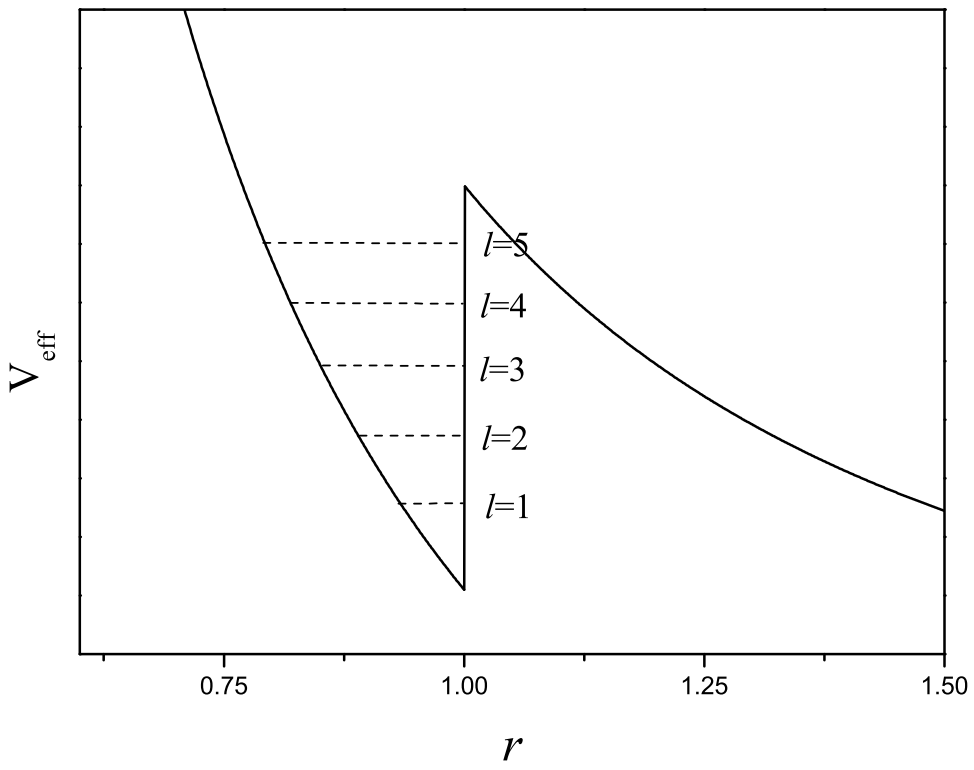

Figure 2.3: Effective potential and excited states corresponding to several radial mode orders for given m.

the underlying classical dynamics is complicated and the physics gets more fruitful.

In our system, a liquid jet cavity, the boundary of the 2D cross section can be approximated as the quadru-octapole in terms of the polar coordinate such as

$$r(\theta) = a(1 + \eta \cdot \cos 2\theta + 0.42 \cdot \eta^2 \cos 4\theta). \tag{2.15}$$

where η is the deformation parameter. The analytic solution such as eq. 2.11 does not exist and the angular momentum is not reserved in this boundary shape, so we need to survey new methods for inspecting a quadru-octapolar microcavity.

In this section, we introduce numerical tools for studying a deformed micrcaovity. Using these methods, we briefly examine the characteristics of an asymmetric cavity.

2.2.1 Poincaré surface of section

To study a system in the semiclassical limit is sometimes very useful to reveal the underlying physics picture. The classical limit of the electromagnetic wave in a deformed microcavity is the ray dynamics in a billiard system. A useful tool to study the classical phase space structure is the PSOS [27]. For a 2D conservative system, the phase space is described by 4 quantity (q_1, q_2, p_1, p_2) and the constant energy E can be written as

$$E = H(q_1, q_2, p_1, p_2). \tag{2.16}$$

Then, we can write one of the momenta as $p_2 = p_2(q_1, q_2, p_1, E)$, and the trajectories are restricted to 3D surface in the 4D phase space. If we make

the plot of the trajectory for constant q_2, the motion will be described on a 2D section in terms of (q_1, q_2), so called as *surface of section*. The motion on the PSOS can be considered as the discrete map, $(q_1, p_1) \to (q_1', q_2')$.

To plot the PSOS for a deformed microcavity, we defined the *Borkhoff coordinate* as $(q_1, p_1) = (s, \sin\chi)$ where s is the normalized arclength along the boundary from the major axis and χ is the boundary incident angle at the bouncing point related to the tangential component of momentum or the *local angular momentum* (Fig. 2.4). The Birkhoff coordinate of the ray at the bouncing position is recorded on the PSOS and by assuming the ray is reflected satisfying the Fresnel's law, the Birkhoff coordinate at the next bouncing position is subsequently recorded. By varying the initial incident angle and the incident position and iterating the reflection, we can plot the whole PSOS for a given boundary shape. In Fig. 2.4, the PSOS for the quadru-octapolar cavity of $\eta = 0.19$ is plotted. In the PSOS, we can find one of KAM tori and the phase space structure corresponding to a period-4 orbit, a period-6 orbit and a chaotic sea.

Until now, the PSOS is considered in the semiclassical limit where the sizeparameter $ka \to \infty$. However, while the size parameter has the finite value, it is well known that the outgoing ray position at the bouncing point is displaced compared to the incident position called as Goos-Hänschen shift [28, 55]. The displacement δs by Goos-Hänschen shift for a TM polarized plane wave at the boundary between dielectric media is given by [29]

$$k\Delta s = Re\left(\frac{2}{\sqrt{n^2\sin^2\chi - 1}}\frac{\sin\chi}{\sqrt{1-\sin^2\chi}}\right). \tag{2.17}$$

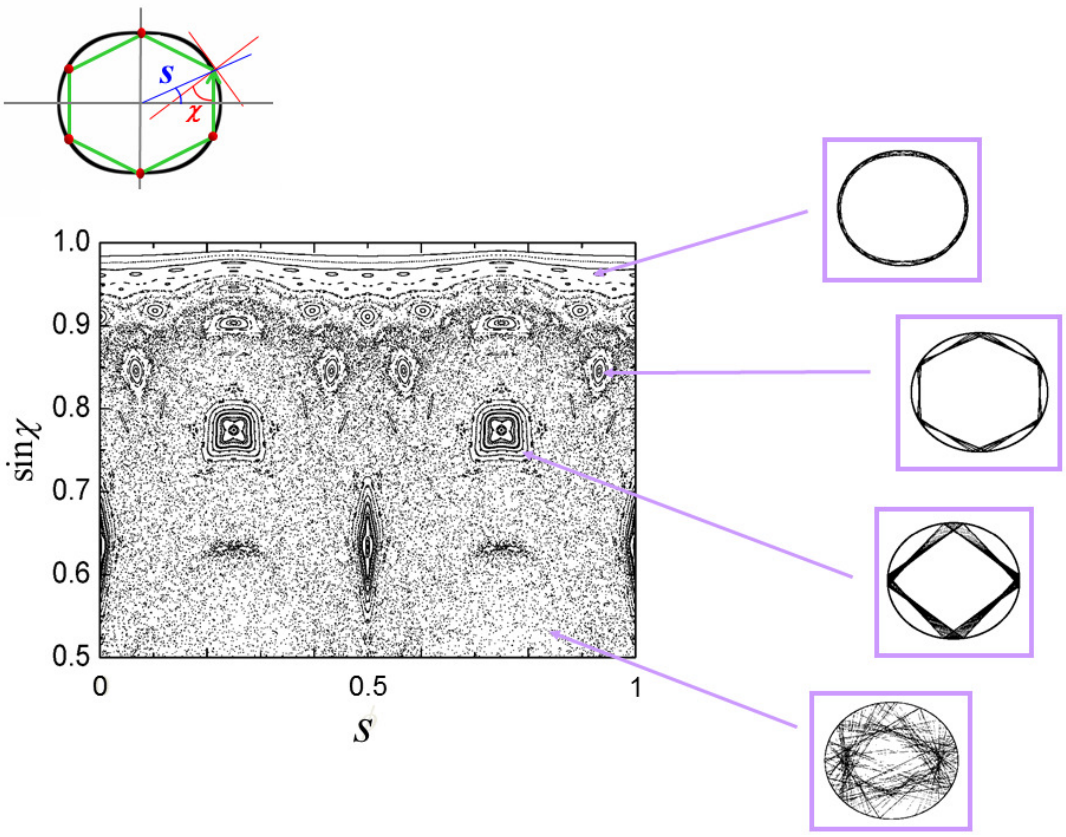

Figure 2.4: Birkhoff coordinate and the PSOS for the quadru-octapolar boundary of $\eta = 0.19$.

From this equation, we can confirm that when $k \to \infty$, $\Delta s \to 0$ as expected. Also, near the critical angle $\sin \chi_c = 1/n$, the $k\Delta s$ diverges. However, the singularity disappear because the incoming wave has the finite extension [55].

Applying the Goos-Hänschen shift, the discrete PSOS map, $T(s_j, \sin \chi_j) = (s_{j+1}, \sin \chi_{j+1})$ should be combined with the map G

$$G(s_j, \sin \chi_j) = (s_j + \Delta s(k, \sin \chi_j), \sin \chi_j), \tag{2.18}$$

then, the map $GT(s_j, \sin \chi_j) = (s_{j+1}, \sin \chi_{j+1})$ gives the modified ray optics.

The result of the modified ray optics is in Fig. 2.5(b). In the figure, the phase space structure is 'lifted' and compressed as the size parameter decreases. It is because the incident angle for the corresponding trajectory increases due to the Goos-Hänschen shift and the Δs increases while $\sin \chi$ decreases approaching to the critical angle. So the phase space structure area increases as the sizeparameter increases.

Fig. 2.6 shows the evolution of the phases space structure as varying the cavity deformation. For a circular boundary $\eta = 0.00$, invariant tori are just horizontal line implying the angular momentum conservation. As deforming the cavity boundary, non-resonant tori become curved lines following the KAM scenario, but the chain-like structures arise near resonant tori. While the cavity boundary shape becomes more deformed, the chaotic

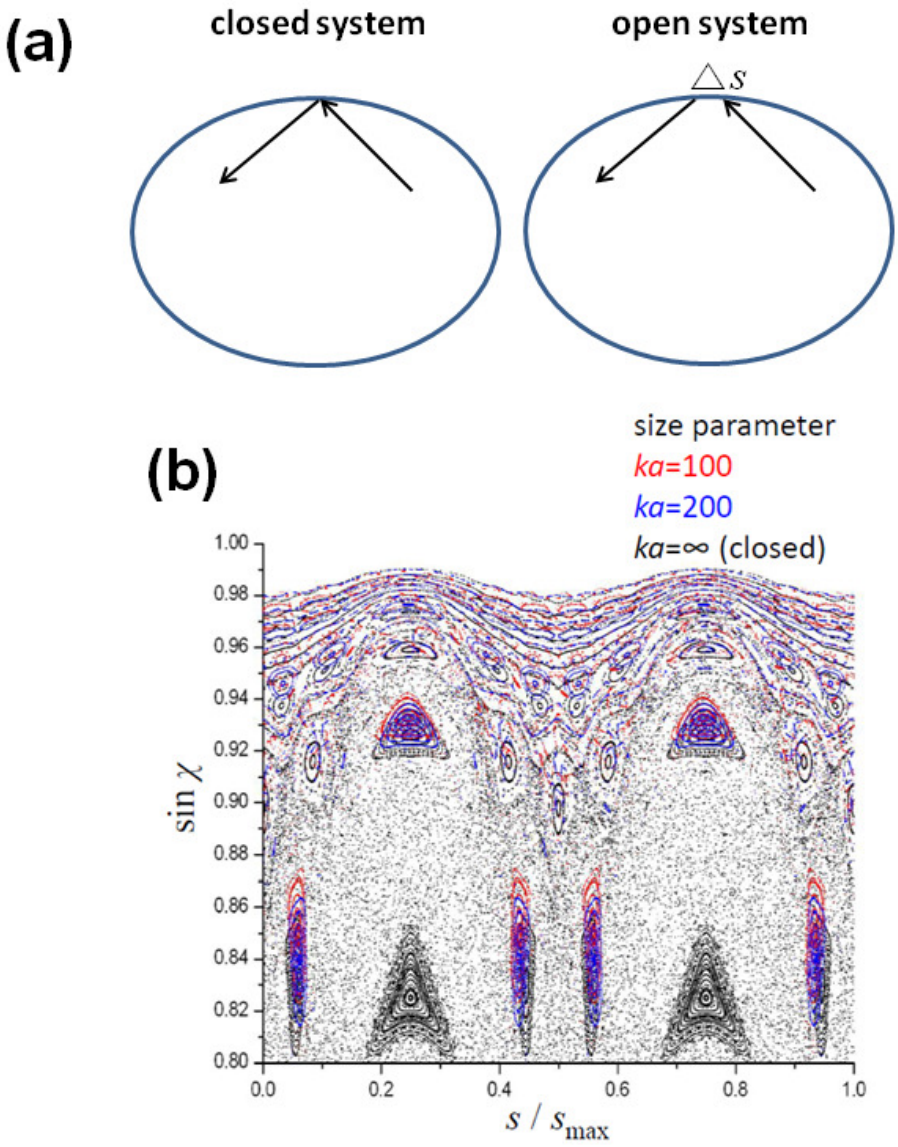

Figure 2.5: (a) The Goos-Hänschen shift at the boundary (b) The PSOS as the sizeparameter varies.

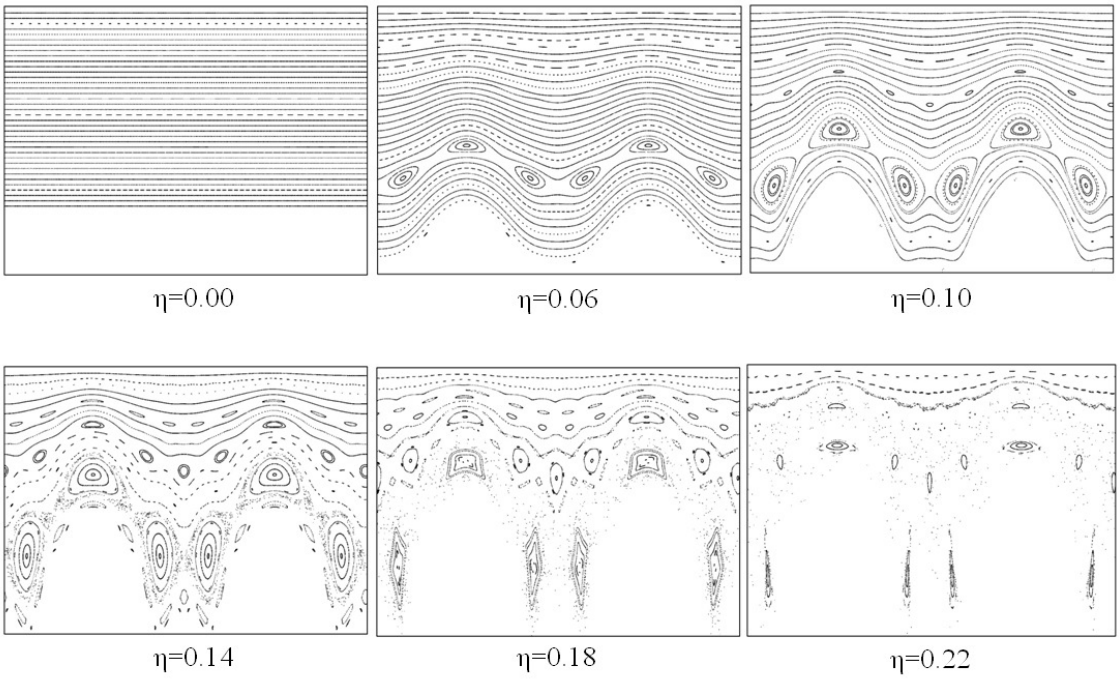

Figure 2.6: Phase space structures as varying the deformation parameter of a quadru-octapolar cavity.

structure appears near the separatrices in the resonance chain structure and the chaotic sea becomes broader with the increasing deformation parameter. Above the critical deformation, all the phase space might be filled with the chaotic sea.

2.2.2 Boundary element method

The eigenstates in a deformed cavity are not the analytic function. Generally, to derived the wave function needs to use numerical methods. The microcavity in our consideration can be described in the configuration of two homogeneous media separated by the cavity boundary. In this case, the useful method for finding the resonances is the boundary element method (BEM) [30]. The BEM reduces the 2D differential equation problem eq. (2.4) to the 1D integral equation, so the computing time decreases drastically.

For using the BEM, we need to introduce the Green's function which is defined as

$$(\nabla^2 + n_j^2 k^2) G(\boldsymbol{r}, \boldsymbol{r'}; k) = \delta(\boldsymbol{r} - \boldsymbol{r'}) \tag{2.19}$$

where $\delta(\boldsymbol{r} - \boldsymbol{r'})$ is the Dirac delta function in the two dimension and $\boldsymbol{r}$ and $\boldsymbol{r'}$ are arbitrary position vector in S_j (Fig. 2.7) . Then, by subtracting the eq.(2.19) multiplied by the wave function $\psi(\boldsymbol{r})$ from the eq. (2.5) multiplied by the Green function, we can find,

$$\psi(\boldsymbol{r})\delta(\boldsymbol{r} - \boldsymbol{r'}) = \nabla[\psi(\boldsymbol{r})\nabla G(\boldsymbol{r}, \boldsymbol{r'}; k) - G(\boldsymbol{r}, \boldsymbol{r'}; k)\nabla\psi(\boldsymbol{r})]. \tag{2.20}$$

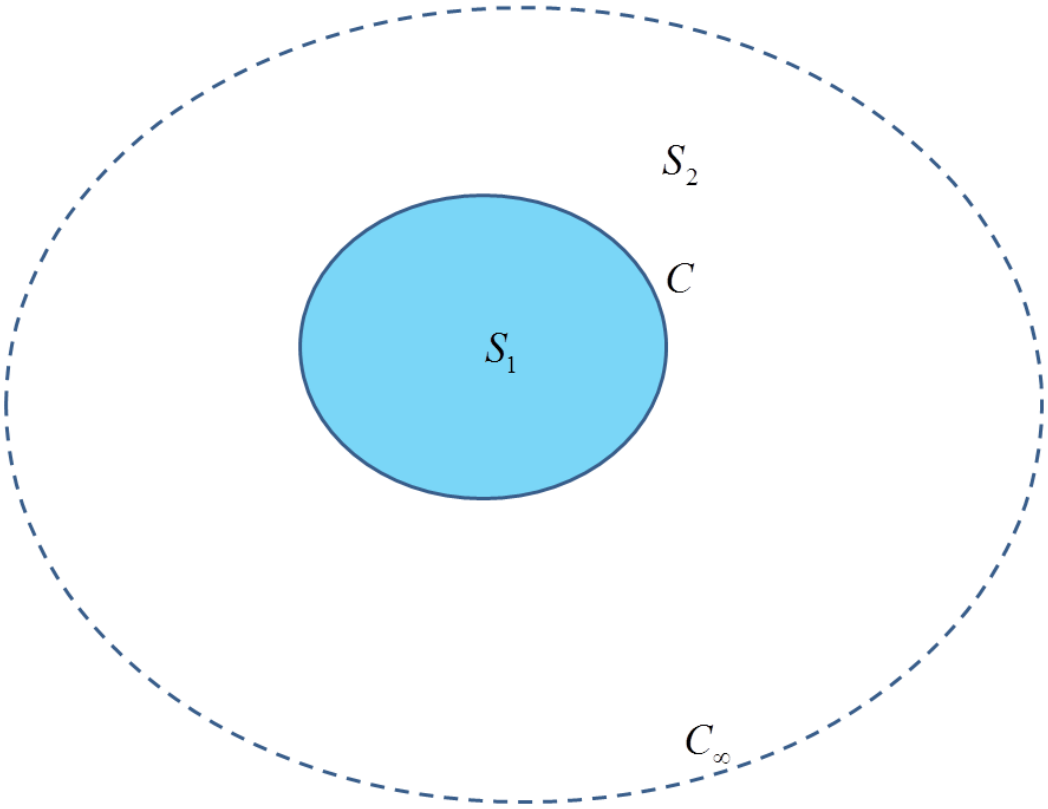

Figure 2.7: The schematic view of a microcavity for the boundary integral equation. S_1 and S_2 mean the inside and the outside cavity. C represents the cavity boundary.

By integrating the above equation over the region S_j and applying the divergence theorem, we can derive the integral,

$$\psi(\boldsymbol{r'}) = \int_C dl[\psi(l)\partial_\mu G(l,\boldsymbol{r'};k) - G(l,\boldsymbol{r'};k)\partial_\mu \psi(l)]. \tag{2.21}$$

Also, as $\boldsymbol{r'}$ approaching the boundary C, the above equation can be written as,

$$\frac{1}{2}\psi(\boldsymbol{r'}) = \int_C dl[\psi(l)\partial_\mu G(l,\boldsymbol{r'};k) - G(l,\boldsymbol{r'};k)\partial_\mu \psi(l)], \tag{2.22}$$

in the sense of Cauchy's principal value [31].

By applying the above equation to both the inside and the outside of boundary and reformulating the equation, we can derive a linear homogeneous boundary integral equations (BIEs),

$$\int_C dl[B(l,l')\phi(l) + C(l,l')\psi(l)] = 0, \tag{2.23}$$

where $B(l,l') = -2G(l,l';k)$, $C(l,l') = 2\partial_\mu - \delta(l-l')$ and $\phi(l) = \partial_\mu \psi(l)$. Using the boundary conditions eq. (2.6) and eq. (2.7) at the cavity boundary, BIEs can be also expressed in the matrix form as

$$\begin{pmatrix} B_1 & C_1 \\ B_2 & C_2 \end{pmatrix} \begin{pmatrix} \phi \\ \psi \end{pmatrix} = M \begin{pmatrix} \phi \\ \psi \end{pmatrix} = 0,$$

where B_j and C_2 are the function in the region S_j.

To solve the BIEs, we need to discretize the cavity boundary into tiny boundary elements. We assume that the wave function and its normal derivative are considered as constant valued in each boundary element. Then, BIEs in eq. (2.23) can be approximated by the homogeneous linear equations as

$$\sum_{s=1}^{N} (B_{js}\phi_s + C_{js}\psi_{js}) = 0, \tag{2.24}$$

where N is the number of boundary elements, $B_{js} = \int_s dlB(l_j, l)$, $C_{js} = \int_s = \int_s dlC(l_j, l)$, $\phi_s = \phi(l_s)$ and $\psi_s = \psi(l_s)$. These equations are transformed to the homogeneous matrix equation such as the above matrix equation and in this equation matrix M is a $2N \times 2N$ square matrix. Applying the outgoing boundary condition at r_∞, we can calculate matrix elements of M.

The homogeneous equations (eq. (2.24) has nontrivial solutions only if the determinant of the matrix M is 0. So, the complex wave vector k of $detM(k) = 0$ is the eigenstate of a deformed microcavity. This eigenvalue k can be found using root-finding methods such as the Newton-Raphson method.

2.2.3 Husimi function

For understanding the underlying physics of the mode characteristics, we need to relate the mode function to the classical phase space structure. To compare the wave function calculated using numerical methods with the PSOS, we can implement the Husimi projection [32]. In the phase space which is position-momentum space, we cannot obtain full information of position space and momentum space simultaneously because of the uncertainty principle like as in qunatum mechanics. Therefore, we can have the phase space projection of the wave function by overlapping the wave function with the minimum uncertainty wave packet centered at $(\phi, \sin\chi)$ point on the PSOS [33]. Then, the Husimi function $H(\phi, \sin\chi)$ can be defined as

$$H(\phi, \sin\chi) = \int d\Phi r_c \psi(r_c, \Phi)\zeta(\Phi; \phi, \sin\chi), \tag{2.25}$$

with the minimum uncertainty packet

$$\zeta(\Phi;\phi,\sin\chi) = (\sigma\pi)^{-1/4}\sum_{l}\exp -\frac{1}{2\sigma}(\Phi+2\pi l-\phi)^2 - ik_0\sin\chi(\Phi+2\pi l), \tag{2.26}$$

where $\sigma = \sqrt{2}/nka$, the uncertainty in ϕ coordinate. To apply the above equation to the Birkhoff coordinate, we need to transform the angle coordinate ϕ to the normalized arclength s.

For example, Fig. 2.8 shows that the wavefunction and its corresponding husimi function. The Husimi function districution is well matched to the KAM tori on the PSOS.

2.3 Experimental Setup

To experimentally study a deformed microcavity, we use a liquid jet column made of ethanol doped with lasing dye as a gain medium. The cross section of nodes or anti-nodes of a liquid jet can be implemented and its deformation parameter is continuously tunable. Using the cavity modified fluorescence spectroscopy, the resonance frequency, the directionality and the quality factor of the specific mode can be experimentally measured. In this section, we briefly review a liquid jet cavity which has been used for a deformed microcavity experiments in our lab, referring to and quoting the context of [34, 35, 25].

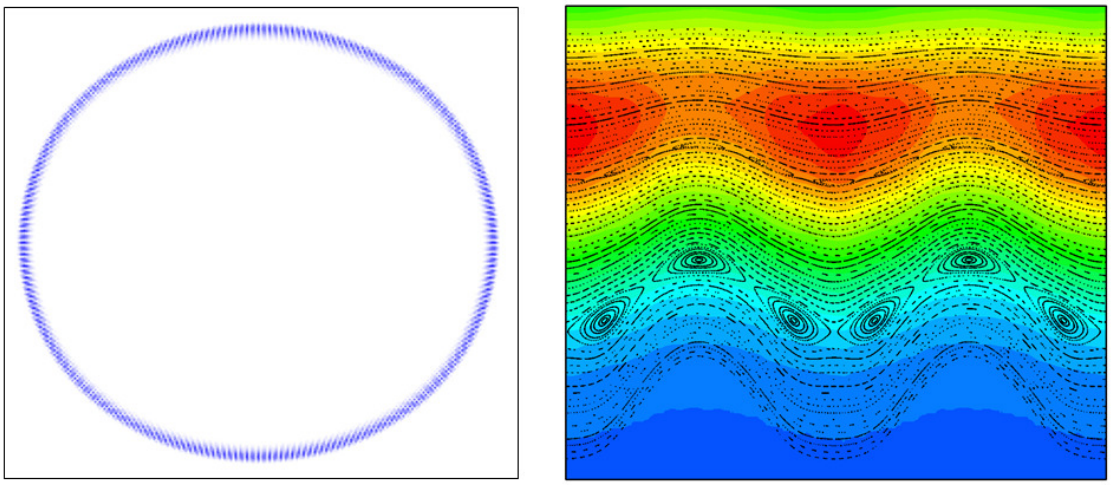

Figure 2.8: The wave function of l=1 mode near $ka \simeq 141.43$ and its corresponding husimi function on the PSOS in the range from $0.8 < \sin\chi < 1$ and $0 < s < 1$.

2.3.1 Liquid jet cavity

The liquid jet column is formed by ejecting ethanol through a deformed orifice. The ejected jet is a stationary tidal column as shown in Fig. 2.9. The surface of the column oscillates due to viscosity and the oscillation is damped along the jet propagating direction. Then, the jet surface shape can be approximated in the cylindrical coordinate as

$$r(\theta, z) = a[1 + \eta_0 \exp(-\frac{z}{v_z \tau}) \sin(\frac{2\pi}{v_z T} z + \zeta) \cos 2\theta], \tag{2.27}$$

where a is the mean radius, η is a seed deformation, τ is the characteristic decay time, T is the oscillation time of the jet column and ζ is the initial phase term of the oscillation at the orifice. The decay time and the oscillation period depend on the liquid property and the orifice size. We assume that the jet velocity v_z is uniform across the jet ignoring the effect of the gravitational force [36]. Also, in this equation, we consider only the quadrupole component described as $\cos 2\theta$ for convenient. The higher order terms are so small that it does not significantly affect to the overall shape. But the octapole component might impact on the chaotic transition so we will consider the octapole component later.

To perform experiments in a 2D deformed mocricavity, we use the cross section of nodes or anti-nodes of the liquid jet column oscillation. The nodes or anti-nodes can be found at $z_n's$ ($n = -1, 0, 1, 2, ...$ in Fig. 2.9) satisfying the condition which the argument of the sine function is $\frac{\pi}{2} + n\pi$ in eq. (2.27).

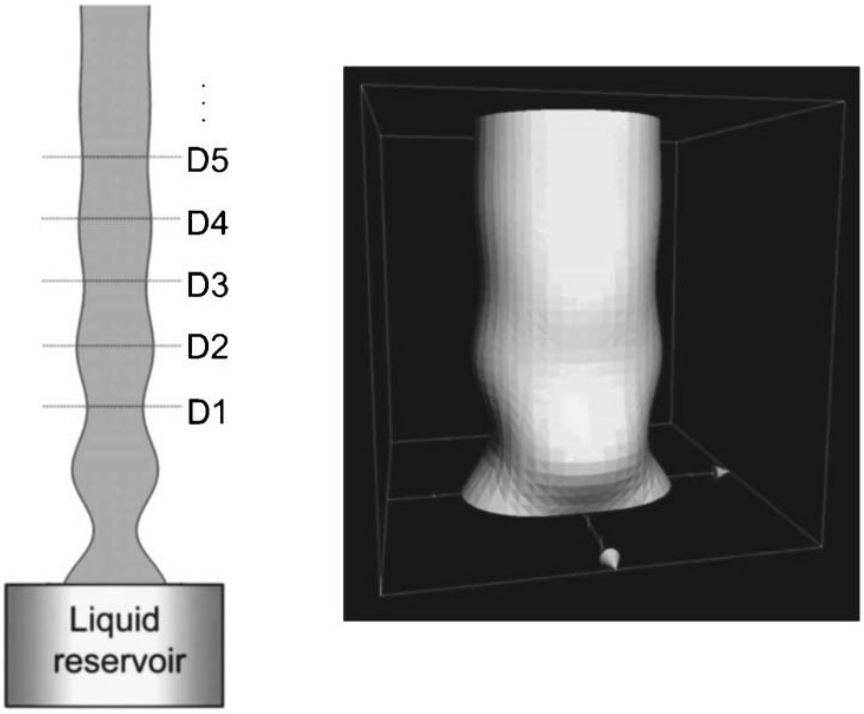

Figure 2.9: Model picture of the liquid jet column ejected from the deformed orifice [34].

Then at the cross section, the cavity boundary shape is approximated by

$$r(\theta, z_n) = a[1 + (-1)^n \eta_n \cos 2\theta], \tag{2.28}$$

where

$$\eta_n = \eta_0 \exp\left(-\frac{z_n}{v_z \tau}\right). \tag{2.29}$$

Also, we defined the cross-section at z_n as D_n. Then, for a given jet velocity, the boundary shape deformation η_n for D_n might exponentially decrease for the upper cross-section along z-axis.

2.3.2 Deformation Tunability

The deformation parameter η_n of $D_n's$ can be controlled by adjusting the ejection pressure. From eq. (2.27), the jet boundary shape at the orifice ($z = 0$) can be approximated as

$$r(\theta, 0) = a(1 + \eta_0 \sin\zeta \cos 2\theta). \tag{2.30}$$

In fact, the boundary shape of orifice can be described in terms of the even-symmetry Fourier series including higer-order term such as $\cos 4\theta$, $\cos 6\theta$ etc. However, the higer-order terms decay more rapidly, at $D_n's$, the jet boundary shape is well approximated by eq. (2.27). Because the shape of the orifice can not be changes, the orifice deformation parameter $\eta_0 \sin\zeta$ is fixed. However, the η_0 and $\sin\zeta$ can be changed respectively by adjusting the ejection pressure.

The initial radial direction velocity of the jet boundary just outside the orifice can be obtain by taking a time derivative of eq. (2.27),

$$v_r(\theta) \simeq \left(\frac{2\pi a}{T}\right)\eta_0 \cos\zeta \cos 2\theta, \tag{2.31}$$

where we ignore the damping effect. Due to the geometry of the inner wall of the nozzle, the radial velocity might be the proportional to the jet ejection velocity. So we can described the radial velocity in terms of v_z,

$$v_r(\theta) = K v_z \cos 2\theta, \tag{2.32}$$

where the K is the proportionality constant depending only on the inner geometry of the nozzle and the liquid properties. Using the above two equations about the radial velocity, we can find the relation

$$\eta_0 \cos\zeta = K v_z T / 2\pi a. \tag{2.33}$$

With this equation and the relation $\eta_i = \eta_0 \sin\zeta$, we can find the relation between the jet ejection pressure and the seed deformation,

$$\eta_0 = \sqrt{\eta_i^2 + (\frac{KT}{2\pi a})^2 v_z^2}. \tag{2.34}$$

Figure 2.10 shows the deformation parameter as the function of the ejection pressure. By adjusting the pressure and changing the cross-section position, we can obtain the desirable deformation parameter.

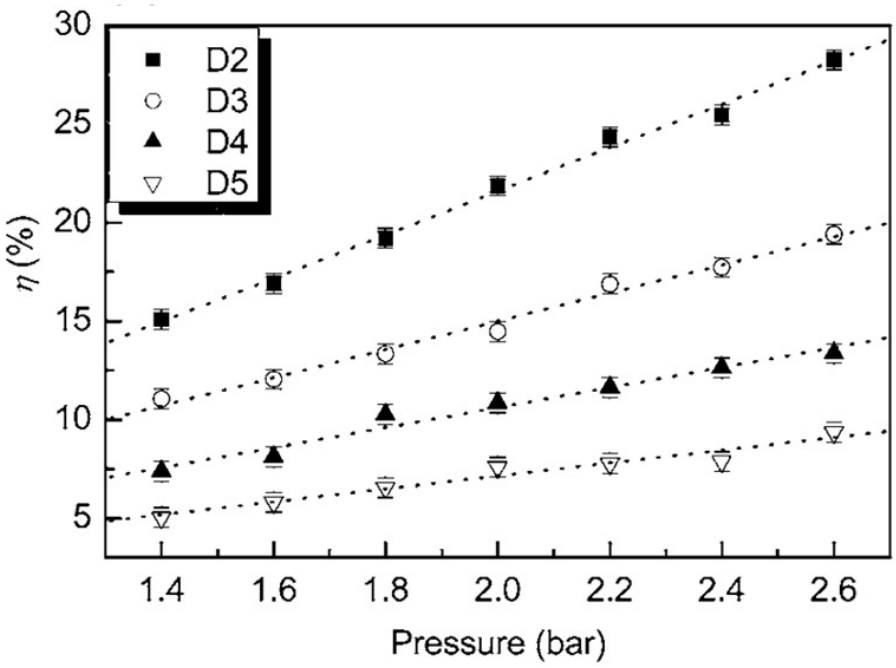

Figure 2.10: Deformation as the function of the ejection pressure for D2, D3, D4 and D5 [34].

Chapter 3

Resonance-assisted tunneling theory

3.1 Canonical perturbation theory

Generally, multidimensional systems are not integrable, so the solution to the Hamilton-Jacobi equation does not exit. However, for the weakly perturbed system, the approximate solutions can be obtained to a desired degree of accuracy by expanding the generating function successively [37]. At first, we find the first order perturbation of a one degree of freedom system.

The weakly perturbed one-dimensional time independent Hamiltonian can be generally written as,

$$H = H_0(I) + \epsilon H_1(I, \theta) + \cdots , \tag{3.1}$$

in terms of action-angle variable (I, θ), where H_0 is an integrable Hamilto-

nian. H_0 has a solution such as

$$\begin{aligned} I &= I_0, \\ \theta &= wt + \beta \\ w &= dH_0/dI, \end{aligned}$$

where I_0, w and β are constants. Then, to find the transformation for which the new Hamiltonian $\bar{H}$ is integrable, we use the 2nd kind generating function $F_2(\bar{I}, \theta)$. Then, the generatong function and the new Hamiltonian can be described as power series in η,

$$F = \bar{I}\theta + \epsilon F_1 + \cdots , \tag{3.2}$$

$$\bar{H} = \bar{H}_0 + \epsilon \bar{H}_1 + \cdots , \tag{3.3}$$

omitting subindex of F_2. From the generating function eq.(3.2), the old action and new angle are derived as,

$$\begin{aligned} I &= \frac{\partial F}{\partial \theta} = \bar{I} + \epsilon \frac{\partial F_1(\bar{I}, \theta)}{\partial \theta} + \cdots , \\ \bar{\theta} &= \frac{\partial F}{\partial \bar{I}} = \theta + \epsilon \frac{\partial F_1(\bar{I}, \theta}{\partial \bar{I}} + \cdots . \end{aligned}$$

Then, old variables can be found in terms of new variables up to first order of ϵ,

$$I = \bar{I} + \epsilon \frac{\partial F_1(\bar{I}, \bar{\theta})}{\partial \bar{\theta}} + \cdots , \tag{3.4}$$

$$\theta = \bar{\theta} - \epsilon \frac{\partial F_1(\bar{I}, \bar{\theta})}{\partial \bar{I}} + \cdots . \tag{3.5}$$

Also, because the generating function does not depend on time, the new Hamiltonian can be written in terms of the new variables,

$$\bar{H}(\bar{I}, \bar{\theta}) = H(I(\bar{I}, \bar{\theta}), \theta(\bar{I}, \bar{\theta}). \tag{3.6}$$

Using the above equations (3.4) and (3.5), the right-hand side of eq.(3.6) can be expanded up to first order of ϵ such as,

$$H_0(I(\bar{I},\bar{\theta})) = H_0(\bar{I}) + \epsilon \frac{\partial H_0}{\partial \bar{I}} \frac{\partial S_1}{\partial \bar{\theta}} + \cdots , \tag{3.7}$$

$$\epsilon H_1(I(\bar{I},\bar{\theta}),\theta(\bar{I},\bar{\theta})) = \epsilon H_1(\bar{I},\bar{\theta}) + \cdots . \tag{3.8}$$

By inserting eq.(3.7) and eq.(3.8) into the eq.(3.6) and comparing eq.(3.6) with eq.(3.3), the new Hamiltonian is derived in terms of the new variables and the generating function, eq.(3.2), such as,

$$\bar{H}_0 = H_0(\bar{I}), \tag{3.9}$$

and

$$\bar{H}_1 = w(\bar{I}) \frac{\partial F_1(\bar{I},\bar{\theta})}{\partial \bar{\theta}}, \tag{3.10}$$

where $w(\bar{I}) = \frac{\partial H_0}{\partial \bar{I}}$.

In the above transforamtion, a new Hamiltonian should be a function of the action variable only. For this purpose, we can introduce the averaging part of H_1,

$$< H_1 >= \frac{1}{2\pi} \int_0^{2\pi} d\bar{\theta} H_1(\bar{I},\bar{\theta}), \tag{3.11}$$

and the oscillating part

$$[H_1] = H_1 - < H_1 > . \tag{3.12}$$

Then, from eq.(3.10), the new Hamiltonian and the generating function are given as,

$$\bar{H}_1 =< H_1 >, \tag{3.13}$$

$$w \frac{\partial F_1}{\partial \bar{\theta}} = -[H_1]. \tag{3.14}$$

Combining (3.9) and (3.13), we find the new transformed Hamiltonian up to first order,

$$\bar{H} = H_0(\bar{I}) + \epsilon < H_1(\bar{I}, \bar{\theta}) > + \cdots \tag{3.15}$$

Also, by describing the $[H_1]$ and F_1 in Fourier series,

$$[H_1] = \sum H_{1n}(\bar{I}) \exp^{in\theta} \tag{3.16}$$

and

$$F_1 = \sum F_{1n}(\bar{I}) \exp^{in\theta}, \tag{3.17}$$

we can derived a Fourier series of F_1 from eq.(3.14)

$$F_{1n} = -\frac{H_{1n}}{inw}, \tag{3.18}$$

when n and w are not zero. The generating function can be derived from the old Hamiltonian.

Similar procedure can be applied to a multidimensional system. We can write a multidimensional Hamiltonian as

$$H(\boldsymbol{I}, \boldsymbol{\theta}) = H_0(\boldsymbol{I}) + \epsilon H_1(\boldsymbol{I}, \boldsymbol{\theta}), \tag{3.19}$$

where $\boldsymbol{I}$ and $\boldsymbol{\theta}$ are the multidimensional actions and angles. Then, we can define the generating function as

$$F = \bar{\boldsymbol{I}} \cdot \boldsymbol{\theta} + \epsilon S_1(\bar{\boldsymbol{I}}, \boldsymbol{\theta}) + \cdots . \tag{3.20}$$

As in one dimension, the new Hamiltonian can be written as, to zero order,

$$\bar{H}_0(\bar{\boldsymbol{I}}) = H_0(\bar{\boldsymbol{I}}) \tag{3.21}$$

and, to first order,

$$\bar{H}_1 = \boldsymbol{w}(\bar{\boldsymbol{I}}) \cdot \frac{\partial F_1(\bar{\boldsymbol{I}}, \bar{\boldsymbol{\theta}})}{\partial \bar{\boldsymbol{\theta}}} + H_1(\bar{\boldsymbol{I}}, \bar{\boldsymbol{\theta}}, \tag{3.22}$$

where

$$\boldsymbol{w}(\bar{\boldsymbol{I}}) = \frac{\partial H_0(\bar{\boldsymbol{I}})}{\partial \bar{\boldsymbol{I}}}. \tag{3.23}$$

Then, by averaging eq.(3.22) over all the angle variables, we find

$$\bar{H} = H_0(\bar{\boldsymbol{I}}) + \epsilon < H_1(\bar{\boldsymbol{I}}, \bar{\boldsymbol{\theta}}) > \tag{3.24}$$

and

$$\boldsymbol{w} \cdot \frac{\partial F_1}{\partial \bar{\boldsymbol{\theta}}} = -[H_1]. \tag{3.25}$$

Also, we can expand H_1 and F_1 in Fourier series such as,

$$H_1 = \sum_{\boldsymbol{m}} H_{1\boldsymbol{m}}(\boldsymbol{I}) \exp^{i\boldsymbol{m}\cdot\boldsymbol{\theta}}, \tag{3.26}$$

and

$$F_1 = \sum_{\boldsymbol{m}} F_{1\boldsymbol{m}}(\boldsymbol{I}) \exp^{i\boldsymbol{m}\cdot\boldsymbol{\theta}}, \tag{3.27}$$

where

$$\boldsymbol{m} \cdot \boldsymbol{\theta} = m_1\theta_1 + \cdots + m_N\theta_N \tag{3.28}$$

with integer m_i and the number of dimension, N.

Inserting above relations to eq.(3.25), we can derived the first order generating function,

$$F_1 = i \sum_{\boldsymbol{m}\neq 0} \frac{H_{1\boldsymbol{m}}(\bar{\boldsymbol{I}})}{\boldsymbol{m} \cdot \boldsymbol{w}(\bar{\boldsymbol{I}})} \exp^{i\boldsymbol{m}\cdot\bar{\boldsymbol{\theta}}} + \cdots . \tag{3.29}$$

3.2 Resonance-assisted Dynamical tunneling in a 2D system

Applying the eq.(3.29), we encounter the divergence problem of the denominator when $\boldsymbol{m} \cdot \boldsymbol{w}$ is close to zero. This is called as "classical non-linear resonance". In the resonance condition, we can not apply the canonical perturbation theory. In this section, we review the perturbation theory near the resonance in a 2D system.

The Hamiltonian dynamics near non-linear resonances can be described by means of the secular perturbation theory. For two-dimensional system, the Hamiltonian with a perturbation can be written as

$$H = H_0(I_1, I_2) + V(I_1, I_2, \theta_1, \theta_2), \tag{3.30}$$

in terms of the action-angle variable where H_0 is an integrable Hamiltonian and V is a perturbation. A resonance condition arises for co-prime positive integer p and q when $p\frac{dH_0}{dI_1} = q\frac{dH_0}{dI_2}$. Then by choosing the generating function as,

$$F_2 = (\theta_1 - \frac{q}{p}\theta_2)\hat{I}_1 + \theta_2\hat{(I)}_2, \tag{3.31}$$

a canonical transformation from $(I_1, I_2, \theta_1, \theta_2)$ to $(\hat{I}_1, \hat{I}_2, \hat{\theta}_1, \hat{\theta}_2)$ is given as

$$\begin{aligned} I_1 &= \hat{I}_1, \\ I_2 &= \hat{I}_2 - \frac{q}{p}\hat{I}_2, \\ \hat{\theta_1} &= \theta_1 - \frac{q}{p}\theta_2, \\ \hat{\theta_2} &= \theta_2. \end{aligned} \tag{3.32}$$

In this transformation, $\hat{\theta}_1$ remains constant as the $p:q$ resonance and varies slowly near the resonance. Then, it is possible to "average" the Hamiltonian over $\hat{\theta_2}$ near the resonance, to obtain the transformed Hamiltonian to first-order,

$$H_{p:q} = H_0 + \bar{V}(\hat{I}_1, \hat{I}_2, \hat{\theta}_1), \tag{3.33}$$

where $\bar{V} = \frac{1}{2\pi p}\int_0^{2\pi p} d\theta_2 V(I_1, I_2, \theta_1, \theta_2)$. Then, $\bar{V}$ can be written as $\frac{2\pi}{p}$ periodic function,

$$\bar{V} = \sum_{j=0} V^j_{p:q} \cos(jp\hat{\theta}_1 + \xi_j). \tag{3.34}$$

Since $V^j_{p:q}$ generally fall off rapidly as j increases, we take $j = 0, 1$ terms. Also, without loss of generality we can take $\xi_1 = 0$ just by trivial constant change of $\hat{\theta_1}$.

Then, by expanding H_0 about $I_{p:q}$, ignoring the constant terms and taking lowest order term in a perturbation and $(I - I_{p:q})$, we can derive a pendulum-like effective Hamiltonian near the $p:q$ resonance,

$$H_{p:q} = \frac{(I - I_{p:q})^2}{2M_{p:q}} + V_{p:q}\cos p\theta, \tag{3.35}$$

where $I = \hat{I}_1$, $I_{p:q}$ is the action I at the resonance, $\theta = \hat{\theta}_1$, $V_{p:q} = V^1_{p:q}$ and $M^{-1}_{p:q} = d^2H_0/dI^2(I_{p:q})$. For a example, the phase space structure of the effective Hamiltonian, eq.(3.35), is described in Fig. 3.1

3.3 Predictions of RADT

In the effective Hamiltonian, eq.(3.35), the eigenstate of the integrable part of the Hamiltonian is given as $|m> \ \exp^{im\theta}$, where m is the mode number.

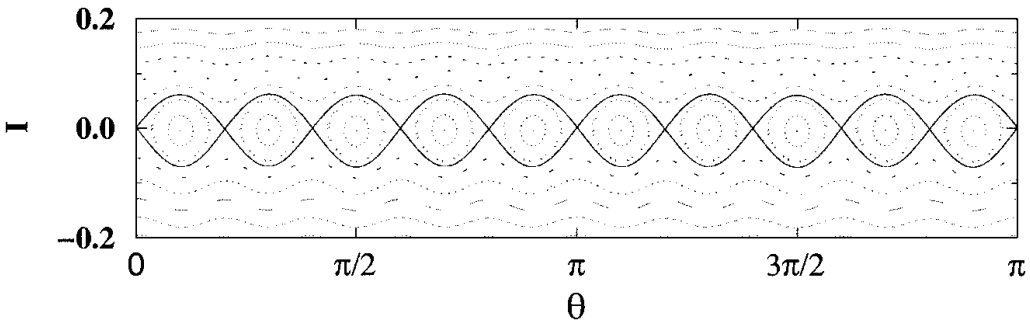

Figure 3.1: Phase space structure of the pendulum-like effective Hamiltonian near the 10:1 resonance [39].

By the perturbation term, $V_{p:q}\cos p\theta$, the eigenstate $|m>$ can be strongly coupled to the eigenstate $|m+p>$. Then, $V_{p:q}$ characterizes the coupling strength, It will be shown below. Also, if we do not ignore the $V^j_{p:q}$ terms in eq.(3.34), $|m>$ can be coupled to the eigenstate $|m+jp>$ with $V^j_{p:q}$ characterizing the coupling strength. Considering second and higher order corrections, the eigenstate $|m>$ interacts with the eigenstate $|m+jp+j'p>$, then the coupling strength might be related to the $V^j_{p:q}V^{j'}_{p:q}$. In any cases, when the eigenmode of the integrable Hamiltonian is coupled to the other mode by the $p:q$ non-linear resonance, their mode index number should differ by integer multiple of p. It gives a *selection rule* for strong interactions.

Also, $V_{p:q}$ can be infered from the phase space structure. When $H = V$, the motion is along the separatrix on the phase space. In this condition, the angular momentum can be written in terms of the θ as $(I - I_{p:q}) = \pm\sqrt{2MV}\sqrt{1-\cos\theta}$. Then, the island area ($S_{p:q}$) enclosed by separatrix

can be calculated,

$$\begin{aligned} S_{p:q} &= 2\int_0^{2\pi}(I - I_{p:q})d\theta \\ &= 2p\sqrt{2M_{p:q}V_{p:q}}\int_0^{2\pi/p}\sqrt{1-\cos p\theta}d\theta \\ &= 2\sqrt{2M_{p:q}V_{p:q}}\int_0^{2\pi}\sqrt{1-\cos x}dx \\ &= 16\sqrt{MV}. \end{aligned}$$

It gives

$$V_{p:q} = \frac{S_{p:q}^2}{256M_{p:q}}. \tag{3.36}$$

The mth and $m+p$th eigenstates of the integrable part in eq.(3.35), the coupling strength between two states can be derived as,

$$\begin{aligned} & < m|Vp:q\cos p\theta|m+p > \\ = & \frac{1}{2\pi}\int_0^{2\pi}\exp^{-im\theta}V_{p:q}\cos p\theta\exp^{i(m+p)\theta}d\theta \\ = & V_{p:q}\frac{1}{4\pi}\int_0^{2\pi}\exp^{-im\theta}(\exp^{ip\theta}+\exp^{-ip\theta})\exp^{i(m+p)\theta}d\theta \\ = & V_{p:q}\frac{1}{4\pi}\int_0^{2\pi}d\theta = \frac{V_{p:q}}{2}, \end{aligned}$$

so $\frac{V_{p:q}}{2}$ is the coupling strength. Then, avoided crossing (AC) gap (δV), twice of the coupling strength, is determined as,

$$\delta V = V_{p:q} = \frac{S_{p:q}^2}{256M_{p:q}}. \tag{3.37}$$

$M_{p:q}$ is defined by the dynamics of the integrable Hamiltonian. Therefore, we can infer the variation of the perturbation (or AC gap) by measuring the change of the phase space area, $S_{p:q}$.

Chapter 4

Observation of the resonance-assisted dynamical tunneling

4.1 Introduction

Although we reviewed the RADT theory for a 2-dimensional system, the theory can be applied to multii-dimensional systems following the similar derivation. Also, the RADT theory is derived for a general Hamiltonian. So, we can apply the RADT theory to any perturbed systems of near integrable of mixed phase space. Actually, the RADT has been studied in various systems such as periodic-driven pendula [41], Rydberg atoms under periodic perturbation [42], quantum accelerator modes [43] and multidimensional molecules [44, 45]. RADT has also been extensively studied in

one-dimensional time periodic qunatum maps such as the kicked Harper model and the kick rotor [38, 39, 46, 49, 50]. However, up to our knowledge, the RADT has been studied theoretically until now and there exists no experimental confirming the prediction of the RADT theory in real system.

On the other hand, for studies of a 2-dimensional billiard system such an optical microcavity, a microwave billiard etc., the internal mode coupling has attracted a lot of interests. The internal mode coupling due to the chaos assisted tunneling and the exceptional point was experimentally confirmed in microwave billiards. Also, for an optical microcavity, the mode pattern change and corresponding mode characteristics variations are theoretically studied [51, 52] and the coupling strength change was experimentally measured as deformation varies [53, 54]. However, the studies of the internal mode interaction mainly focus on the result of the interactions. It is still an open question to elucidate the underlying for the interactions in a deformed cavity.

We try to apply the RADT theory to an optical microcavity system. In this system, the deformation can be continuously controlled by adjusting the ejection pressure of the dye doped ethanol jet cavity. Also, the AC gaps due to the RADT can be observed by the spectrum measurement. We expect that an optical microcavity might be prominent tool for experimental confirmation of RADT and this work might shed lights on finding the semiclassical back ground describing the interaction in a microcavity.

4.2 Husimi function localization along the resonant tori

At first, to study the inter-mode interactions in a deformed microcavity, we find the eigenvalues in the given range with varying the deformation. Fig. 4.1(a) shows the mode-dynamics diagram calculated using BEM for $\eta = 0.16$. For this, we first numerically find high-Q mode spectrum in the range from $ka \sim 100$ to $ka \sim 180$ and label the *uncoupled* mode groups as *mode order* l (=1,2,3,4) by the order of the free spectral range in the *uncoupled* region. Then, we define the sequence of reference frequencies of regular spacing and measure the relative frequencies of the each mode group with respect to the reference frequency. Detailed information of the *uncoupled* mode labeling and the relative frequency measuring is described elsewhere [53].

The relative frequencies of 4 mode groups are plotted in mode-dynamics diagram for η=0.16 in Fig. 4.1. Each mode group more or less follows *diabatic* line but they show AC while encountering other mode groups. By inspecting the AC gaps, approximately proportional to the coupling strength between uncoupled modes, we can *qualitatively* distinguish two kinds of interactions, *strong* (red circle) and *weak* (blue circle) interactions.

To further investigate the distinction between two kinds of interaction, we consider the Husimi distribution of quasi-eigenmodes near the interaction region and compare it to the Poincaré surface of section (PSOS) of

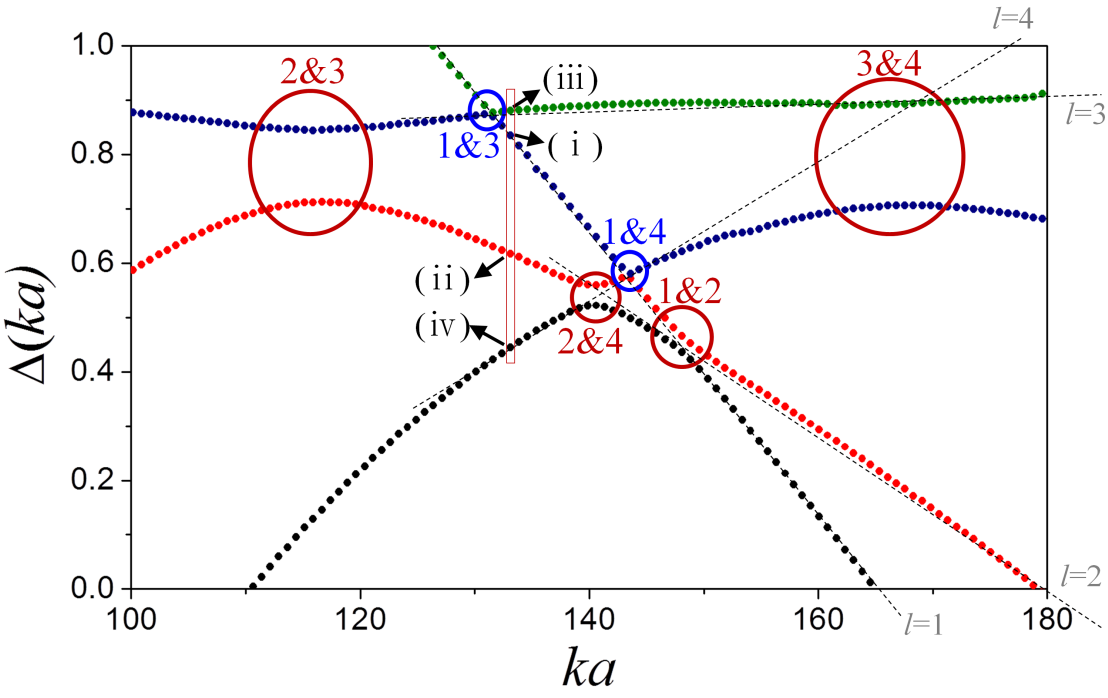

Figure 4.1: Mode dynamics diagram showing relative frequencies $\Delta(ka)$ of l=1, 2, 3 and 4 modes calculated with respect to a reference frequency in the range from $ka \simeq 100$ to $ka \simeq 180$ when $\eta = 0.16$.

the augmented ray dynamics [55]. Fig. 4.2 and Fig. 4.3 shows the Husimi plots of the modes near the interaction region of *weak* and *strong* interactions, respectively. In Fig. 4.2, the Husimi functions of the two nearest quasi-eigenmodes experiencing the *weak* interaction show mixing of the Husimi functions of the two quasi-eigenmodes far off avoided-crossing region in which the eigenvalues follow nearly diabatic lines. Although, the eigenvalues change following the *adiabatic* line, the lateral distributions and the $\sin\chi$ values of the Husimi function change following the *diabatic* line. This feature is generally expected in AC's of quasi-eigenmodes.

On the other hand, when two modes undergo a strong inter-mode interaction as shown in Fig. 4.3, their Husimi functions are well localized along the stable or unstable periodic orbits associated with a classical nonlinear resonance structure in the phase space. Also, it seems that the lateral husimi distributions does not follow the *diabatic* line but change following the *adiabatic* line near the AC region. Only the $\sin\chi$ values vary following the *diabatic* line, which is related to the decay rate of the quasi-eigenvalue and shows the mode group order l. In addition, the localized distributions of the Husimi functions remain over a large ka range around the closest encounter.

All of the strong and weak interactions in Fig. 4.1 show the above tendencies of the Husimi functions, respectively, upon AC's (For the Husimi functions of other interactions, refer to the appendix. A). In particular, the

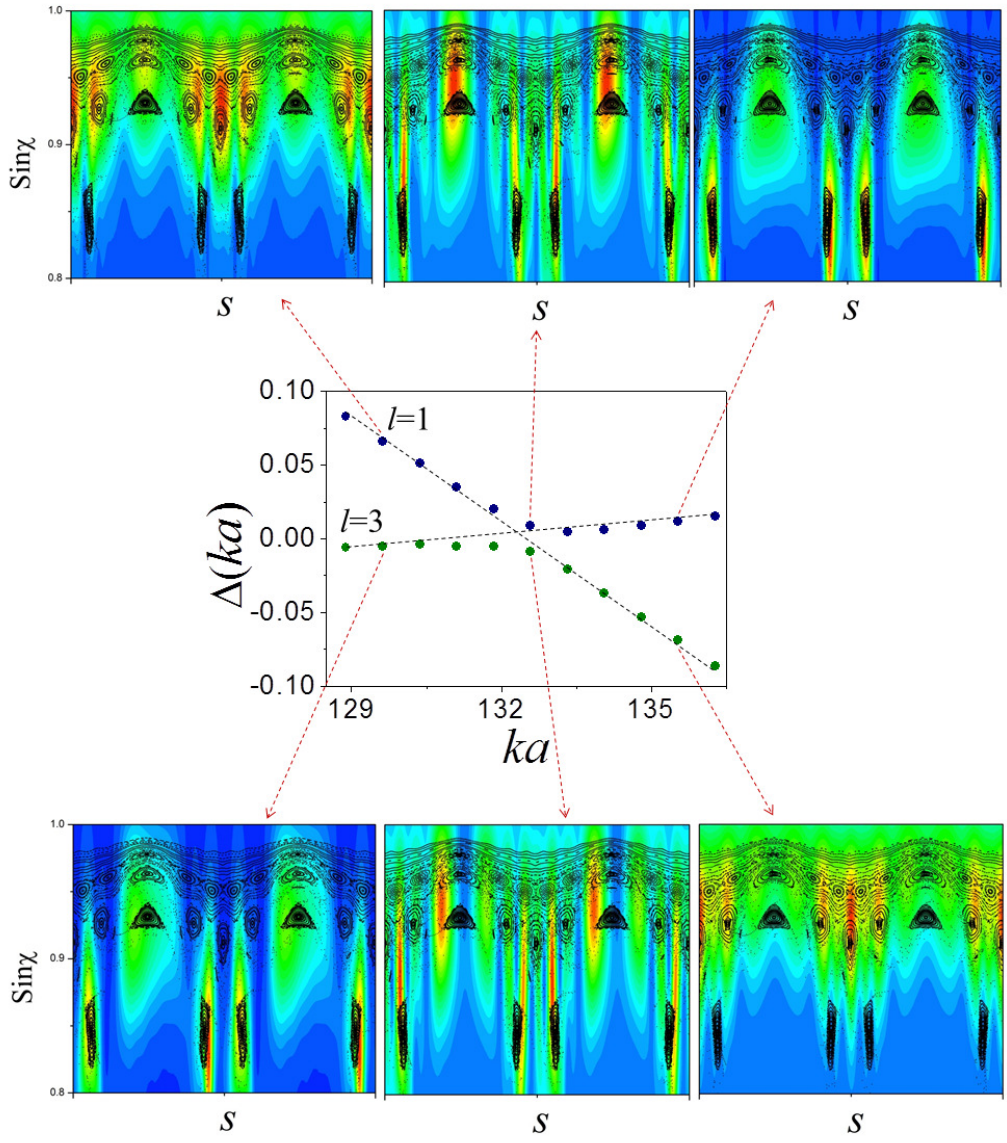

Figure 4.2: Relative frequencies of l=1 and 3 modes near the AC region and the Husimi plots of the two modes at the closest encounter, marked by dashed arrows, when $\eta = 0.19$.

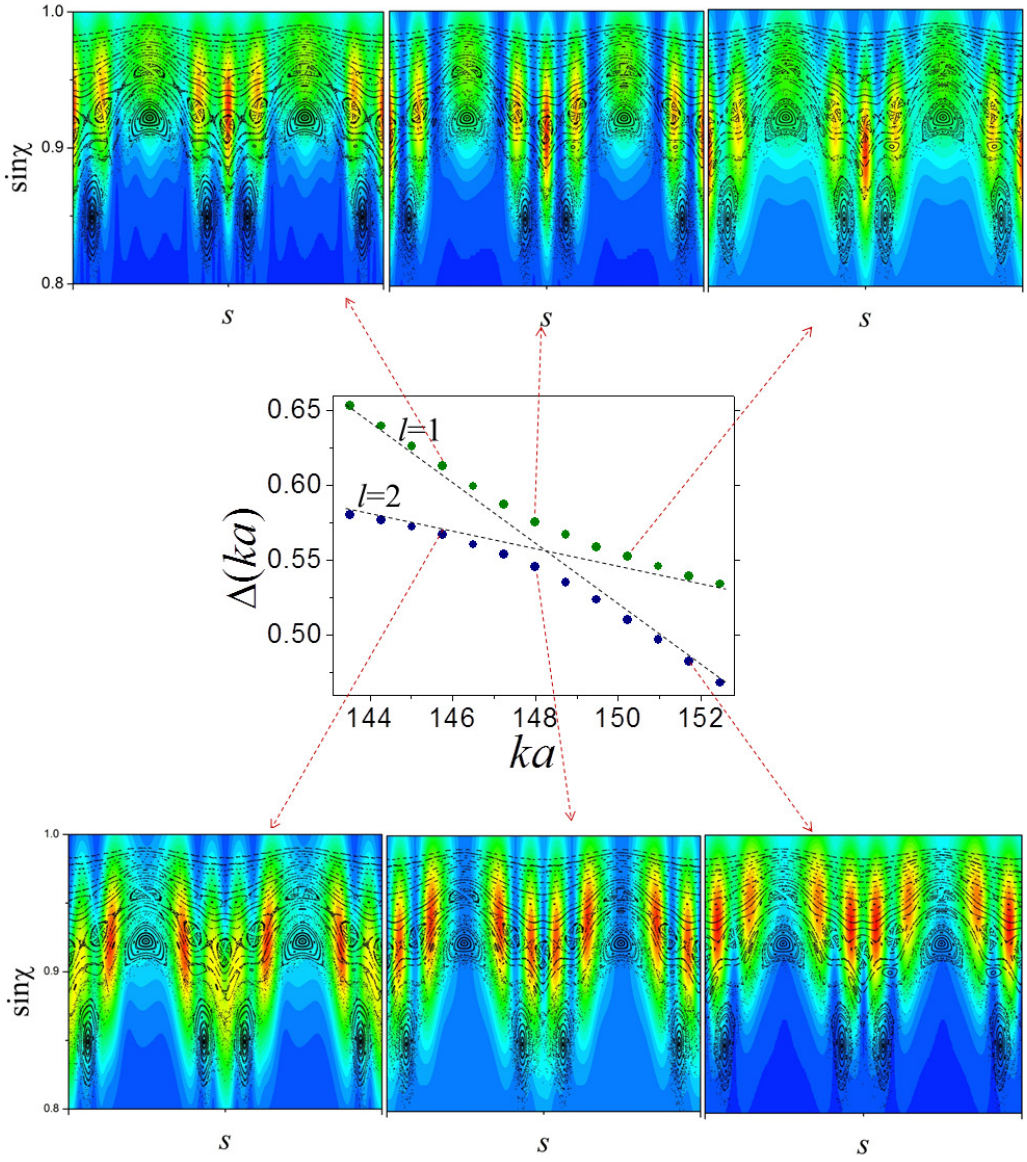

Figure 4.3: Relative frequencies of l=1 and 2 modes near the AC region and the Husimi plots of the two modes at the closest encounter, marked by dashed arrows, when $\eta = 0.16$.

Husimi function localization phenomena suggests that the strong interaction is related to the nonlinear resonance structure [50]. We are thus motivated to apply the RADT theory to the strong inter-mode interactions in our system.

Note that, far from the closest encounter, the Husimi functions of the each mode group undergoing the resonance-assisted interaction reside 'higher' or 'lower' than the resonance chain in the PSOS. While undergoing the interaction, the Husimi functions are localized along the resonant tori between their original position. In a perspective of the wave optics, it is trivial, because the modes undergoing the interaction are described as the superposition of the unperturbed modes. However, it is not directly implied in the RADT theory.

Also, it seems that the Husimi function localization along the resonance tori is related to the spatial mode distribution. The trajectory connecting the boundary points where the intensity modulation of the spatial mode pattern undergoing the resonance-assisted interaction corresponds to the related resonant torus 4.4. We can interpret this result as the existence of the closed classical trajectory corresponding to the spatial mode distribution of the interacting mode decides the localization of the Husimi function and it enhance the coupling between the unperturbed modes.

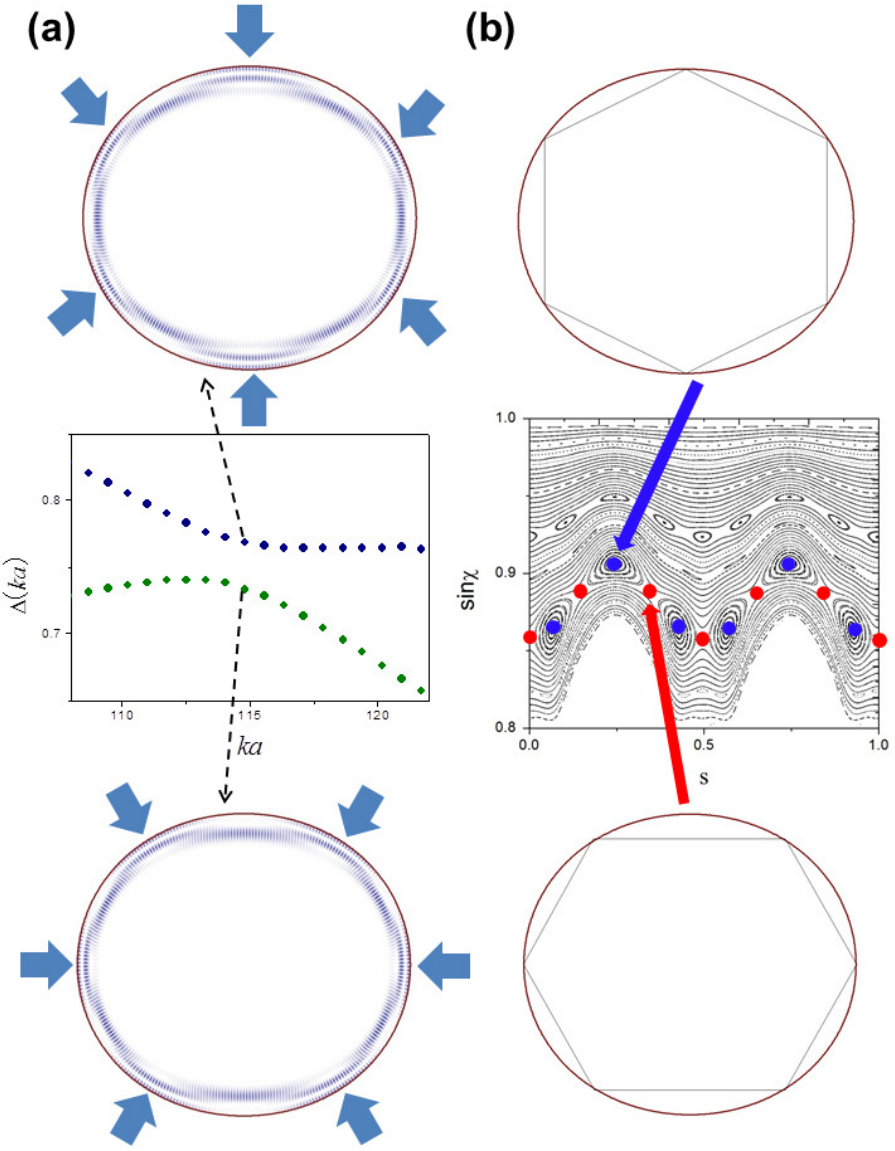

Figure 4.4: (a) The spatial mode distribution of $l = 2$ and $l = 3$ showing the $p = 6$ resonance-assisted interaction at the closest encountering region near $ka \simeq 114$ at $\eta = 0.10$. (b) Corresponding classical trajectory and the phase space position

4.3 Selection Rule

To verify the selection rule predicted by the RADT theory for strong interactions, we should identify the angular mode number of each mode group. The angular mode index is defined for a circular cavity where the angular momentum of the moving particle is conserved and represented as the angular mode index. As mentioned before, the quasi-eigenstates of a circular cavity inside the boundary for TM modes are described by,

$$\Psi(r, \theta) = J_m(k_i r) \cos m\theta,$$

where k_i is the i-th wavevector satisfying the boundary condition, and then i means radial mode order. Spatial mode distributions for 4 mode groups was given in Fig. 4.5.

Although, for deformed microcavities, the angular mode index is not defined in principle, far from the interaction region, a quasi-eigenmode can be described as the slightly varied corresponding unperturbed quasi-eigenmode, so we can infer the mode number by inspecting the spatial mode distribution of the quasi-eigenmode. In Fig. 4.6, the intensity plots of spatial mode distributions are shown for each mode group. (Compare the Fig.4.5 with Fig. 4.6.) In each plot, we count the number of anti-nodes of which a half gives the angular mode index m. In each mode group, the angular mode index m increases by 1 when ka increases by one free spectral

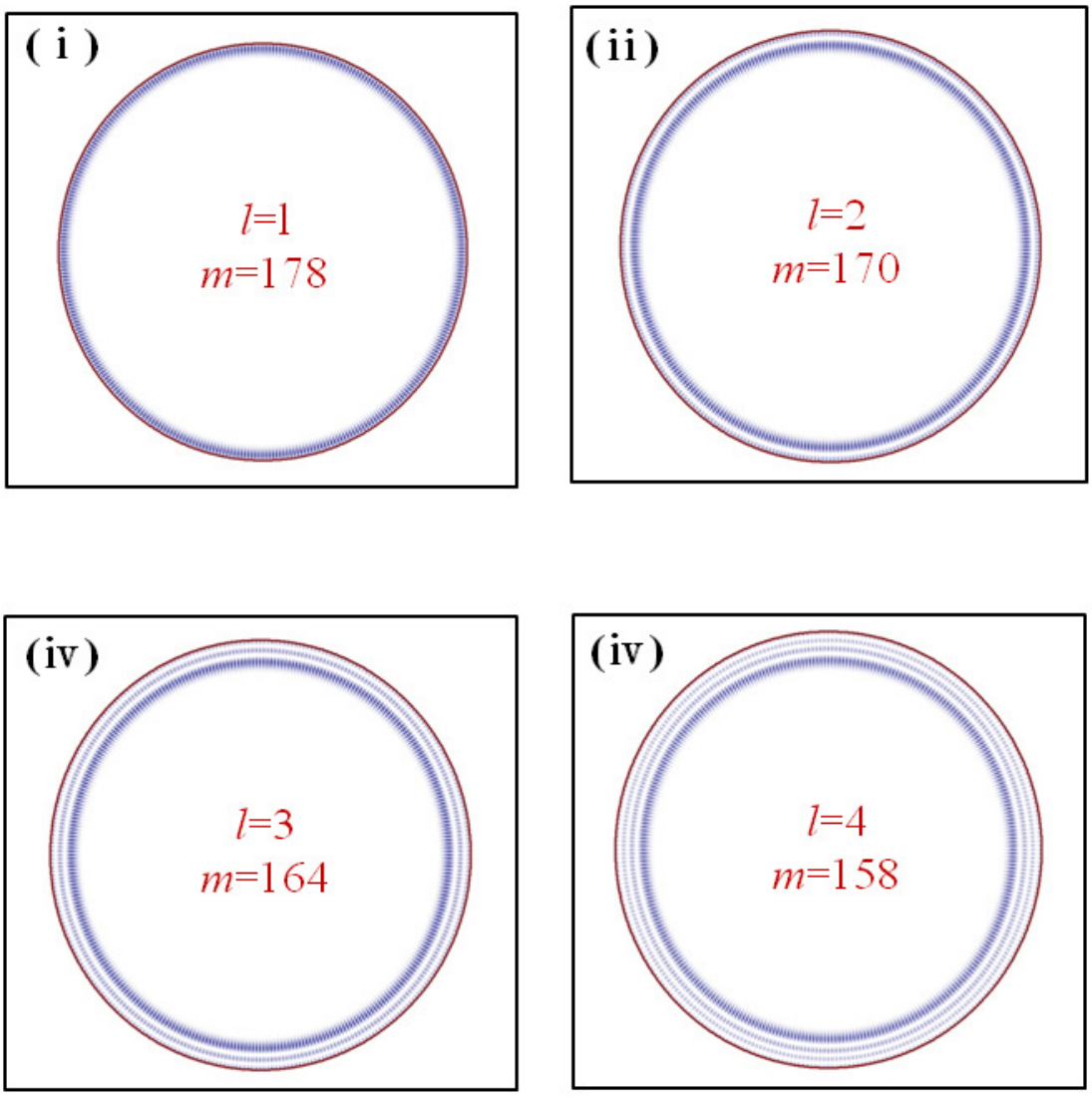

Figure 4.5: Spatial mode-distribution intensity plot for l=1,2,3 and 4 modes for a circular cavity corresponding to the mode distributions of Figure 4.6.

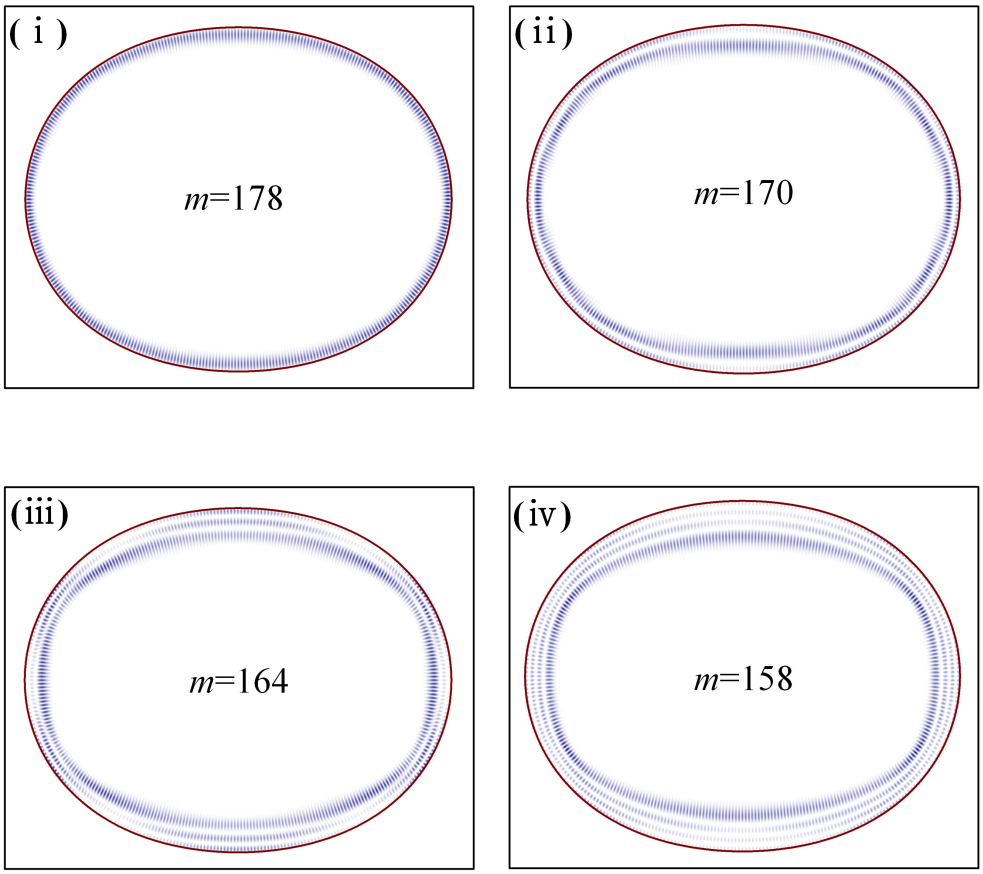

Figure 4.6: Spatial mode-distribution intensity plot for l=1,2,3 and 4 modes marked by arrow in Figure (4.1) , when $\eta = 0.16$. The angular mode index m is indicated for each plot.

l	Δm	p	type
1vs2	8	8	Strong
2vs3	6	6	Strong
3vs4	6	6	Strong
2vs4	12	6	Strong
1vs3	14	NA	Weak
1vs4	20	NA	Weak

Table 4.1: Comparison between the angular mode number difference (Δm) and the number of island (p) of the related chain structure for each unperturbed basis mode interaction.

range along the adiabatic line. So, the angular mode index differences (Δm) between four mode groups with respect to the same reference ka are not changed. Also, the radial mode number can be identified by counting the number of anti-nodes along the radial direction, and we find that the mode group number means the radial mode number of each mode group.

The result of our examination on the relation between Δm and p for all strong and weak interactions in Fig. (4.1) is summarized in Table 4.1. For all the strong interaction in Fig. 4.1, the angular mode number difference is equal to or two times of the number of the island in the related resonance chain structure as expected by the selection rule in the RADT theory. For the interactions of l=1 with l=3 and l=1 with l=4, the 6-island chain and the 8-island chain reside between tori along which the Husimi distributions of quasi-eigen modes spread far from the interaction region. So we can see that the weak interactions do not satisfy the selection rule, because the

number 6 and 8 are not divisors of the number 14 or 20.

To confirm the enhancement of the coupling strength induced by the RADT, the coupling strength of resonance-assisted interaction of two specific mode groups should be compared to the coupling strength of non-RADT-induced interaction of the identical pair of mode groups. For this, we calculate the mode-evolution in the extended range, up to $ka \simeq 300$ (Figure 4.7). Because the quality factor of each mode group also increases as ka increases, the number of the high-Q modes increases in the mode dynamics plot. The free spectral range of each mode group increases as the radial mode index increases. Two mode groups showing interactions at specific ka meet again each other at increased ka. Our cavity boundary has symmetry about the x-axis and y-axis in cartesian coordinate, so modes do not interact with any modes of different parity about two axes. It means that the mode index difference of two interacting modes is even number. Therefore, two mode groups meet again, their angular mode number difference increases by 2.

The interaction between $l = 2$ and $l = 4$ is assisted by the non-linear resonance structure near $ka \simeq 141$ because $\Delta m = 12$ and the $p = 6$. However, when two mode groups meet again near $ka \simeq 210$ (red circle in Fig. 4.7), $\Delta m = 14$ and the interaction can not be assisted by the resonance structure due to the reason mentioned above. The AC gaps, proportional

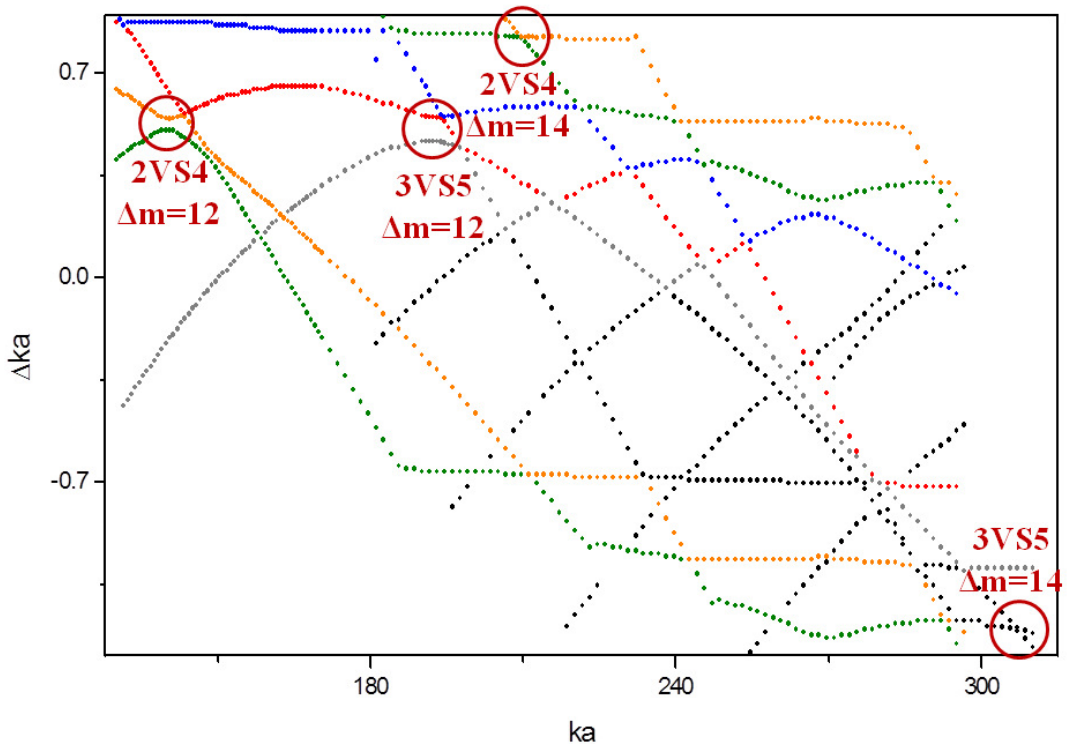

Figure 4.7: Extend high-Q mode evolution plot in the range from $ka \simeq 100$ to $ka \simeq 300$ when $\eta = 0.16$.

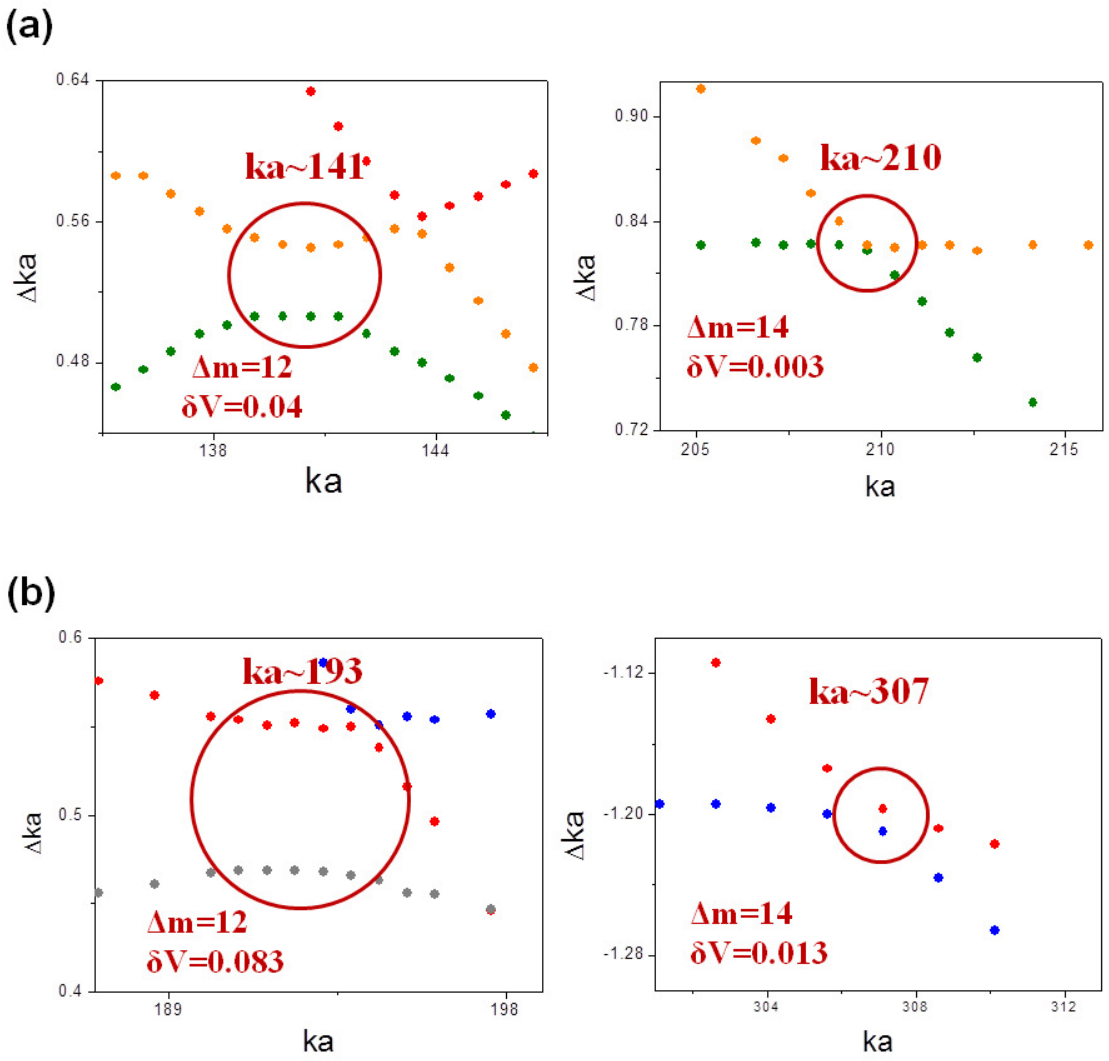

Figure 4.8: (a) Relative frequency of $l = 2$ and $l = 4$ near AC region, $ka \simeq 141$ and $ka \simeq 210$ when $\eta = 0.16$. (b) Same plot of $l = 3$ and $l = 5$ near $ka \simeq 193$ and $ka \simeq 307$.

to the coupling strength, for theses interactions are plotted in Fig. 4.8(a). The AC gap of RADT induced interaction, $ka \simeq 141$, is $\delta V simeq 0.04$. This gap size is ten times lager than the gap size of the interaction while the RADT is not related, $\delta V \simeq 0.003$. Also, in the extended examination, we find that $l = 3$ and $l = 5$ encounter each other near $ka \simeq 193$ ($\Delta m = 12$, related to the RADT)and $ka \simeq 307$ ($\Delta m = 14$, not related to the RADT). (Figure 4.8(b)) For these interactions, the coupling strength of the RADT related interaction ($\delta V \simeq 0.083$) is much stronger than the other interaction ($\delta V \simeq 0.013$).

Interestingly, the number of islands in the non-linear resonance structure is always even because of the cavity symmetry. So, the non-linear resonance structure also mediated mode interactions between modes of even Δm, similar to general interactions.

4.4 S^2 dependence of the coupling strength

4.4.1 RADT theory in the Birkhoff's coordinate

In the previous section, we confirmed the selection rule, one of the predictions of the RADT theory for strong interactions. The RADT theory also predicts that the AC gap size of interactions related to the non-linear resonance is proportional to the squared area of the corresponding non-linear resonance structure (S) given as eq.(3.36). The AC gap is experimentally measurable quantity in our liquid-jet system. So we try to experimentally confirmed the S^2 dependence of the coupling strength.

To study an optical microcavity, the motion in the billiard has been generally presented in terms of the Birkhoff's coordinate (s, $\sin\chi$) and the PSOS is presented in the dimensionless phase space space. However, eq. (3.36) is described in terms of the action-angle variable, (I, θ) and then, the phase space area has the dimension of angular momentum. So, to apply the RADT theory for studying a microcavity, we should describe eq. (3.36) in terms of the Birkhoff's coordinate and transform $S_{p:q}$ and $M_{p:q}$ into dimensionless quantities. Also, δV in eq. (3.36) is order of energy, so it is convenient to described the AC gap in terms of the size parameter, ka.

For a circular cavity which is an integrable system, the action variable can be written as $I = \hbar ka \sin\chi = \hbar ka\tilde{I}$, where $\tilde{I} = \sin\chi$, the momentum component of the Birkhoff coordinate. Also, for the arclength coordinate s, $s = \theta/2\pi$. Then the effective Hamiltonian is rewritten as,

$$H_{p:q} = (\hbar ka)^2 \frac{(\tilde{I} - \tilde{I}_{p:q})^2}{2M_{p:q}} + V_{p:q}\cos p2\pi s. \tag{4.1}$$

To calculate the δV, we should know $M_{p:q}$ but it needs the information of the integrable Hamiltonian, H_0. Unfortunately, the H_0 form is not known until now. We can just guess $M_{p:q}$ from the proportionality constant of linear fitting of $S^2_{p:q}$-δV data. However, we can guess the relation between δV and $S^2_{p:q}$ by applying the crude assumption. For a given k, we try to write the integrable Hamiltonian as $H_0 \simeq h\nu\tilde{H}_0 = \hbar ck\tilde{H}_0$. Then, $M^{-1}_{p:q} = d^2H_0/dI^2 \simeq \frac{\hbar ck}{(\hbar ka)^2}\frac{d\tilde{H}_0}{d\tilde{I}^2} = \frac{\hbar ck}{(\hbar ka)^2}\tilde{M}^{-1}_{p:q}$ where $\tilde{I}$ is the momentum component of Birkhoff coordinate as mentioned before. Here, we assume that the energy change by the variation of the action is given as the change of $\tilde{H}_0$ and k remains constant. Then, $\tilde{M}_{p:q}$ might be related to the frequency change

with action $\tilde{I}$ at the resonance. Applying these relations to the eq.(4.1), we get

$$\delta V = (2\pi)^2 ka \frac{\tilde{S}_{p:q}^2}{256\tilde{M}_{p:q}}. \tag{4.2}$$

Using the above equation, the AC gap can be derived from the resonance chain structure on the PSOS. From now, without notification, $S_{p:q}$ means the phase space area on the PSOS.

4.4.2 Phase space area measurement

As discussed in the previous subsection, it is needed to know the integrable Hamiltonian for deriving the prefactor $M_{p:q}$. But, because $M_{p:q}$ is defined for the integrable system, it remains constant for a given interactions as the deformation is varying. Also, the size paramter ka in eq.(4.2) is defined as the degenerated energy of the interacting mode groups, and it remains constant, too. So, while the perturbation strength changes, a variable is only $\tilde{S}_{p:q}$, the phase space area on the PSOS, in R.H.S. of eq.(4.2). Therefore, to confirmed the RADT, we will measure the AC gap proportional to the square of the related resonance chain structure area on the PSOS.

In a deformed microcavity, the perturbation strength increases as the cavity boundary becomes more deformed. The broadening of the phase space area of the 6 : 1 resonance structure is described in Fig. 4.9 as the deformation increases. Also, as we expect in the pendulum-like effective Hamiltonian, the area of the each island regions is nearly same with each

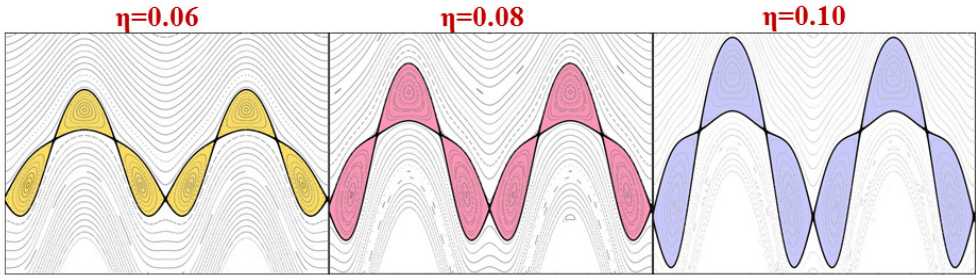

Figure 4.9: The magnified PSOS structure near the $p = 6$ resonance chain structure near $ka \sim 114$ when $\eta = 0.06$, $\eta = 0.08$ and $\eta = 0.10$. $S_{6:1}$ is the area of the shaded region.

other. To compare the resonance chain area with the AC gaps, we measure the $S_{6:1}$ per each $\Delta\eta = 0.25$ or $\Delta\eta = 0.125$. The resonance chain area is measured by fitting the associated seperatrix structure as in Fig. 4.10. The upper and lower part of separatrix enclosing one of 6 islands are fitted as 6th-order polynomial. For example, in Fig. 4.10, the upper-left island (shade region) is selected and the fitting equations are $\sin\chi = 1.01079 - 5.61136 * s + 73.03031 * s^2 - 433.48776 * s^3 + 1369.52815 * s^4 - 2263.80762 * s^5 + 1531.5523 * s^6$ and $\sin\chi = 0.74511 + 3.98317 * s - 47.03553 * s^2 + 290.26484 * s^3 - 965.44671 * s^4 + 1634.8788 * s^5 - 1107.14535 * s^6$ for the upper and the lower part of the separatrix. Then, the $S_{6:1}$ is measured by integrating the difference of these equations between unstable close orbits. The red solid line in Fig. (4.13) is the $S^2_{6:1}$ in the range from $\eta = 0.06$ to $\eta = 0.12$.

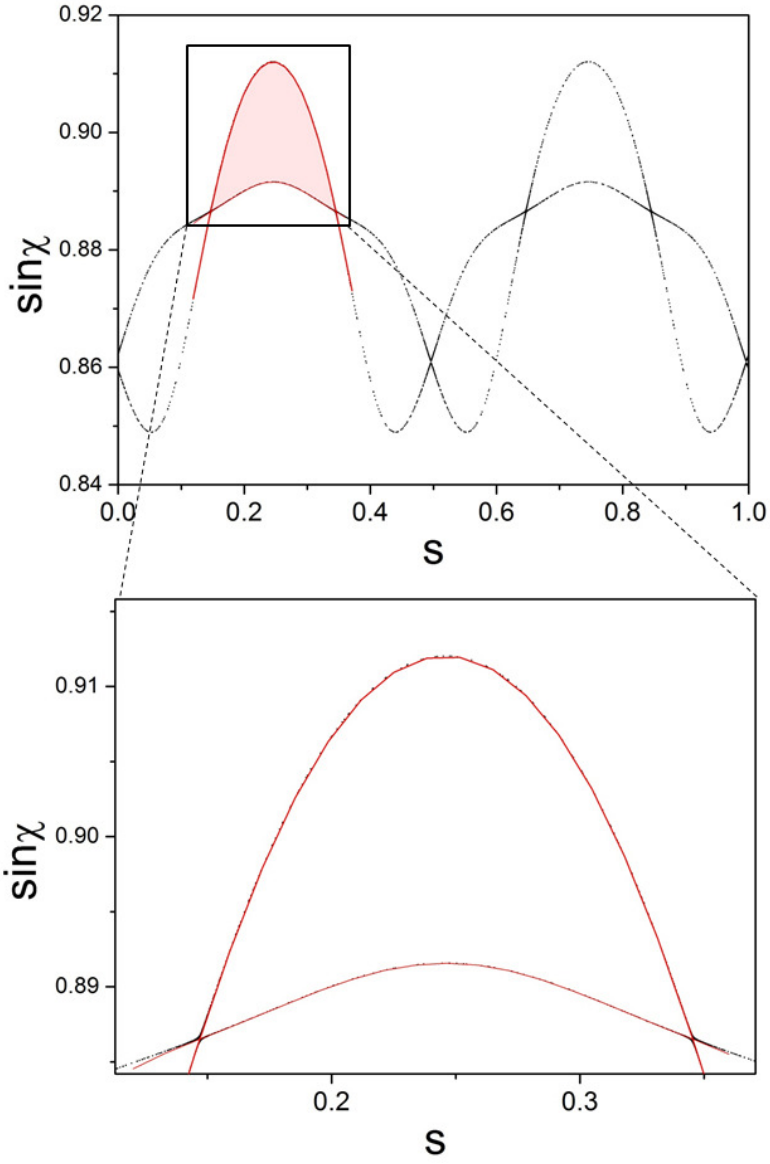

Figure 4.10: (upper) The separatrix structure near the 6 : 1 resonance. near $ka \sim 114$ when $\eta = 0.085$ (lower) The magnified view of the rectangle region in the upper figure. The red-solid line is the 6th order polynomial fitting of the separatrix of the shaded region.

4.4.3 AC gap measurement

The AC gap of the interaction between $l = 2$ and $l = 3$ mode groups is experimentally measured. The interactions is related to the $6 : 1$ resonance tori near $ka \simeq 114$. In our liquid jet microcavity system, the interaction is measured near $\lambda \simeq 832nm$. To cover this spectral range, the cavity medium is doped with laser dye styryl (LDS) 821 molecules at a concentration of 0.03 mM/L. The maximum absorption wavelength of LDS 821 is 574nm and the maximum fluorescence wavelength is 750nm [56]. In this molecular concentration, the fluorescence spectrum of cavity modes can be effectively measured and the medium absorption rate is so low that the high-Q mode can be radiated out from the microcavity. (The output coupling efficiency is given as $\frac{\gamma_{mode}}{\gamma_{mode}+\gamma_{abs}}$ with the cavity mode decay rate γ_{mode} and the absorption rate of the cavity medium γ_{abs}. [54]) Also, the refractive index $n \sim 1.357$ in this range.

Our cavity is pumped by the VERDI-V5 laser at $\lambda = 532nm$. The cavity modified fluorescence spectrum is measured by MS257 (Oriel instrument). The spectrometer resolution is approximately $\Delta\lambda \simeq 0.044nm$ near the center of the CCD for the 1800 groove grating. In terms of the size paramter, it gives experimental error about 0.0029. The part of the cavity-modified fluorescence spectrum is in Fig. 4.11(a). The four high-Q mode groups are identified in the spectrum. In this range, the parity of $l = 2$ and $l = 3$ marked by arrow in Fig. 4.11(a) is opposite to the parity of $l = 1$ and $l = 4$ marked by arrow. So, $l = 2$ and $l = 3$ modes does not interact with $l = 1$ and $l = 4$ modes in this range.

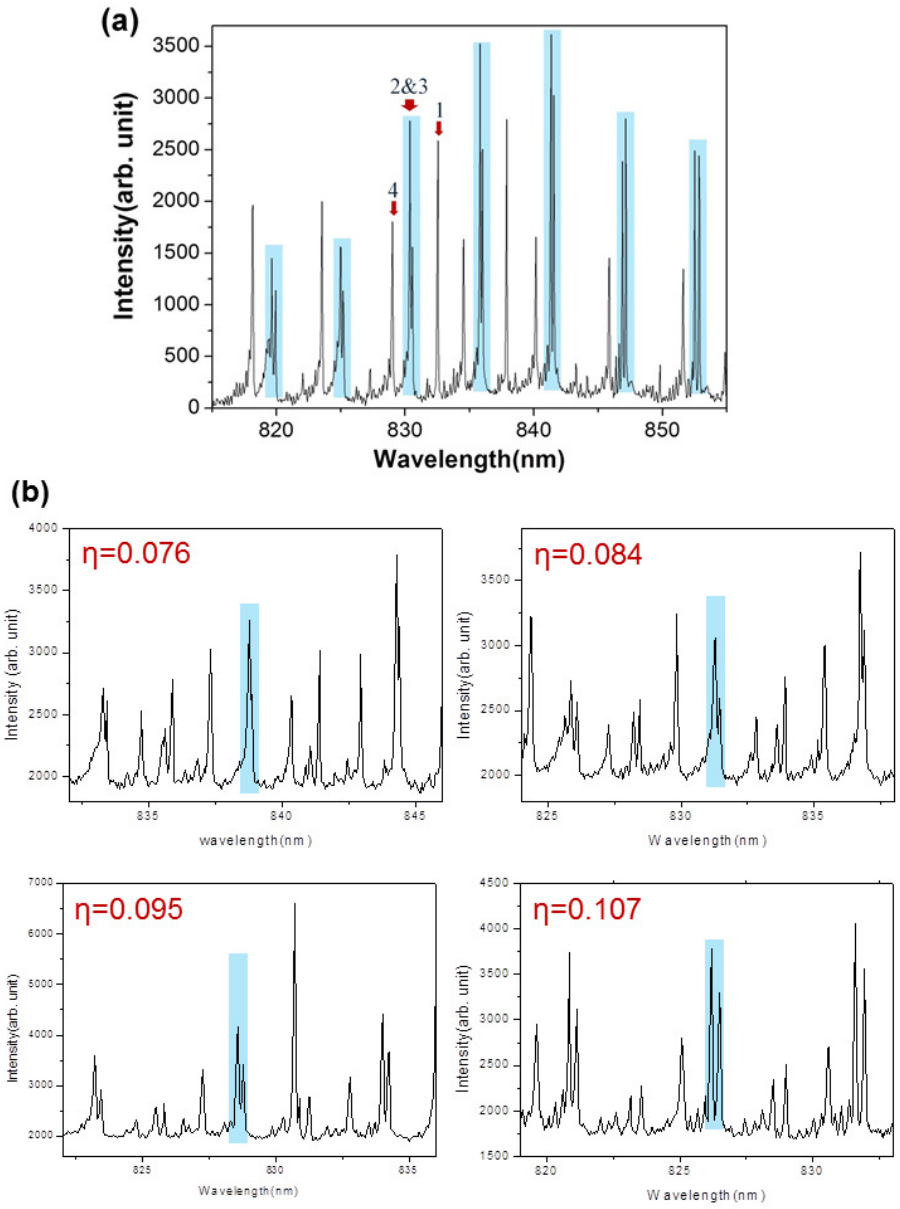

Figure 4.11: (a) Cavity-modified fluorescence spectrum near $\lambda \simeq 835nm$ at $\eta = 0.089$. Peaks of 4 mode groups are marked by arrow. (b) Spectra for various deformation. The pearks corresponding the closest encounters of the interactions between $l = 2$ and $l = 3$ are marked as shaded rectangle.

The cavity deformation can be controlled by adjusting jet ejection pressure. The spectra near the AC region of $l = 2$ and $l = 3$ modes are measured while the cavity deformation parameter varies. In Fig. 4.11(b), the spectra for various deformation are presented. The closest encounter of $l = 2$ and $l = 3$ is marked by shaded rectangles. We can confirm that the AC gap ($\Delta\lambda$) in spectrum increases while the cavity boundary shape becomes more deformed. The δV, the AC gap in terms of the size parameter, can be measured from the spectra at each deformation,

$$\delta V = |\Delta(\frac{2\pi a}{\lambda})| = \frac{2\pi a}{\lambda} \cdot \frac{\Delta\lambda}{\lambda} = ka\frac{\Delta\lambda}{\lambda}. \tag{4.3}$$

4.4.4 Result

To compare $S^2_{6:1}$ with the AC gap, the proportionality constant $\frac{\pi^2}{64}\frac{ka}{\tilde{M}_{6:1}}$ should be determined. The slop of the linear fitting of the δV-$S^2_{6:1}$ plot is the proportionality constant. For this purpose, we also measure the AC gap using the result from the wave calculation. The results are shown in Fig. 4.12. For the interaction of $l = 2$ and $l = 3$, the proportionality constant is given as 69.6466. From this, we can also determine the $M_{6:1}$. More discussion about the proportionality constant or the prefactor $M_{6:1}$ will be later.

Figure 4.13 shows the comparison between $S^2_{6:1}$ and δV. For comparison, the AC gaps from the wave calculation are also presented. We find that the

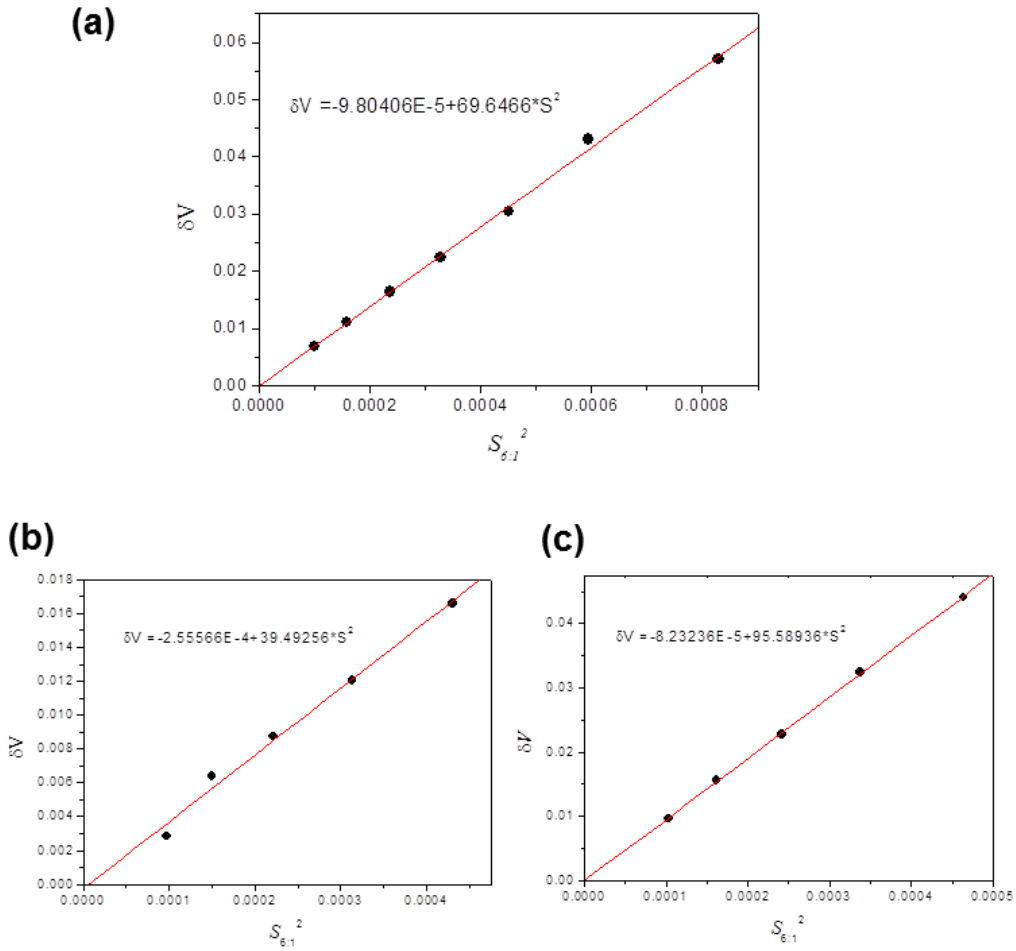

Figure 4.12: (a)δV plot for $S^2_{6:1}$ of the interaction between $l = 2$ and $l = 3$ near $ka \simeq 114$. (b) Same plot of $l = 1$ and $l = 2$. (c) Same plot of $l = 3$ and $l = 4$.

experimental and the numerical results well confirm the $S^2_{6:1}$ dependence of the coupling strength.

For further investigations, we have also performed the wave calculation to measuring the AC gaps for $l = 1$ and $l = 2$ modes near $ka \sim 65$ and $l = 3$ and $l = 4$ modes near $ka \sim 165$. Both interactions are also the resonance-assisted interaction associated to the 6-island chain structure. The proportionality constants for these interactions are determined in the same manner with the interaction of $l = 2$ and $l = 3$ modes, by linearly fitting δV-$S^2_{6:1}$ as in Fig. 4.12(b) and (c). The relation between the size parameter where the AC happens and the proportionality constant will be also discussed later. In Fig. 4.14, we can confirm that both interactions also satisfy the relation $\delta V \sim S^2_{6:1}$ over range from $\eta = 0.06$ to $\eta = 0.10$.

Another way to confirm the relation $\delta V \sim S^2_{6:1}$ is to plot $\log(\delta V)$-$\log(S_{6:1})$. By taking the logarithm both side of eq. (4.1), the relation is given as

$$\log(\delta V) = \log(\frac{\pi^2}{64} \cdot \frac{\tilde{S}^2_{6:1}}{\tilde{M}_{6:1}}) = \log(\frac{\pi^2}{64} \cdot \frac{1}{\tilde{M}_{6:1}}) + 2\log(\tilde{S}_{6:1}). \qquad (4.4)$$

Therefore, the slope of the linear fitting of the $\log(\delta V)$-$\log(S_{6:1})$ graph gives the multiplier of $S_{6:1}$. Figure 4.15 shows the $\log(\delta V)$-$\log(S_{6:1})$ graph of $l = 2$ and $l = 3$ modes. The δV from the wave calculation and $S_{6:1}$ are measure per $\eta = 0.0025$ in the range from the $\eta = 0.06$ to $\eta = 0.08$. In fact, the

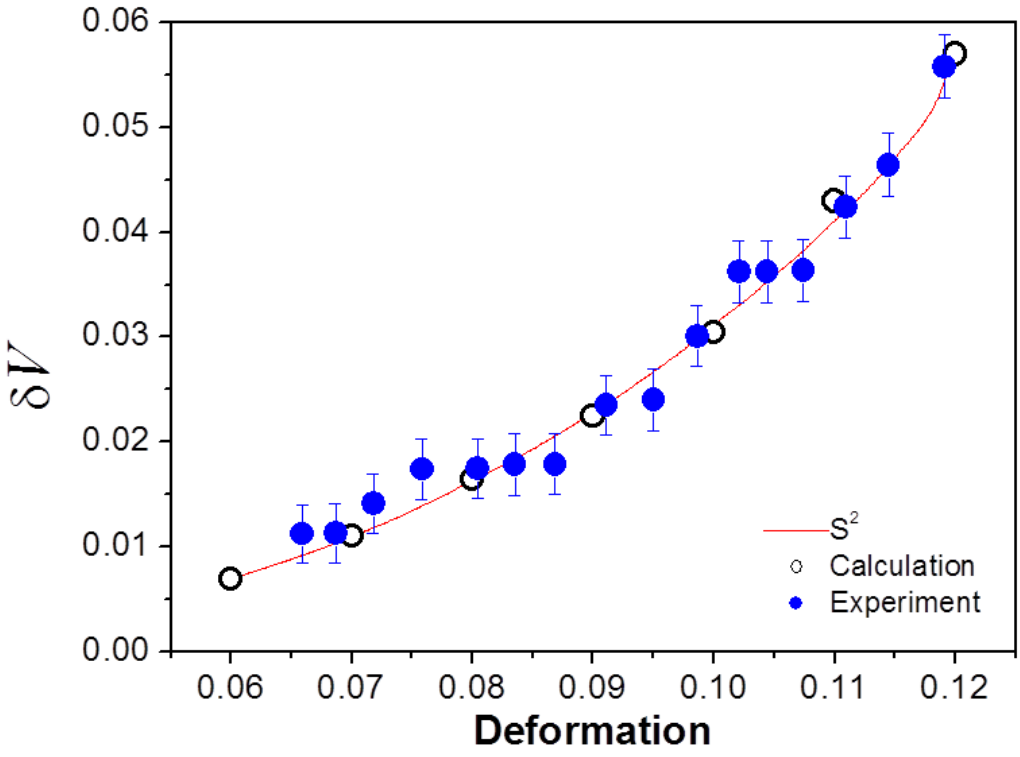

Figure 4.13: Scaled $S^2 2$ (red solid curve) of 6-island resonance structure is compared to the experimentally AC gaps (blue-filled circles) between $l = 2$ and $l = 3$ modes near $ka \simeq 114$. For comparison, the AC gaps from the wave calculation are plotted as black empty circles.

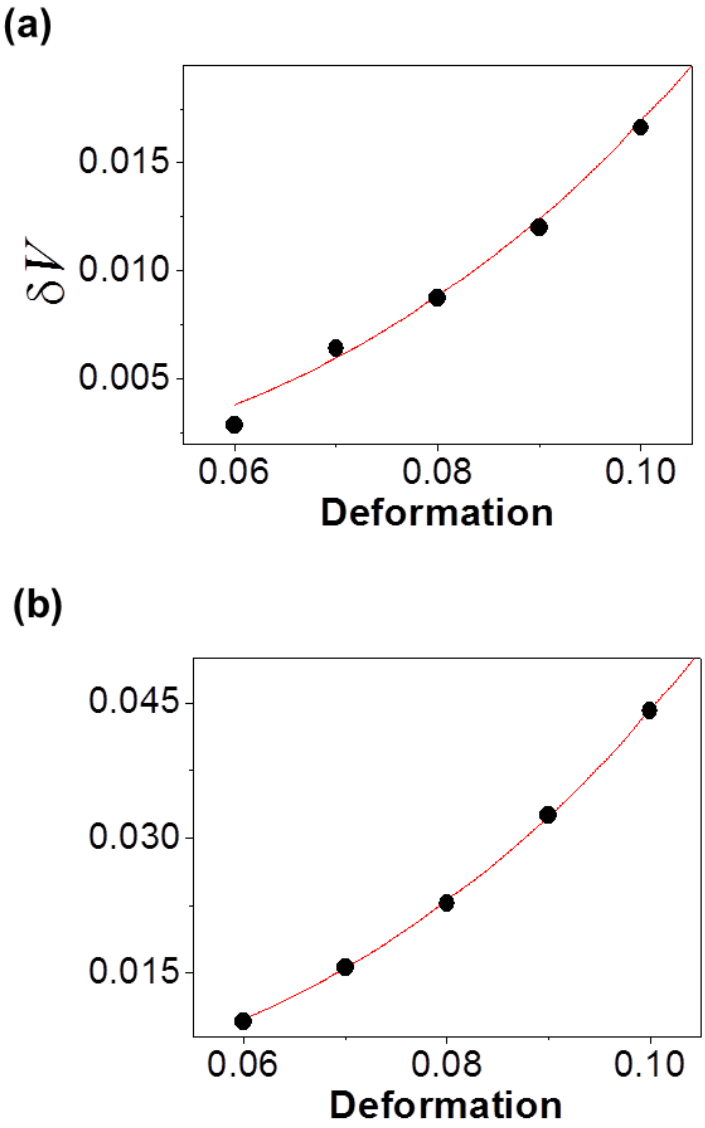

Figure 4.14: (a) Scaled $S^2 2$ of 6-island resonance structure (red curve lined) is compared to the numerically calculated AC gaps between $l = 1$ and $l = 2$ modes near $ka \simeq 65$ (black-filled circles. (b) Same plot for $l = 3$ and $l = 4$ modes near the $ka \simeq 165$.

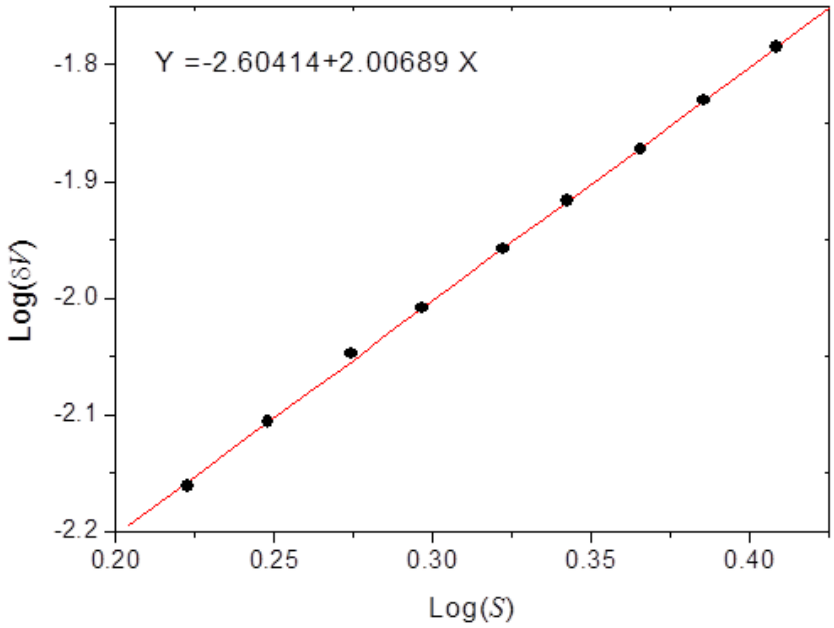

Figure 4.15: $\log(\delta V)$-$\log(S_{6:1})$ plot for the interaction of $l = 2$ and $l = 3$ modes in the range from $\eta = 0.06$ to $\eta = 0.08$.

pendulum-like effective Hamiltonian is derived for weak perturbation, so we take measurements for small deformation as possible as. The $\delta V \sim S_{6:1}^2$ relation is confirmed from the slope of the linear fitting, 2.00689.

Interestingly, the δV-$S_{6:1}$ relation is well confirmed up to relatively larger deformation, $\eta > 0.10$. In principle, the RADT theory is developed for weak perturbation system which can be described by the first order perturbation.

Near $\eta \simeq 0.10$, the separatrix begins to be broken and shows mild stochasticity. The stochasticity is well shown near the unstable periodic orbit as in Fig. 4.16(b). The breaking of the separatrix structure means that the deformed microcavity system is not weakly perturbed system near 6-island resonance structure. (In the upper region on the PSOS, that is more large $\sin\chi$ region, the separatrix near the non-linear resonance remains unbroken.) It is considered as the wave mechanical characteristics of the system. As we can see in Fig. 4.16(a), the size of the Husimi function (related to the minimun uncertainty of the system, $\frac{1}{nka} \sim 5 * 10^{-3}$) is much larger than the size of the stochastic region ($\sim 10^{-4}$). So, the delicate structure can not be distinguished. In the classical regime (very large nka), the minimum uncertainty goes to zero, so all the detail structure of the PSOS can be distinguished. As the deformation increases, the stochastic region becomes broader and evolves into chaotic sea.

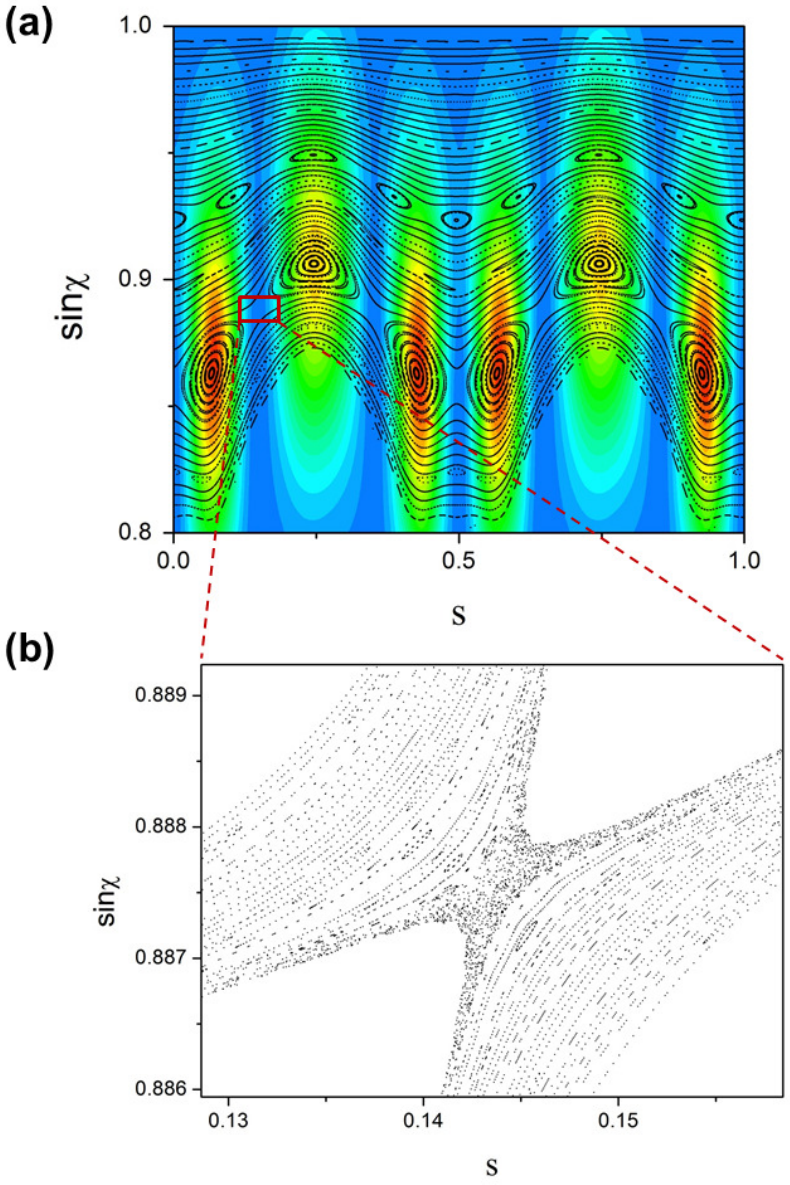

Figure 4.16: (a) The Husimi function and the PSOS near $ka \simeq 114$ when $\eta = 0.10$. (b) The magnified view of the grey rectangle of (a)

Chapter 5

Discussion

5.1 Prefactor, $M_{p:q}$

In the previous chapter, we inferred the coupling strength of the RADT related interactions from the phase space area. Then, the proportionality constant and the prefactor $M_{6:1}$ are considered as constants while the deformation changes. The meaning of the $M_{p:q}$ is the inverse change rate of frequency at the action of resonance, because the prefactor is defined as,

$$M_{p:q} = (\frac{d^2 H_0}{dI^2})^{-1}_{I_{p:q}} = (\frac{d\dot{\theta}}{dI})^{-1}_{I_{p:q}}, \tag{5.1}$$

where we use $\dot{\theta} = dH_0/dI$, so $\dot{\theta}$ is the angular velocity of the motion in the integrable system. Although the prefactor is determined from the details of the integrable Hamiltonian, we can also infer the prefactor by the fitting. The fitting result from the fitting in Fig. 4.12(a) is given as $M_{6:1} = 0.261 \pm 0.00271$.

While deriving the eq. (4.2), it was assumed that $M^{-1}_{p:q} = \frac{\hbar ck}{(\hbar ka)^2} \frac{d^2 \tilde{H}_0}{d\tilde{I}^2} =$

$\frac{c}{\hbar k a^2}\tilde{M}_{p:q}^{-1}$. The dimensionless $\tilde{M}_{6:1}$ can be considered as depending only on the non-linear resonance chain structure on the PSOS because $\tilde{I} = \sin\chi$, the momentum component of the Birkhoff's coordinate. It can be confirmed by comparing the δV with the size parameter where the AC's related to the same resonance structure happen. Ignoring the Goos-Hanchen shift, the PSOS is not changed as the size parameter increases, so $\tilde{M}_{p:q}$ and $\tilde{S}_{p:q}$ are invariant.

The 3 interactions between $l = 1$ and $l = 2$ near $ka \simeq 65$, between $l = 2$ and $l = 3$ near $ka \simeq 115$ and between $l = 3$ and $l = 4$ near $ka \simeq 165$ are related to the 6-island resonance. The δV of each AC is measured at $\eta = 0.08$ and compared to the size parameter where the closest encounter is. The result is shown in Fig. 5.1. The δV for the interactions are well fitted linearly, meaning that the $\tilde{M}_{6:1}$ is nearly invariant. The fitting result gives $\tilde{M}_{6:1} \simeq 0.26 \pm 0.01$.

In the previous discussion, we ignored the effect of the Goos-Hanchen shift. The Goos-Hanchen shift slightly modifies the PSOS structure and as a result, the phase space area $\tilde{S}_{p:1}$ and the prefactor $\tilde{M}_{p:q}$ change slightly. As the size parameter decreases and the effect of the Goos-Hanchen shift increases, the PSOS structure is compressed along the $\sin\chi$ axis. Therefore, as the size parameter increases, the phase space area $\tilde{S}_{p:q}$ increases, and the $1/\tilde{M}_{p:q}$ decreases because $d\dot{\theta}/d\tilde{I}$ decreases. Actually, we can confirm these effect for the above interactions by measuring the phases space area for different size parameters, $S_{6:1} \simeq 0.01488$ near $ka \simeq 65$, $S_{6:1} \simeq 0.01536$ near

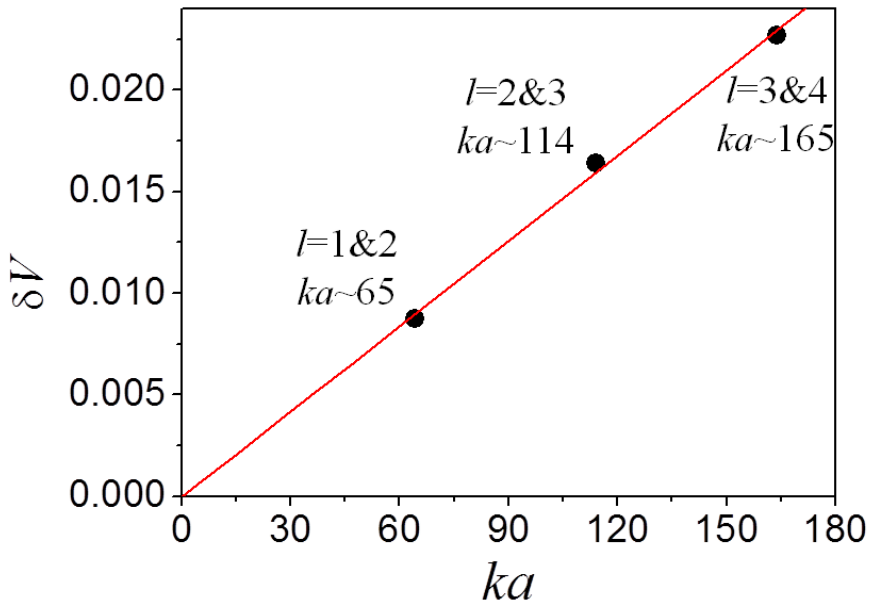

Figure 5.1: (a)ka-δV for 3 interactions related to the 6-island resonance structure at $\eta = 0.08$.

$ka \simeq 114$ and $S_{6:1} \simeq 0.01554$ near $ka \simeq 165$. Also, from Fig. 4.12(b) and (c), we can determine the prefactor for interactions, $M_{6:1} \simeq 0.2512 \pm 0.0147$ and $M_{6:1} \simeq 0.2661 \pm 0.010304$. The prefactors result from 3 interactions are in the error range from the fitting result, from Fig. 5.1, $\tilde{M}_{6:1} \simeq 0.26 \pm 0.01$. $\tilde{S}_{6:1}$ varies in the range of 3%, and $\tilde{M}_{6:1}$ varies in the range of 5%.

5.2 Reconstructing the interaction Hamiltonian

In the previous study, we only consider the first order interaction of the resonance-assisted coupling. However, the RADT can be extended to predict the AC gaps induced by the higher order interaction. In this section, we discuss the second order interaction. The discussion can be applied to higher order cases.

When two mode groups are coupled to the mediator mode group by the resonance-assisted tunneling described by eq. (3.35), the two mode groups can indirectly coupled to each other. At the closest encounter of two indirectly coupled mode groups, the Hamiltonian matrix can be written as

$$H_{2nd} = \begin{pmatrix} E & V & 0 \\ V & E_{med} & V \\ 0 & V & E \end{pmatrix},$$

where E is the unperturbed eigenvalue of the mode group we consider, E_{med} is the unperturbed eigenvalue of the mediator mode groups and V is the coupling strength between each mode group and the mediator mode groups

by the RADT. Then, the eigenvalues of the above Hamiltonian are given as

$$\lambda = E \tag{5.2}$$

or

$$\lambda = \frac{(E + E_{med}) \pm |E - E_{med}|\sqrt{1 + 8V^2/(E - E_{med})^2}}{2}. \tag{5.3}$$

If $V << |E - E_{med}|$, the latter 2 eigenvalues can be approximated as

$$\lambda \simeq E + \frac{2V^2}{(E - E_{med})} \tag{5.4}$$

and

$$\lambda \simeq E_{med} - \frac{2V^2}{(E - E_{med})}. \tag{5.5}$$

Then, the AC gap is determined as

$$\delta V = \frac{2V^2}{(E - E_{med})} \tag{5.6}$$

and using the relation eq. (4.2) the coupling strength V at ka is given by

$$V = \frac{1}{2}\frac{(ka)}{(ka)_0}\delta V_0, \tag{5.7}$$

where $(ka)_0$ and δV_0 are the size parameter where the closest encounter between two modes coupled to each other by the RADT is and the AC gap at $(ka)_0$.

We test the above result eq. (5.6) for the second order interactions, the interaction between $l = 2$ and $l = 4$ and the interaction between $l = 3$ and $l = 5$ at $\eta = 0.14$ shown in Fig. 5.2. The $l = 2$ and $l = 4$ mode groups are coupled via $l = 3$ mode group. At the closest encounter, $E_2 = E_4 \simeq 136.08$ and $E_3 \simeq 136.38$. Using the coupling strength data of the interactions

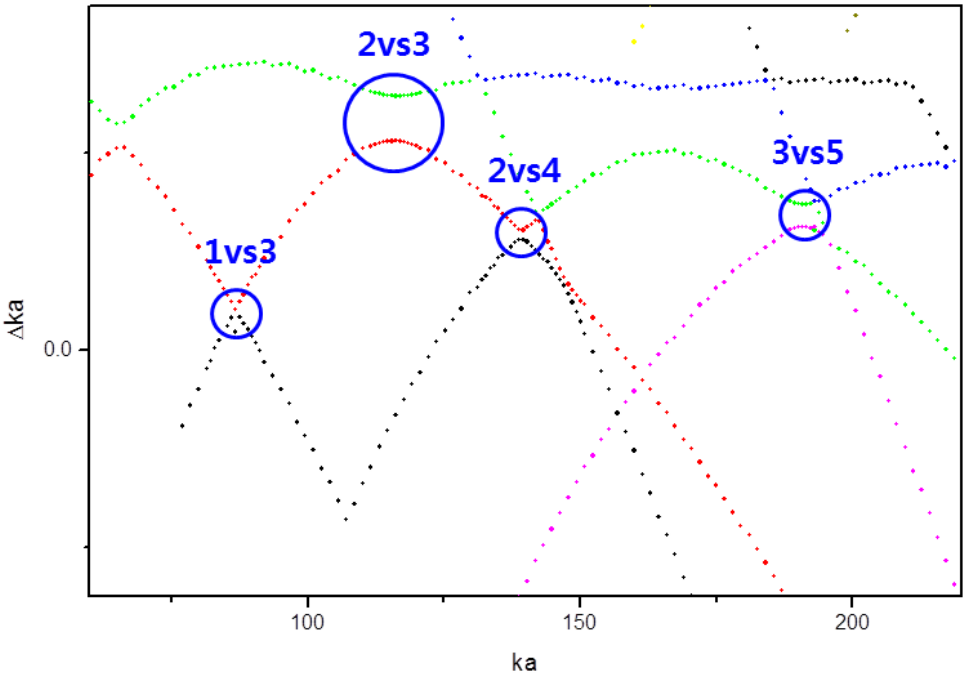

Figure 5.2: Mode evolution in the range from $ka \simeq 60$ to $ka \simeq 230$ at $\eta = 0.14$. The RADT relations are marked by red circles.

between $l = 2$ and $l = 3$ near $ka \simeq 115$, the theoretical prediction of the AC gap between $l = 2$ and $l = 4$ mode groups is $\delta V_{2n4} \simeq 0.0189$. The AC gap measured from the numerical calculation is about $\Delta(ka)_{2n4} \simeq 0.019$. In the same way, for the interaction between $l = 3$ and $l = 5$ mode groups, the theoretical prediction of the AC gap is about $\delta V_{3n5} \simeq 0.0393$ and the AC gaps by the numerical simulation is $\Delta(ka)_{3n5} \simeq 0.045$. The theoretical results are well matched with the numerical results.

The higher order interactions can be derived in the similar way using the eq. (4.2). In principle, all of the interaction strengths can be predicted. It sheds light on reconstructing the interaction Hamiltonian.

Chapter 6

Conclusion

In this work, we found that the RADT theory can be applied to the strong interactions between the unperturbed-basis modes. For strong interactions, the Husimi functions are well localized along the stable closed orbit or the unstable closed orbit which is related to the classical resonance. It implies the relevance between strong interactions and the RADT. Also, we confirmed that the angular mode index difference between the unperturbed-basis modes experiencing the strong interaction is the integer multiple of the number of the island in the resonance chain structure. This *selection rule* is one of the predictions of the RADT theory.

Another prediction of the RADT theory is that the coupling strength is proportional to the square of the area of the associated resonance structure on the PSOS. We performed the experiment measuring the AC gap between $l = 2$ and $l = 3$ mode groups with varying the deformation parameter and confirmed that the experimentally measured AC gaps follow the predictions of the RADT theory. Also, for the RADT related interactions between other

mode groups, the AC gaps measured by the numerical simulation confirmed the S^2 curve. Then, we found that the coupling strength of the resonance-assisted interactions related to the identical non-linear resonance structure on the phase space is proportional to the size parameter.

This work reveals the underlying semi-classical background for the unperturbed-basis mode interactions. Using the RADT theory, we expect to reconstruct the interaction Hamiltonian. Also, without the knowledge of the Hamiltonian structure, we can obtain the information of the coupling strength by just inspecting the phase space structure.

Appendix A

Husimi function exchange around the closest encounter

In this appendix, we present the Husimi functions around the closet encounter of weak and strong interactions. The inteactions of l=2 and 3 modes, l=3 and 4 modes and l=2 and 4 modes are related to the $p = 6$ resonant tori. Particulary, the interaction between l=2 and 4 modes is the *second order* interaction because $\Delta m = 12$. In Fig. A.3, the 2 lateral intensity modulations per each stable or unstable periodic orbits are shown.

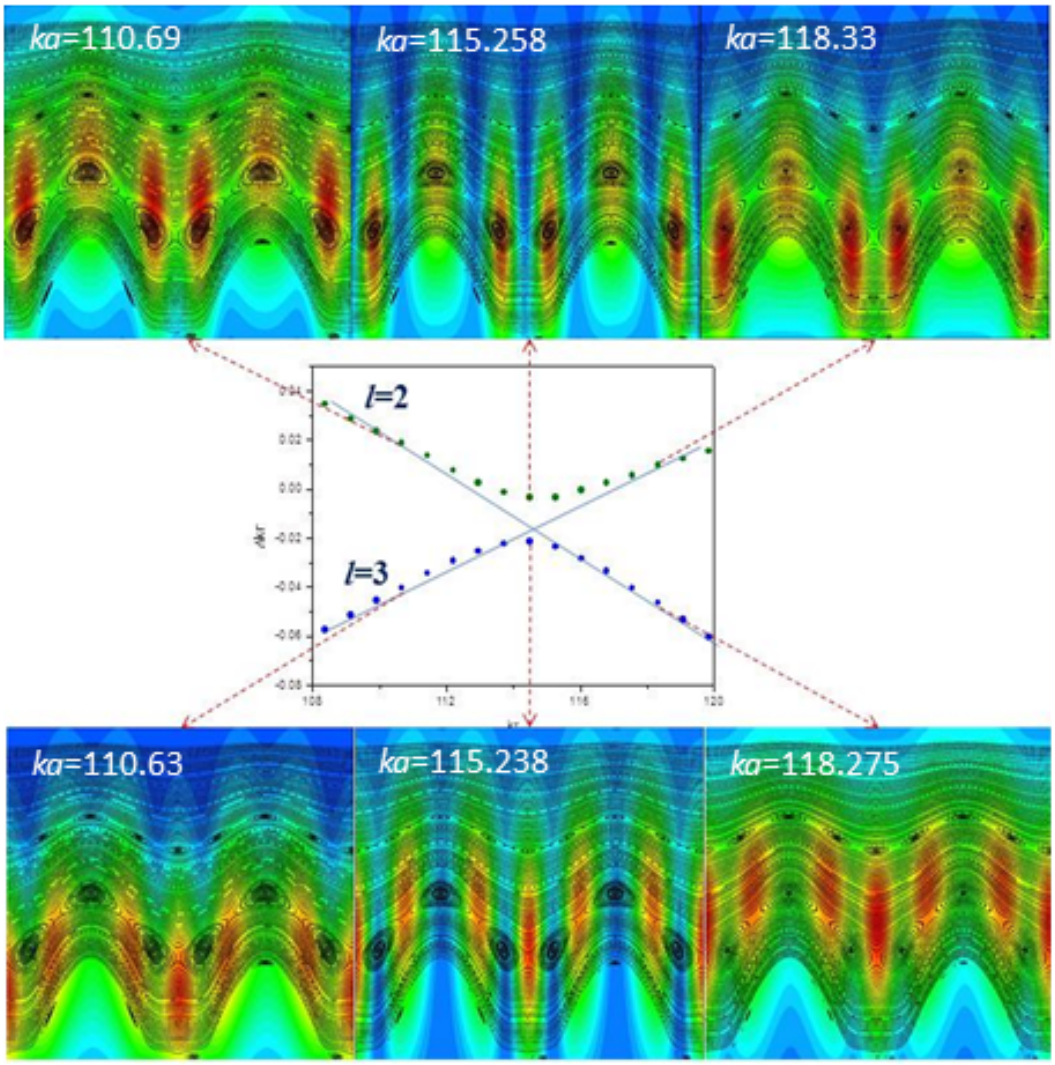

Figure A.1: Relative frequencies of l=2 and 3 modes near the AC region and the Husimi plots of the two modes at the closest encounter, marked by dashed arrows, when $\eta = 0.08$.

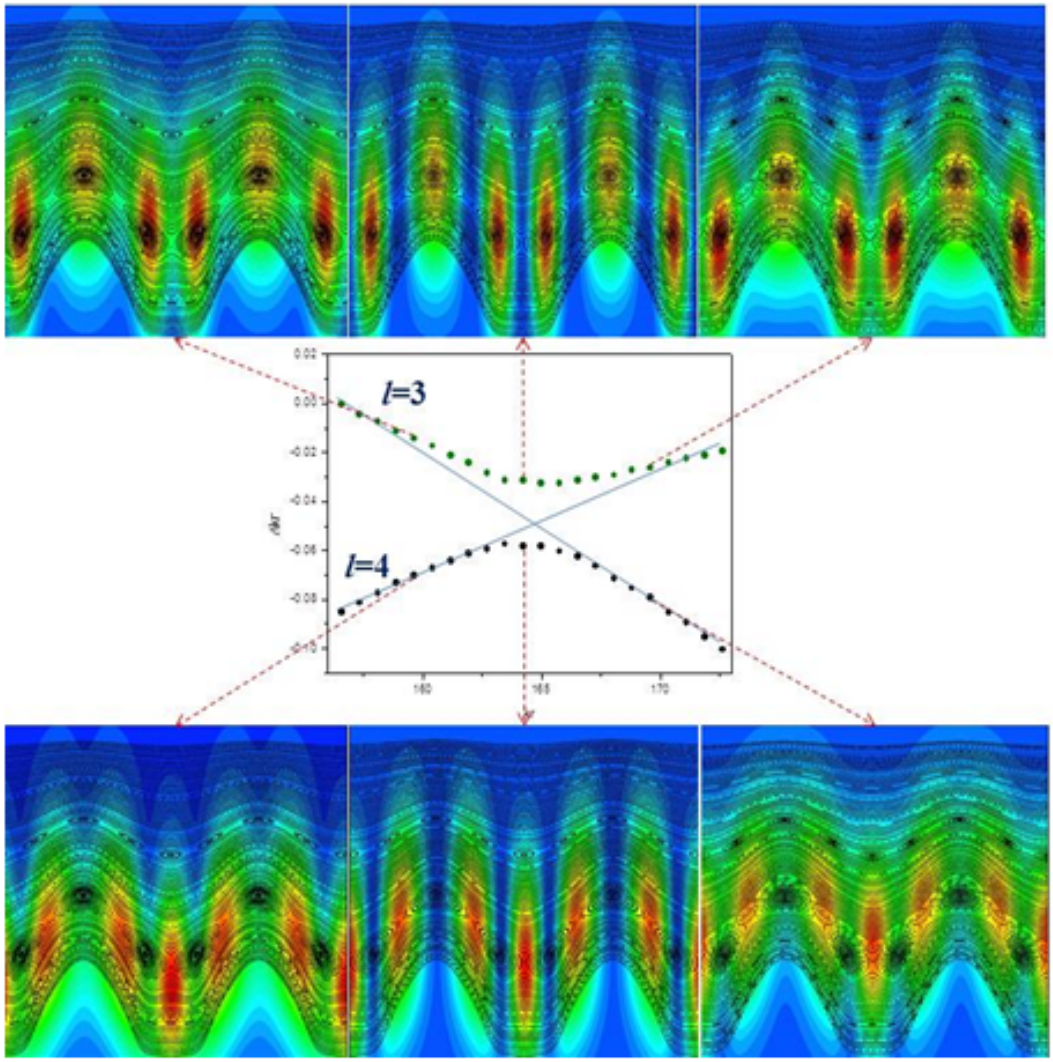

Figure A.2: Relative frequencies of l=3 and 4 modes near the AC region and the Husimi plots of the two modes at the closest encounter, marked by dashed arrows, when $\eta = 0.08$.

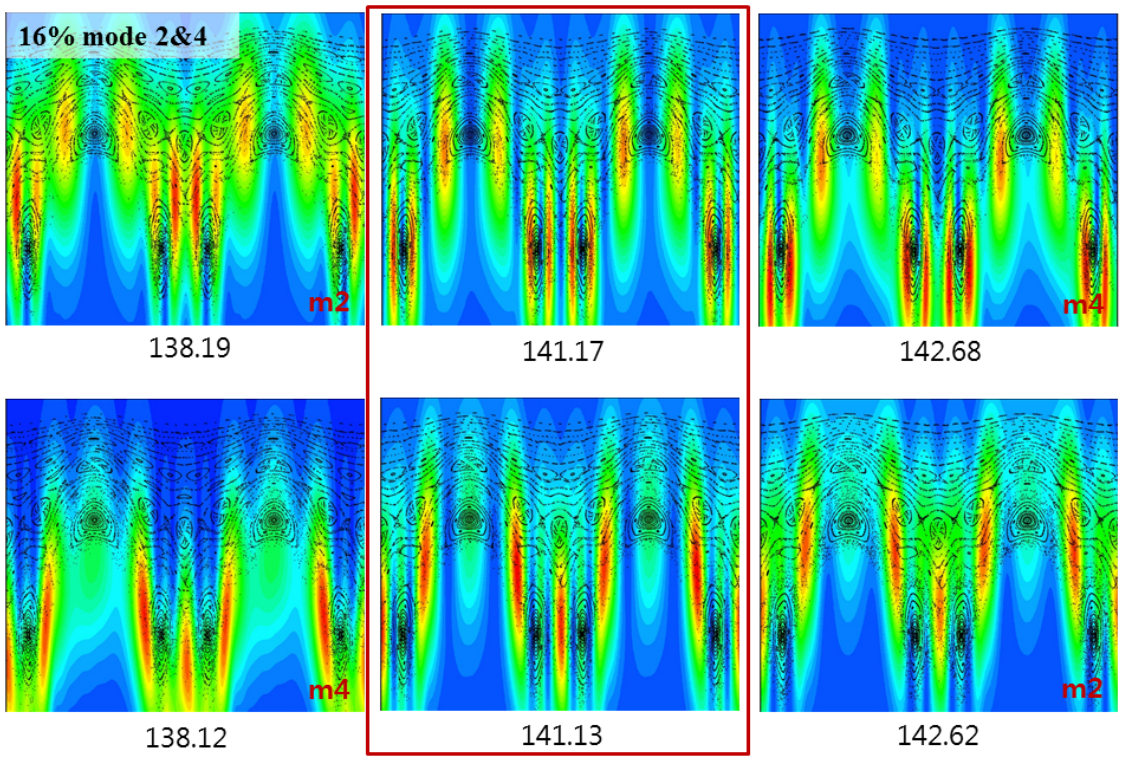

Figure A.3: The Husimi plots of l=2 and 4 modes around the closest encounter, marked by dashed arrows, when $\eta = 0.16$. The Husimi functions in the red rectangle are at the closest encounter.

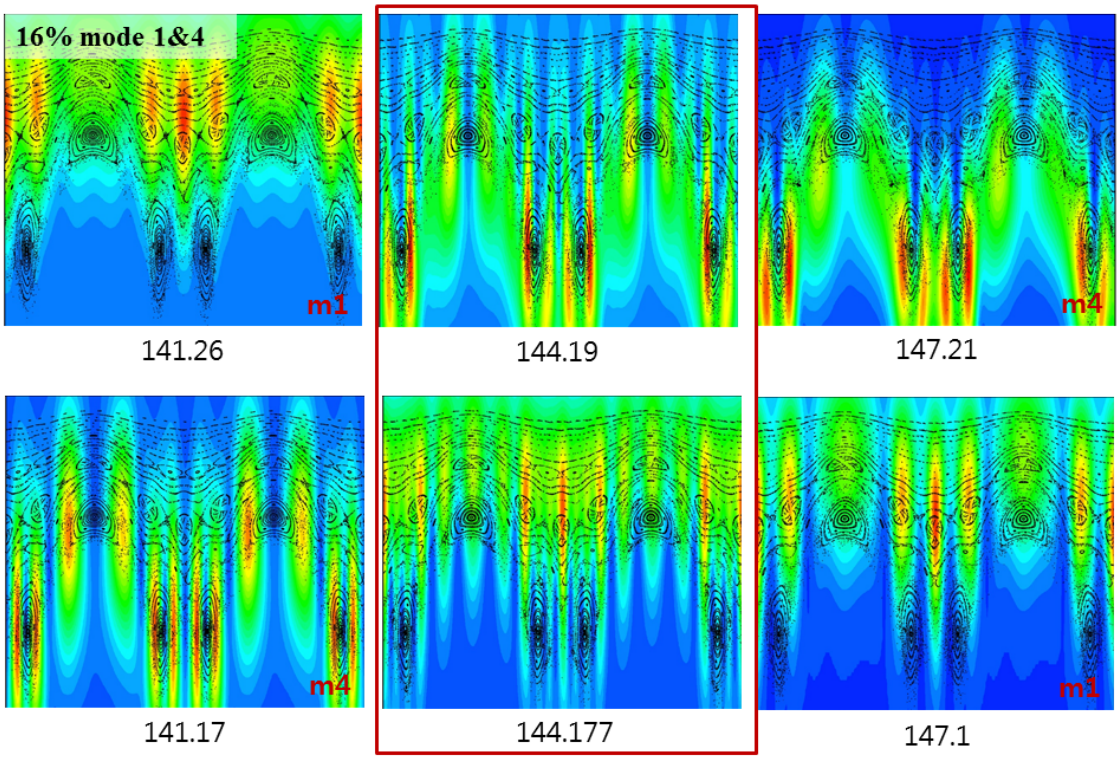

Figure A.4: The Husimi plots of l=1 and 2 modes around the closest encounter, marked by dashed arrows, when $\eta = 0.16$. The Husimi functions in the red rectangle are at the closest encounter.

Appendix B

Acoustic Cavity

The characteristics of quasi-eigenmodes are mainly studied in terms of the far-field pattern or the emission spectra. Although it is well known that spatial mode distributions show interesting features [51, 57, 52], it is so hard to measure the spatial mode pattern in non-destructive way because the measurement needs the scattering of light in the cavity [58].

This limitation can be supplemented by noting that ultrasonic pressure field in a water-filled metal cavity satisfies the same form of the wave equation (Helmholtz equation) and the boundary condition similar to the optical field in the microcavity. Also, the spatial pressure field distribution in water can be easily measured by the schlieren method which is widely used to visualize the density modulation in a transparent medium [60, 61].

In this appendix, we introduce the schlieren method which is an experimental tool for measuring the spatial mode pattern and the resonance frequency of acoustic modes. Also, the theoretical description of the acoustic wave will be given for calculating acoustic modes in a given geometry. Then,

we apply the experimental and the theoretical tools to study the acoustic circular shell cavity which is one of the most simple type of an acoustic cavity. Our works might serve as a foundation for future researches of acoustic cavities.

B.1 Shlieren method

The schlieren method is a useful optical tool for visualize the refractive index modulation in a transverse 2D plane. The electric field of the parallel light passing through a transparent medium (Fig. B.1) can be described as [59]

$$E_0(x,y) = A_0 \exp\left[i\psi(x,y)\right] \simeq A_0[1 + i\psi(x,y)] \tag{B.1}$$

where $\psi(x,y)$ is the phase variation of the electric field due to the change of the optical path length which is proportional to the refractive index at the passing position. Then, on the Fourier plane, the electric field is given as

$$\begin{aligned} E_0(f_x, f_y) &= A_0 \int E_0(x,y) \exp\left[2\pi i(f_x x + f_y y)\right] dxdy \\ &= A_0 \int \exp\left[2\pi i(f_x x + f_y y)\right] dxdy + iA_0 \int \psi(x,y) \exp\left[2\pi i(f_x x + f_y y)\right] dxdy, \end{aligned}$$

where the first term of rhs of the second equation is given by the non-interactive parallel light and the second term is due to the diffracted light by the refractive index modulation. Then, the first term can be removed using the 'black spot' at the center of the Fourier plane which filters the parallel light. So, at the image plane behind the Fourier plane, the image of the diffracted light by the refractive index modulation is formed with the

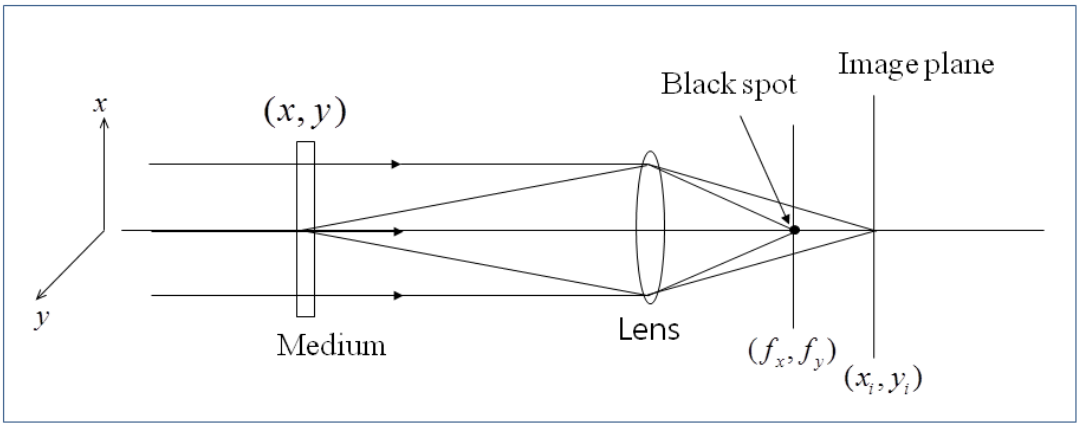

Figure B.1: Schematic view of the schlieren method [59].

spatial intensity distribution,

$$I_0(x_i, y_i) = I_0\psi^2(x_i, y_i). \tag{B.2}$$

In our experiments, we make an acoustic cavity by drilling a hole in aluminium bulk using a computerized numerical control technique to make a hole having the boundary shape what we want mathematically and test it by submerging the holed bulk in water (Fig. B.2). Then, the acoustic cavity becomes a shell type cavity where the inside is filled with water, the shell is comprised of aluminium and the outside of the shell is filled with water. Similar to the electromagnetic wave, the refractive index for the acoustic wave can be defined by its wave length. For a given frequency, the wavelength is determined by its propagation speed, $\lambda = f/c$. The refractive

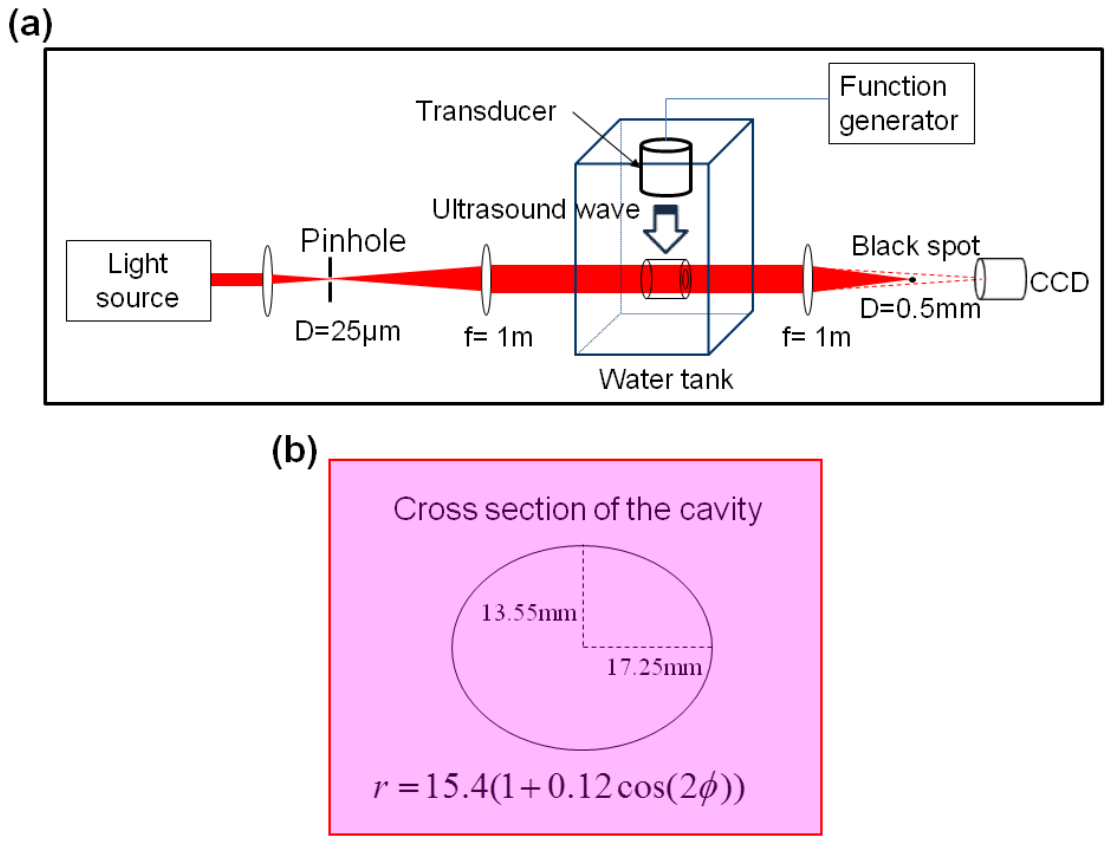

Figure B.2: (a) Experimental setup using the schlieren method. (b) The cross section of an acoustic cavity.

index is inversely proportional to the wavelength. The speed of sound in water is 1433 m/s, the speed of the logitudinal wave in aluminium is 6374 m/s and the speed of the transverse wave is 3111 m/s. So the refractive index of water for the sound wave is lager than both the waves in aluminium.

The example of the visualized mode patterns using the schlieren method are shown in Fig. B.3 for the cavity of the inner boundary shape given by Fig. B.2(b). The boundary shape is quadrupole described as $r(\theta) = 15.2(mm)(1 + 0.12\cos 2\theta)$ in a polar coordinate. We excite this acoustic cavity as varying the excitation frequency. When the excitation frequency is resonant with one of acoustic cavity modes, then mode is strongly excited. Excited modes are well localized along the classical period-4 orbits. The upper two modes in Fig. B.3 corresponds to the stable periodic orbit marked by red empty circles on the PSOS in Fig. B.4 and the lower two modes corresponds to the unstable orbit marked by solid blue circles. Since the lower two modes are localized along the unstable and the classically zero probability trajectory, they are *scar* modes.

B.2 Wave equation of the acoustic wave

The pressure field in water can be described as [62]

$$p = P - P_0 \simeq (\frac{\partial P}{\partial \rho})(\rho - \rho_0) = B(\frac{\rho - \rho_0}{\rho_0}) \tag{B.3}$$

for the small change of the pressure, where P is the pressure, P_0 is the pressure at the equilibrium, p is the relative pressure, B is the bulk modulus, ρ is the density of water and ρ_0 is the water density at the equilibrium. Then,

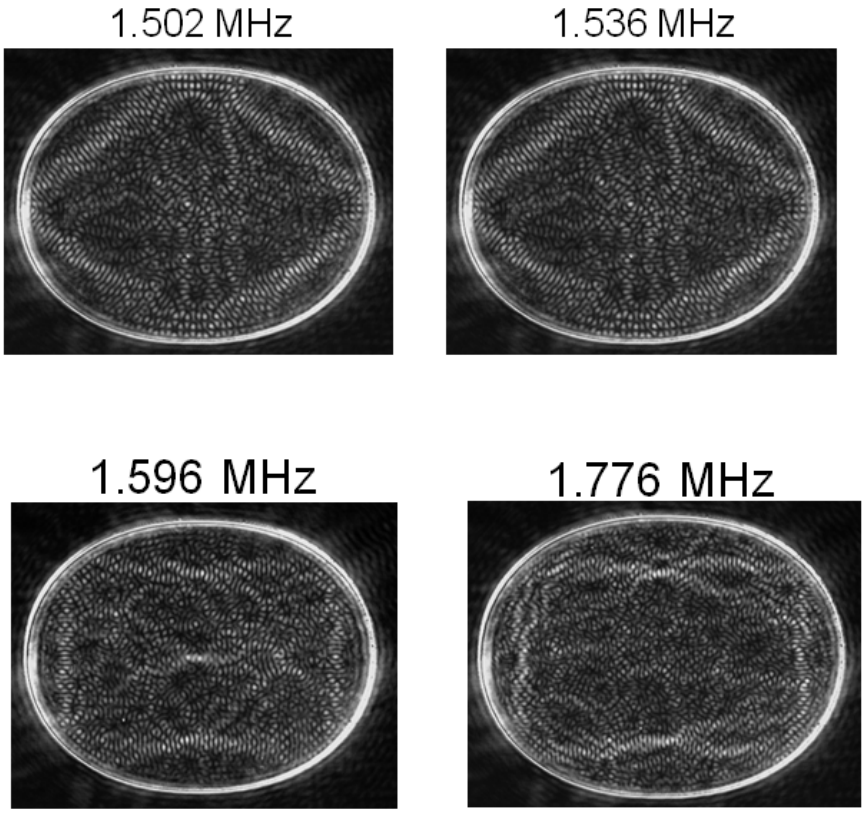

Figure B.3: Visualized mode patterns for a quadrupole cavity of $\eta = 0.12$ and the excitation frequencies

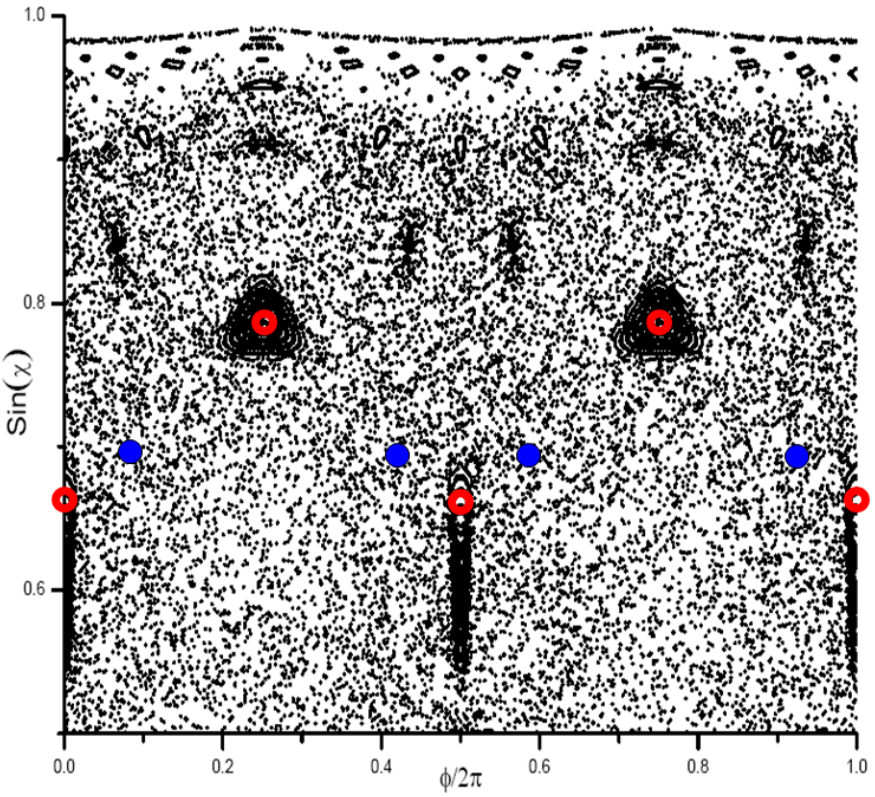

Figure B.4: PSOS for the quadrupole boundary at $\eta = 0.12$. The stable period-4 orbit is marked by red empty circles and the unstable period-4 orbit is marked by blue solid circles.

using the one-dimensional continuity equation,

$$\frac{\partial \rho}{\partial t} + \frac{\partial}{\partial x}(\rho u) = 0$$
$$\Rightarrow \frac{\partial s}{\partial t} + \frac{\partial}{\partial x} u \simeq 0,$$

where $s = \frac{\rho - \rho_0}{\rho_0}$ is the condensation and using the one-dimensional Euler's force equation,

$$\rho \frac{du}{dt} + \frac{\partial P}{\partial x} = 0$$
$$\Rightarrow \rho_0 \frac{\partial u}{\partial t} + \frac{\partial p}{\partial x} \simeq 0,$$

we can find the wave equation for the pressure field in one dimension,

$$\frac{\partial^2 p}{\partial x^2} - \frac{\rho_0}{B} \frac{\partial^2 p}{\partial t^2} = 0. \tag{B.4}$$

This equation can be generalized for 3 dimension as,

$$\nabla^2 p - \frac{1}{c^2} \frac{\partial^2 p}{\partial t^2} = 0, \tag{B.5}$$

where $c = \sqrt{\frac{B}{\rho_0}}$. If we assume that the pressure field is the monochromatic wave described as $p(\boldsymbol{r}, t) = p(\boldsymbol{r}) \exp(iwt)$, then, the above equation is rewritten as

$$\nabla^2 p(\boldsymbol{r}) + \frac{w^2}{c^2} p(\boldsymbol{r}) = 0 \tag{B.6}$$

This is the Helmholtz equation equal to the optical wave. Accordingly, the characteristics of acoustic wave in a water cavity might have many similarities with the optical wave.

The wave equation in solid such as aluminium for which we must consider the shear force is derived by the Newton's law. The stress tensor is described

as [62]

$$\sigma_{ij} = \lambda \frac{\partial u_k}{\partial x_k} \delta_{ij} + \mu \left(\frac{\partial u_i}{\partial x_j} + \frac{\partial u_j}{\partial x_j} \right), \tag{B.7}$$

where $\boldsymbol{u}$ is the displacement vector, λ is the Lame constant and μ is the shear modulus. Then, ignoring the external force, the Newton's equation can be written as,

$$\frac{\partial \sigma_{ij}}{\partial x_i} = \rho \ddot{u}_j. \tag{B.8}$$

Introducing the potentials ϕ and ψ satisfying the relations,

$$\boldsymbol{v} = \boldsymbol{v}_l + \boldsymbol{v}_t \tag{B.9}$$

where $\boldsymbol{v}_l$ and $\boldsymbol{v}_t$ are the velocity vectors for the longitudinal wave and transverse wave and

$$\boldsymbol{v}_l = \nabla \phi \qquad \boldsymbol{v}_t = \nabla \times \psi, \tag{B.10}$$

eq. (B.7) can be arranged so that each potential function satisfies the Helmholtz equation, respectively such that

$$\nabla^2 \phi + k_l^2 \phi = 0 \tag{B.11}$$

$$\nabla^2 \psi + k_t^2 \psi = 0 \tag{B.12}$$

The amplitude of each function might be determined by the boundary conditions.

Because the elastic wave in solid is described as the sum of two kinds of wave, we need 3 boundary conditions for solving the wave equation of the acoustic wave. The two boundary conditions are the continuity of the surface normal force and the continuity of the surface normal displacement [63]. Another boundary condition is the continuity of the shear force at the

interface, but the shear force is zero in water so the third condition is the zero shear force at the boundary.

B.3 Acoustic circular shell cavity

In this section, we study an acoustic circular shell cavity using the experimental and the theoretical method. By implementing the schlieren method, we can experimentally easily visualize the spatial mode patterns. Also, the spectrum of an acoustic cavity can be measured by sweeping the exciting frequency and the integrating the intensity of the visualized mode pattern image. For an example, the spectrum of a concentric circular shell cavity is given in Fig. B.5. The aluminium shell submerges in water and the outer radius of the shell is 12 times lager than the inner radius as shown in the inset of the figure. The angular mode index and the radial mode index corresponding to a peak in spectrum can be identified by measuring the spatial mode pattern at the frequency as shown in Fig. B.6. By counting the intensity maximum along the radial direction and the boundary, we can measure the mode index. We indicate the mode index as (angular mode index, radial mode index) above spectrum peaks in Fig. B.5.

Schlieren method can visualize the density modulation in a transparent medium, so the elastic wave in aluminium can not be measured. However,

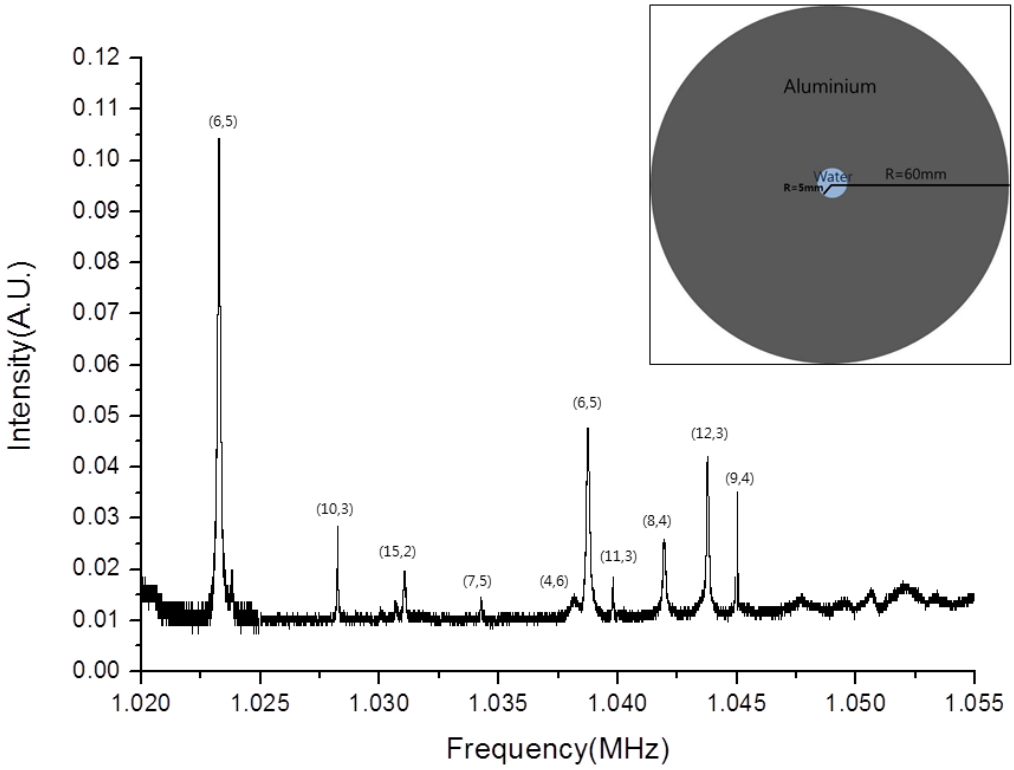

Figure B.5: Spectrum for an concentric circular shell cavity in the range of the exciting frequency from 1.02MHz to 1.055MHz. (inset) Cross-section of an acoustic cavity

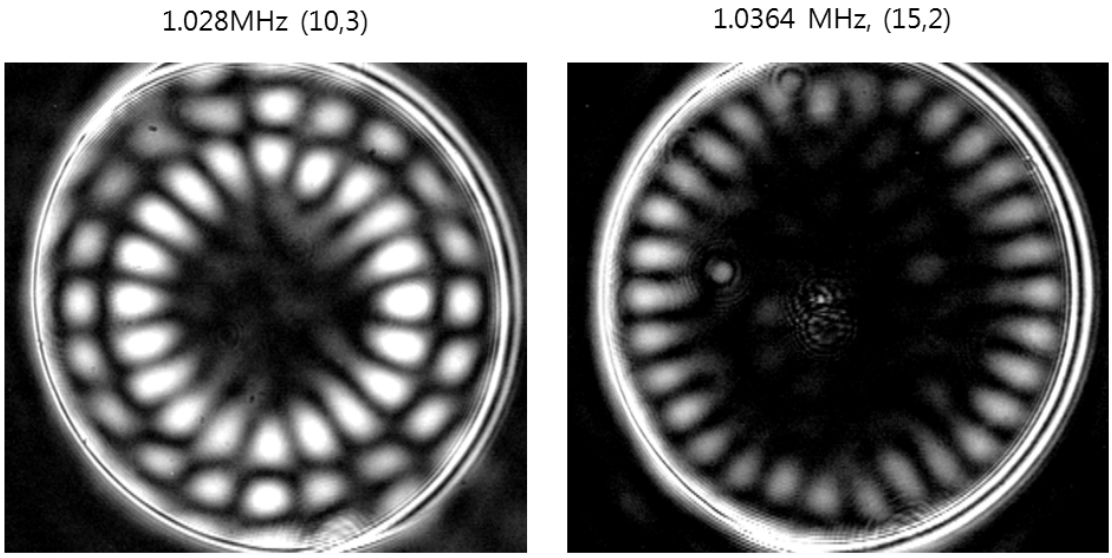

Figure B.6: Spatial mode patterns in water corresponding to (10,3) and (15,2) in Fig. B.5.

we should also consider the aluminium shell to study the mode characteristics of a shell cavity. So, we need to supplement this limitation using the theoretical method.

At the inner and the outer boundary of a concentric circular shell cavity, three boundary conditions between water and aluminium are given as

$$\sigma_{r\theta} = 0$$

$$\sigma_{rr} = -p$$

$$u_r^{al} = u_r^{wat}$$

where $u_r^{wat} = \frac{1}{\rho_w w^2}\frac{\partial p}{\partial r}$. Also, the fields in each region is given by,

$$P_{in} = \sum A_m J_m(k_w r)(\frac{\cos m\theta}{\sin m\theta})$$

in the inner water region,

$$\phi = \sum [B_m J_m(k_l r) + C_m N_m(k_l r)](\frac{\cos m\theta}{\sin m\theta})$$
$$\psi = \sum [D_m J_m(k_t r) + E_m N_m(k_t r)](\frac{\sin m\theta}{-\cos m\theta})$$

in the aluminium shell and applying the outgoing boundary condition,

$$P_{out} \sum F_m H_m^{(1)}(k_w r)(\frac{\cos m\theta}{sinm\theta}) \tag{B.13}$$

in the outer water region. We can use 6 boundary condition equations for two boundaries, the inner and the out boundary of the shell. So, the equations can be arranged to the homogeneous 6×6 matrix equation and the eigenvalues are the wavevector k making the determinant zero.

We calculate the eigenvalues and the eigenvectors of $m = 15$ modes in a concentric circular cavity for $R = 3r$ where R is the outer radius and the

r is the inner radius. The eigenvalues are described in terms of $k_w r$ where k_w is the wavevector in water. Fig. B.7 shows the cross-section view of the cavity, the eigenvalues and the corresponding spatial mode distributions. Inspecting the spatial patterns, we can distinguish two kinds of modes by the spatial mode distribution. The spatial distributions of modes of $kr = 16.613$ and $kr = 21.808$ are mainly in the inner water region but others are distributed in the aluminium region.

For comparisons, we also calculate the eigenvalues and the mode patterns for a circular water cavity of the radius r surrounded by aluminium (Fig. B.8) and for a circular aluminium cavity of the radius R surrounded by water (Fig. B.9). As you can see, the eigenvalues and the mode patterns of the first kind modes of the shell cavity are similar to the characteristics of the water cavity modes and the second kind modes of the shell cavity resemble with aluminium cavity modes. That is, the shell cavity modes can be classified as the water based mode (WBM) and the solid based mode (SBM) by their origin.

For more investigations, we searched a shell cavity by adjusting the outer shell radius. Since the eigenvalues are defined in terms of the inner radius, the eigenvalues of water cavity modes are not changed by varying the

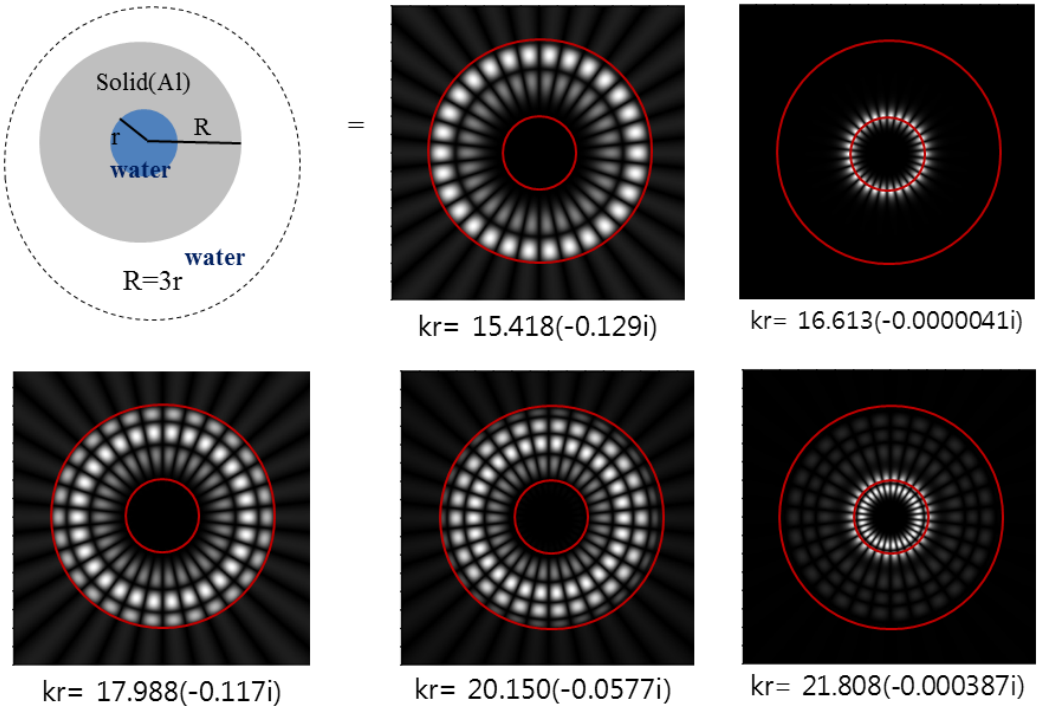

Figure B.7: The eigenvalues and the spatial mode pattern of an concentric circular shell cavity of $R = 3r$.

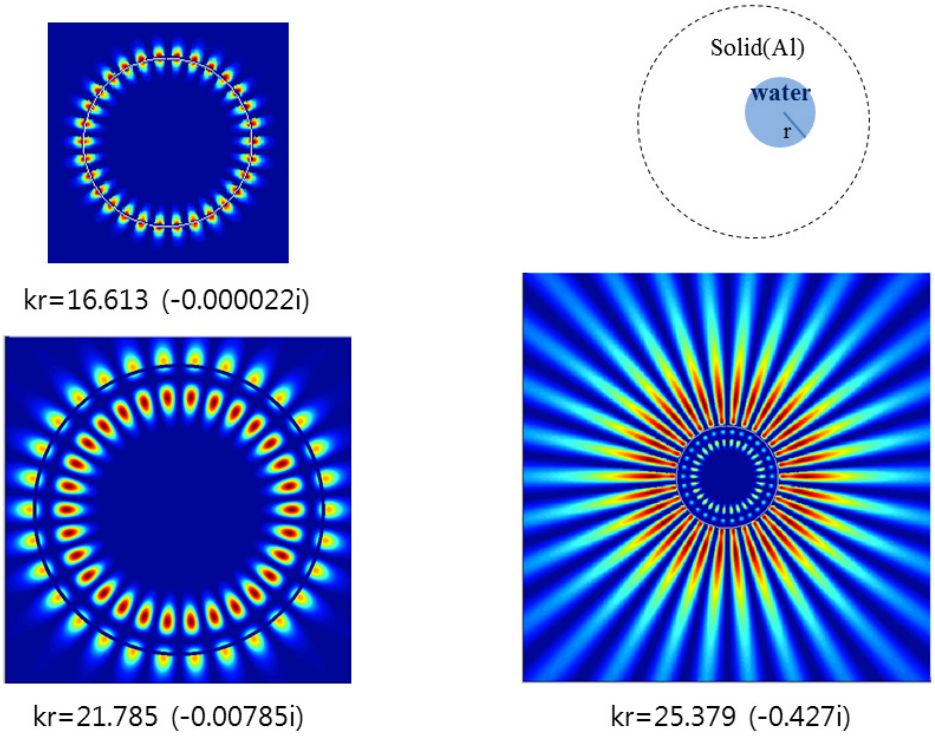

Figure B.8: The eigenvalues and the spatial mode pattern of a circular water cavity of the radius r surrounded by aluminium.

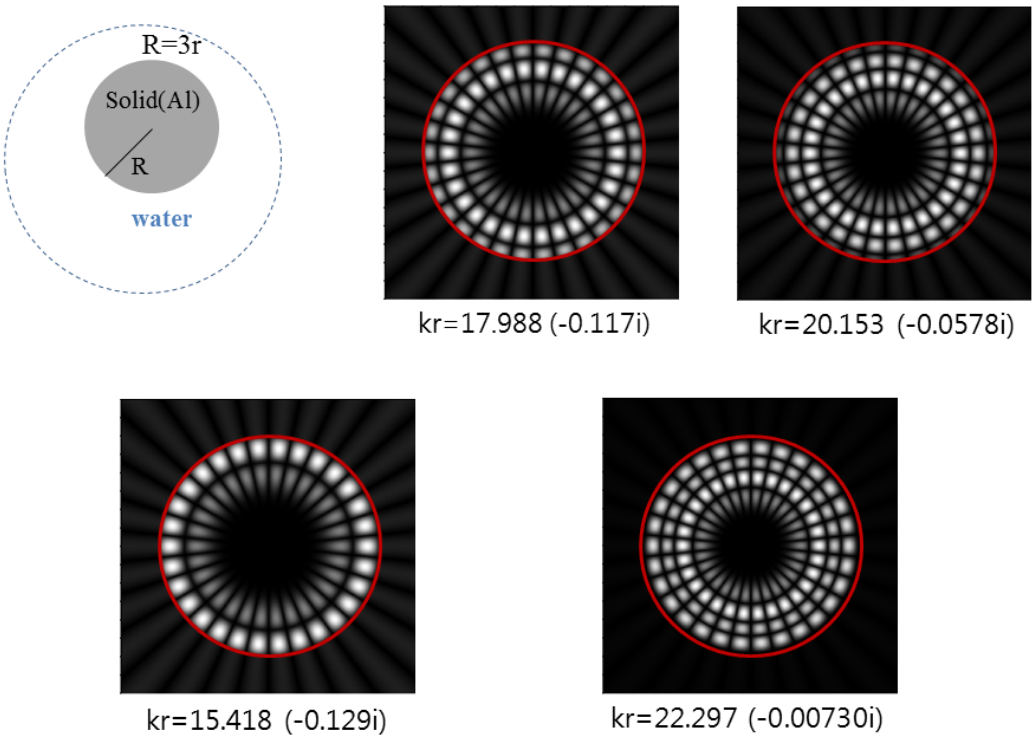

Figure B.9: The eigenvalues and the spatial mode pattern of a circular aluminium cavity of the radius R surrounded by water.

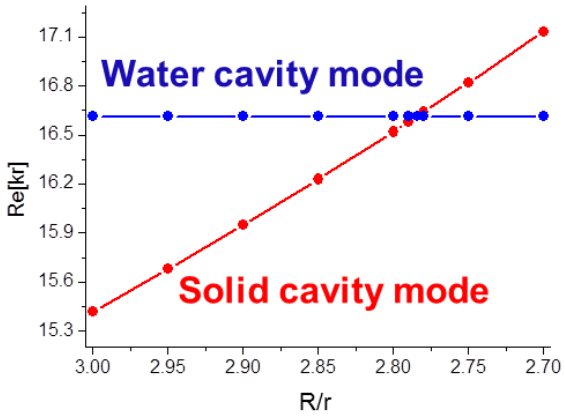

Figure B.10: The change of the eigenvalues of a water cavity mode and a solid cavity mode as varying the outer radius R.

outer radius. However, the eigenvalues of solid cavity modes are inversely proportional to the outer radius as shown in Fig. B.10. Also, WBMs and SBMs are affected in the similar way by adjusting the outer radius. Then, by decreasing the outer radius, we can make WBMs and SBMs encounter each other.

Fig. B.11, Fig. B.12 and Fig. B.13 show the real part of the eigenvalue and the Q-factor of water modes of $m = 15$ and $l = 1, 2, 3$ near the closest encounter with SBM modes. For (15,1) water mode and SBM, they show the crossing of the real eigenvalues and the avoided crossing the imaginary part of the eigenvalues. But, for (15,2) and (15,2) water modes, they show the avoided crossing with SBMs. The coupling strength between a WBM and a SBM increases as the radial mode number increases. It is the expected

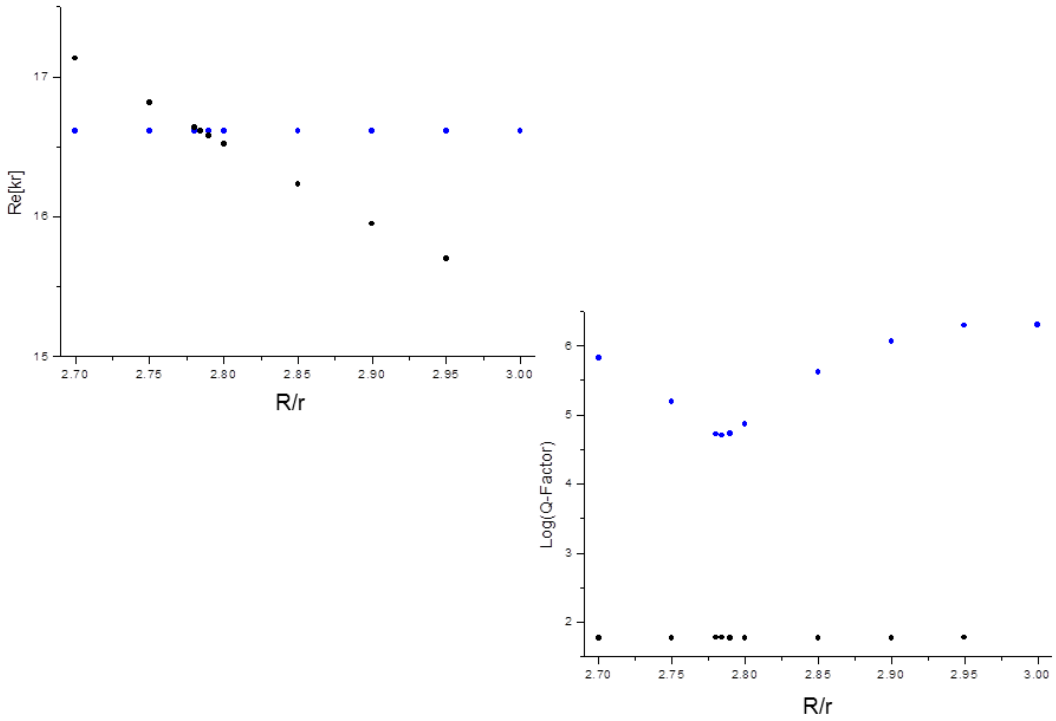

Figure B.11: The real part of the eigenvalue and the log plot of the Q-factor near the closest encounter of the (15,1) WBM mode with SBM

result because the tunneling rate of WBM increases for a large radial number mode, (the Q-factor of WBM decreases as l increases) and it results in the increase of the coupling strength.

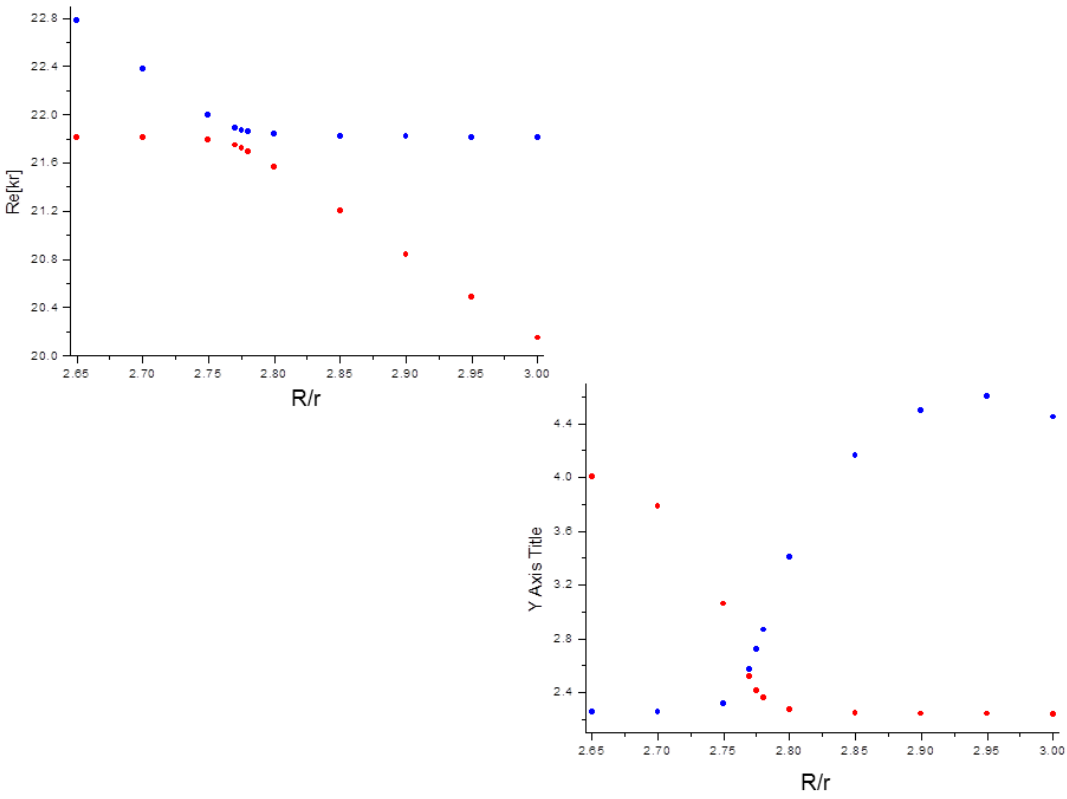

Figure B.12: The real part of the eigenvalue and the log plot of the Q-factor near the closest encounter of the (15,2) WBM mode with SBM

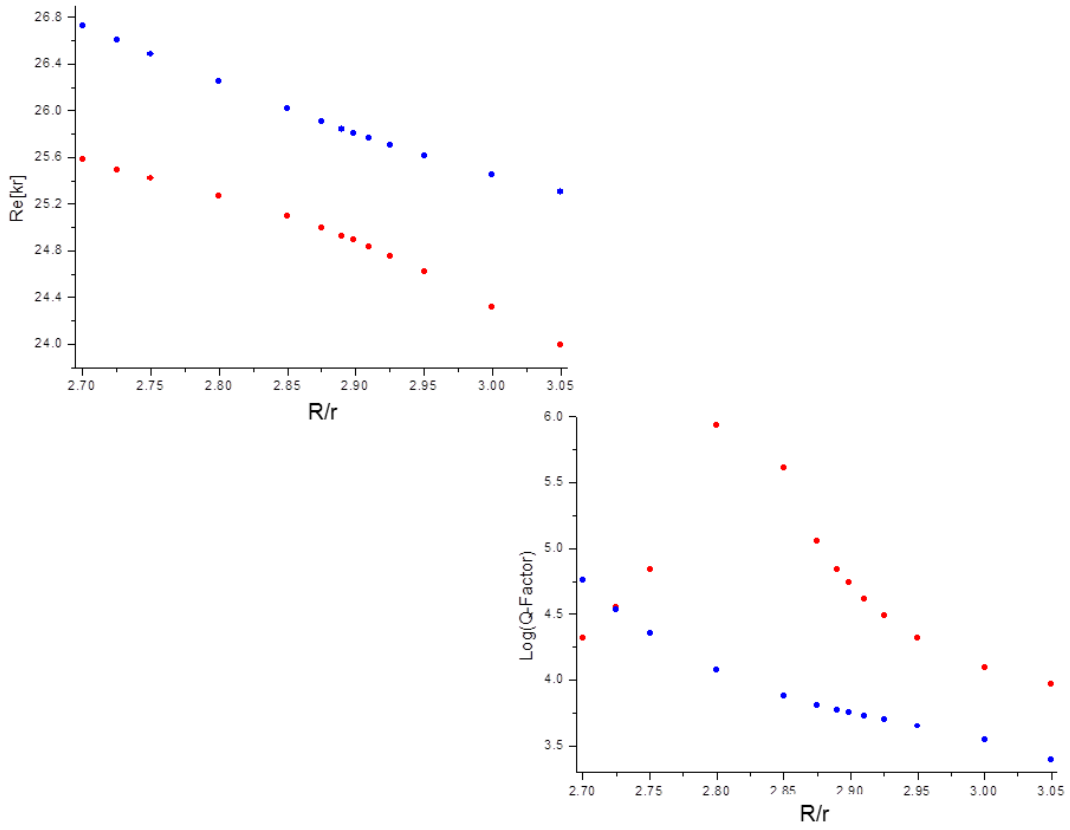

Figure B.13: The real part of the eigenvalue and the log plot of the Q-factor near the closest encounter of the (15,3) WBM mode with SBM

Also, we perform similar calculations by changing the angular mode index for the fixed radial mode index, especially for $l = 2$ because the spatial mode patterns of $l = 2$ mode group are well visualized by the schlieren method. Fig. B.14 shows the real part of the eigenvalues of WBMs for the $l = 2$ mode group. The modes from $m = 13$ to $m = 16$ show the avoided crossing and the modes of $m = 17$ and $m = 18$ show the crossing. So, we can guess that the position of the exceptional point locate between the closest encounter of $m = 16$ and $m = 17$, as marked by red circle in Fig. B.14. Also, as we expect, the coupling strength between SBMs and WBMs increases as the angular mode index decreases.

The calculated spatial mode patterns of the $m = 13$ and $m = 15$ shell mode groups are shown in Fig. B.15 and Fig. B.16. In these figures, we can confirm the mode mixing near the closest encounter and the mode exchange following the diabatic lines. Also, the intensity of the spatial mode pattern in the water region inside the shell is relatively strong for modes on the diabatic line of WBM and weak near the closest encounter. On the diabatic line of SBM, the mode patterns are not excited in the water region.

We can experimentally confirm the avoided crossing between WBMs and SBMs using the technique described before. The experimental results are

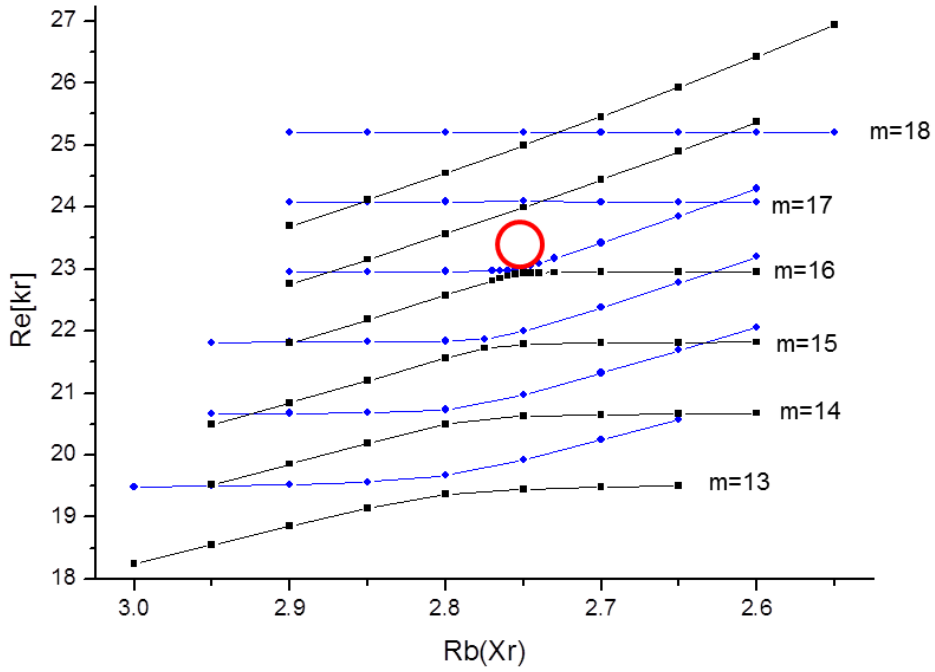

Figure B.14: The real part of the eigenvalues of WBMs for $l = 2$ and $m = 13 \sim m = 18$ near the closest encounter with SBMs. The position of the exceptional point is marked by red circle.

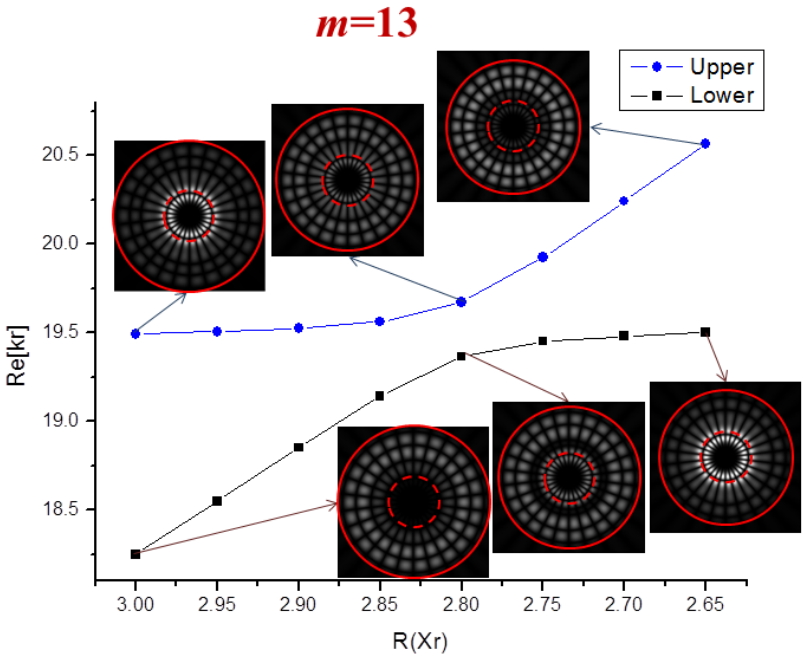

Figure B.15: The eigenvalues of WBMs and SBMs for $m = 13$ and the calculated normalized spatial mode patterns of corresponding to each eigenvalue.

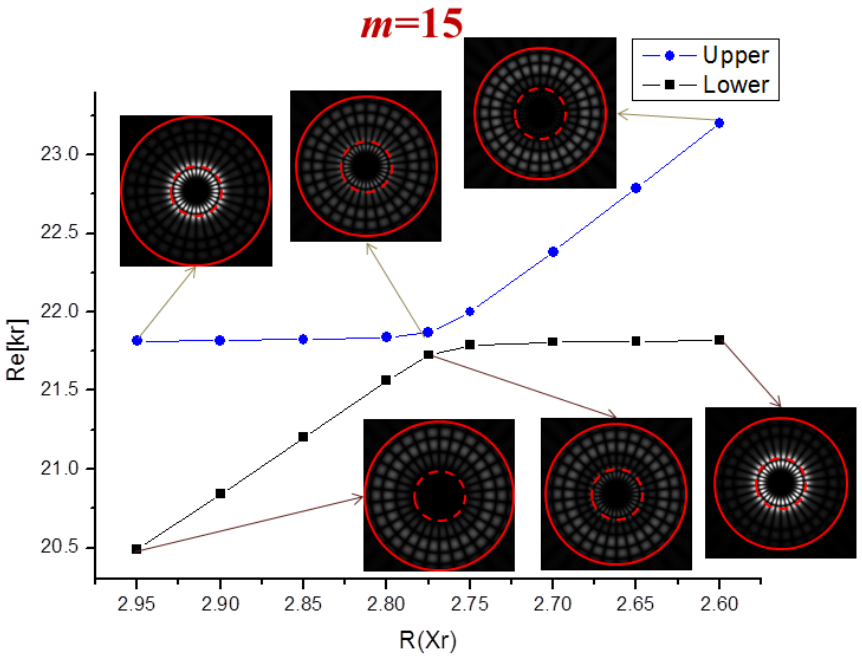

Figure B.16: The eigenvalues of WBMs and SBMs for $m = 15$ and the calculated normalized spatial mode patterns of corresponding to each eigenvalue.

shown in from Fig. B.17 to Fig. B.20 for from the $m = 11$ mode group to the $m = 14$ mode group. The eigenvalues are marked by solid black circle in each figure. For comparison, the calculated eigenvalues are also presented. (blue and red line). We can see that the experimental result well confirm the calculation. The experimentally measured spatial mode patterns in the water region inside the shell are also shown for several eigenvalues. As commented before, the intensity of spatial mode pattern is strong on the WBM diabatic line and the spatial mode patterns disappear on the SBM diabatic line.

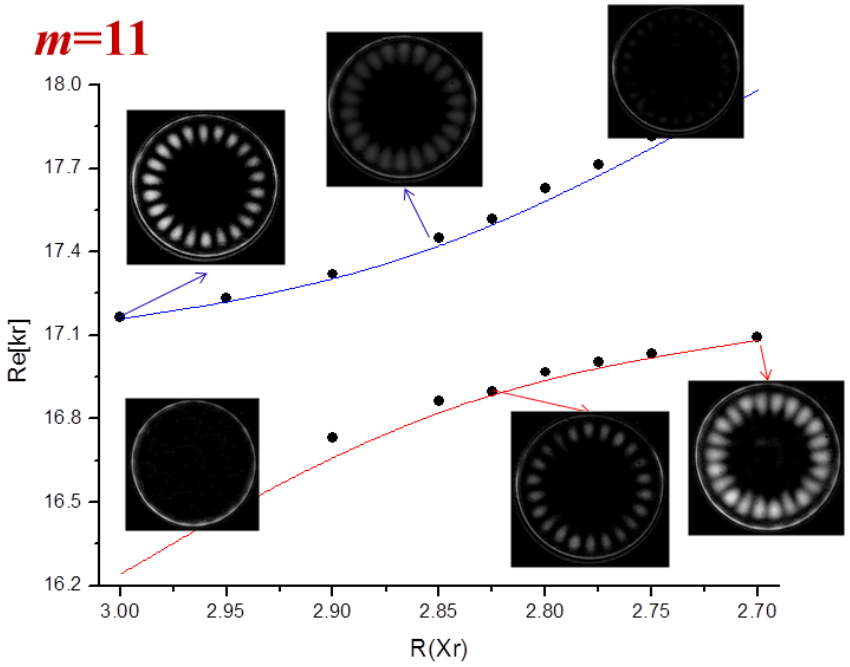

Figure B.17: The experimentally measured eigenvalues and the corresponding spatial mode patterns for $m = 11$ mode group.

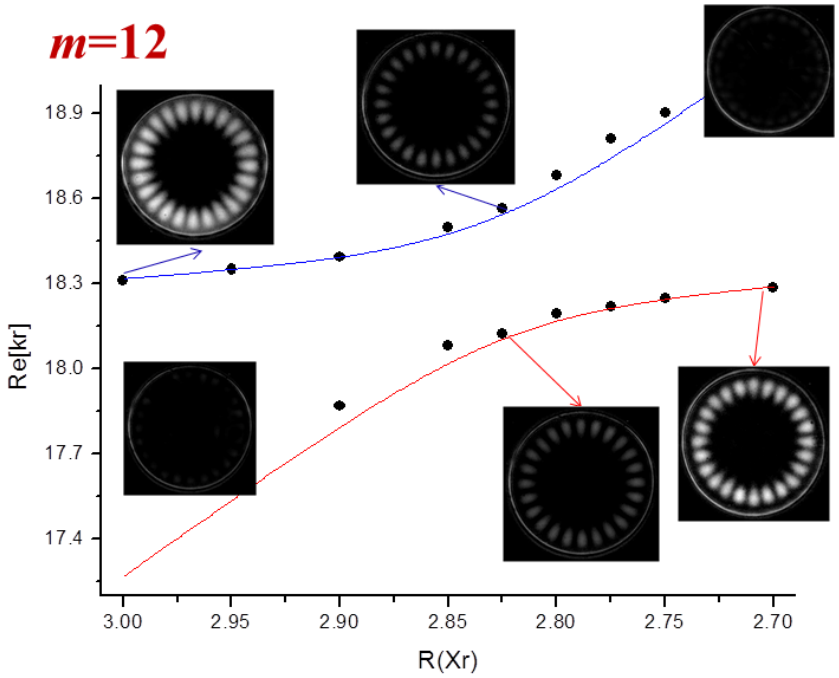

Figure B.18: The experimentally measured eigenvalues and the corresponding spatial mode patterns for $m = 12$ mode group.

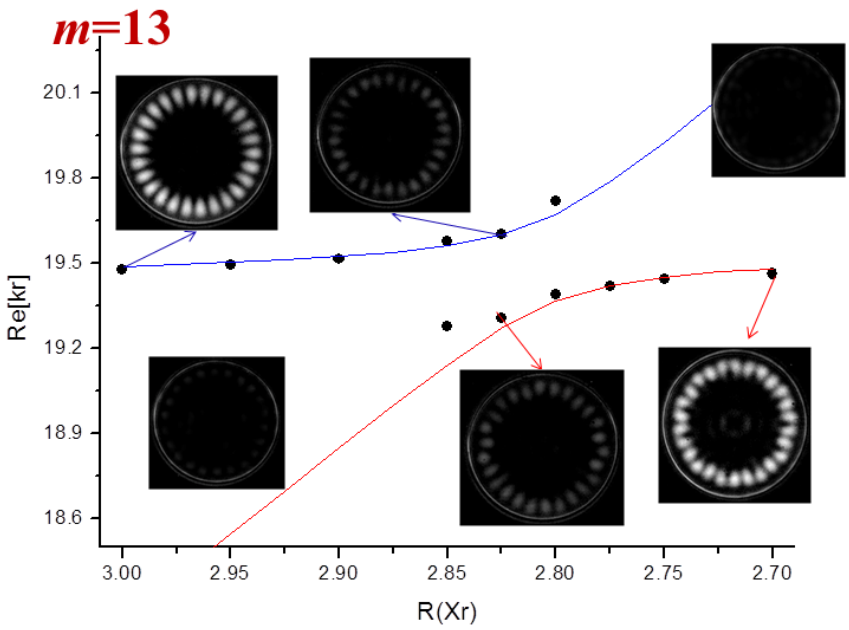

Figure B.19: The experimentally measured eigenvalues and the corresponding spatial mode patterns for $m = 13$ mode group.

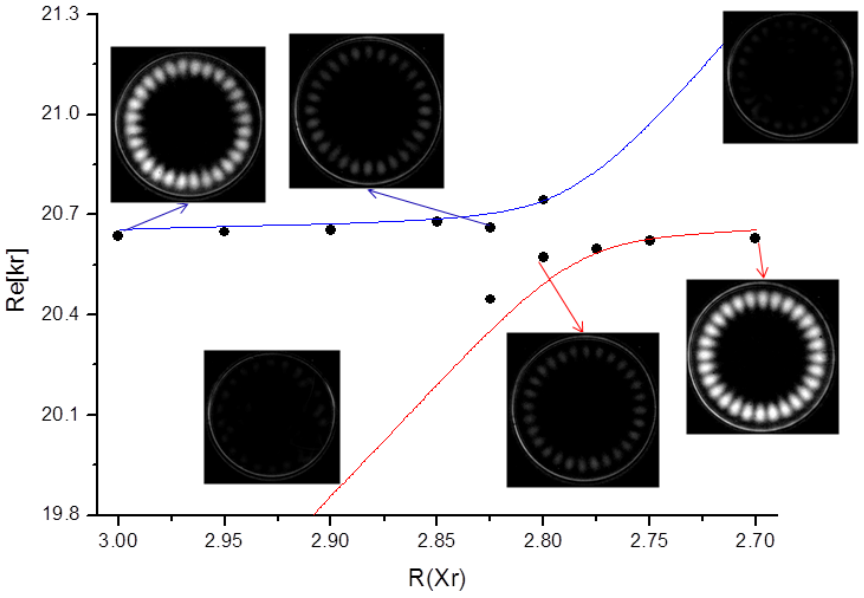

Figure B.20: The experimentally measured eigenvalues and the corresponding spatial mode patterns for $m = 14$ mode group.

Bibliography

[1] K. J. Vahala, Nature (London) **424**, 839 (2003).

[2] E. Moreau, I. Robert, J. M. Gérard, I. Abram, L. Manin, and V. Thierry-Mieg, Appl. Phys. Lett. **79**, 2865 (2001).

[3] S. M. Spillane, T. J. Kippenberg, and K. J. Vahala, Nature, **415**, 621 (2002).

[4] S. Suzuki, Y. Hatakeyama, Y. Kokubun, and S. T. Chu, J. Lightwave Technol. **20**, 745 (2002).

[5] A. M. Armani, R. P. Kulkarni, S. E. Fraser, R. C. Flagan, and K. J. Vahala, Science **317**, 783 (2007).

[6] P. Del'Haye, A. Schliesser, O. Arcizet, T. Wilken, R. Holzwarth, and T. J. Kippenberg, Nature **450**, 1214 (2007).

[7] A. Schliesser, R. Riviére, G. Anetsberger, O. Arcizet, and T. J. Kippenberg, Nature Physics **4**, 415 (2008).

[8] B. Min, E. Ostby, V. Sorger, E. Ulin-Avila, L. Yang, X. Zhang, and K. Vahala, Nature **457**, 455 (2009).

[9] J. U. Nöckel, A. D. Stone, G. C. Helene, L. Grossman, and R. K. Chang, Opt. Lett. **21**, 1609 (1996).

[10] S. Chang, R. K. Chang, A. D. Stone, and J. U. Nöckel, J. Opt. Soc. Am. B **17**, 1828 (2000).

[11] H. G. L. Schwefel, N. B. Rex, H. E. Tureci, R. K. Chang, and A. D. Stone, J. Opt. Soc. Am. B. **21**, 923 (2004).

[12] S.-B. Lee, J. Yang, S. Moon, J.-H. Lee, K. An, J.-B. Shim, H.-W. Lee, and S. W. Kim, Phys. Rev. A **75** 011802(R) (2007).

[13] W. A. Lin and L. E. Ballentine, Phys. Rev. Lett. **65**, 2927 (1990).

[14] O. Bohigas, S. Tomsovic, and D. Ullmo, Phys. Rep. **223**, 43 (1993).

[15] S. Tomsovic and D. Ullmo, Phys. Rev. E **50**, 145 (1994).

[16] D. A. Steck, W. H. Oskay and M. G. Raizen, Science **293**, 274 (2001).

[17] W. K. Hensinger, H. Häffner, A. Browaeys, N. R. Heckenberg, K. Helmerson, C. McKenzie, G. J. Milburn, W. D. Phillips, S. L. Rolston, H. Rubinsztein-Dunlop and B. Upcroft, Nature **412**, 52 (2001).

[18] V. A. Podolskiy, and E. E. Narimanov, Opt. Lett. **30**, 474 (2002).

[19] S. Shinohara, T. Harayama, T. Fukushima, M. Hentschel, T. Sasaki, and E. E. Narimanov, Phys. Rev. Lett. **104**, 163902 (2010).

[20] J. Yang, S.-B. Lee, S. Moon, S.-Y. Lee, S. W. Kim, T. T. A. Dao, J.-H. Lee, and K. An, Phys. Rev. Lett. **104**, 243601 (2010).

[21] L. Rayleigh, *The problem of the whispering gallery* (Cambridge University, Cambridge, UK, 1912)

[22] J. D. Jackson, *Classical electrodynamics* (Wiley, New York, 1962)

[23] H. C. van de Hulst, *Light Scattering by Small Particles* (John Wiley and Sons, New York, 1957)

[24] H. G. L. Schwefel, *Directionality and vector resonances of regular and chaotic dielectric microcavities.* PhD thesis, Yale University, 2004.

[25] J. Yang, *Free-space optical pumping based on ray and wave chaos in deformed microcavities* PhD thesis, Seoul National University, 2010.

[26] B. R. Johnson, J. Opt. Soc. Am. A **10**, 343 (1993).

[27] L. E. Reichl, *The trnasition to chaos in conservative classical systems: Quantum manifestations* (Springer-Verlag, New York, 1992).

[28] H. Schomerus and M. Hentschel, Phys. Rev. Lett. **96**, 243903 (2006).

[29] K. Artmann, Ann. Phys. (Leipzig) **8**, 270 (1951).

[30] J. Wiersig, J. Opt. A: Pure Appl. Opt. **5**, 53 (2003).

[31] I. Kosztin and K. Schulten, Int. J. mod. Phys. C **8**, 293 (1997).

[32] K. Husimi, Proc. Phys. Math, Soc, Jpn., **22**, 264 (1940).

[33] M. Hentschel, H. Schomerus and R. Schubert, Europhys. Lett., **62**, 636 (2003).

[34] J. Yang, S. Moon, S.-B. Lee, J.-H. Lee and K. An, Rev. Sci. Instrum., **77**, 083103 (2006).

[35] S. Moon, J. Yang, S.-B. Lee, J.-B. Shim, S.-W. Kim, J.-H. Lee and K. An, Opt. Exp. **16**, 11007 (2008).

[36] Lamb, *Hydrodynamics* (Dover, New York, 1945)

[37] A. J. Lichtenberg and M. A. Liebermann, *Regular and Stochastic Motion* (Springer, New York, 1983).

[38] O. Brodier, P. Schlagheck, and D. Ullmo, Phys. Rev. Lett. **87**, 064101 (2001)

[39] O. Brodier, P. Schlagheck, and D. Ullmo, Ann. Phys. (N.Y.) **300**, 88 (2002).

[40] A. M. Ozorio de Almeida, J. Phys. Chem. **88**, 6139 (1984).

[41] A. Mouchet, C. Eltschka and P. Schlagheck *et al.*, Phys. Rev. E **74**, 026211 (2006).

[42] S. Wimberger, P. Schlagheck, C. Eltschka and A. Buchleitner, Phys. Rev. Lett. **97**, 043001 (2006).

[43] M. Sheinman, S. Fishman, I. Guarneri and L. Rebuzzini, Phys. Rev. A **73**, 052110 (2006).

[44] S. Keshavamurthy, J. Chem. Phys. **122**, 114109 (2005).

[45] S. Keshavamurthy, Phys. Rev. E **72**, 045203(R) (2005).

[46] C. Eltschka and P. Schlagheck, Phys. Rev. Lett. **95**, 014101 (2005).

[47] C. Dembowski, H.-D. Gräf, A. Heine, R. Hofferbert, H. Rehfeld and A. Richter, Phys. Rev. Lett. **84**, 867 (2000).

[48] C. Dembowski, H.-D. Gräf, H. L. Harney, A. Heine, W. D. Heiss, H. Rehfeld and A. Richter, Phys. Rev. Lett. **86**, 78 (2001).

[49] S. Löck, A. Bäcker, R. Ketzmerick and P. Schlagheck, Phys. Rev. Lett. **104** 114101 (2010).

[50] D. A. Wisniacki, M. Saraceno, F. J. Arranz, R. M. Benito and F. Borondo, Phys. Rev. A **84** 026206 (2011).

[51] T. Takami, Phys. Rev. Lett. **68**, 3371 (1992).

[52] J. Wiersig, Phys. Rev. Lett. **97**, 253901 (2006)

[53] S.-B. Lee, J. Yang, S. Moon, S.-Y. Lee, J.-B. Shim, S. W. Kim, J.-H. Lee and K. An, Phys. Rev. A **80**, 011802(R) (2009).

[54] S.-B. Lee, J. Yang, S. Moon, S.-Y. Lee, J.-B. Shim, S. W. Kim, J.-H. Lee and K. An, Phys. Rev. Lett. **103**, 134101 (2009).

[55] J. Unterhinninghofen *et al.*, Phys. Rev. E **78**, 016201 (2008).

[56] http://www.exciton.com/pdfs/lds820.pdf

[57] S. Y. Kee, S. Rim, J. W. Ryu, T. Y. Kwon, M. Choi and C. M. Kim, Phys. Rev. Lett. **93**, 164102 (2004).

[58] T. Carmon, H. G. L. Schwefel, L. Yang, M. Oxborrow, A. D. Stone and K. J. Vahala, Phys. Rev. Lett. **100**, 103905 (2008).

[59] S. J. Min, *Study of a non-homogeneous transparent medium using the schlieren method*, master degree thesis, Konkuk University, 1982.

[60] P. A. Chinnery and V. F. Humphrey, Phys. Rev. E **53**, 272 (1996).

[61] P. A. Chinnery and V. F. Humphrey, J. Acoust. Soc. Am. **102**, 1383 (1997).

[62] L. E. Kinsler, *Fundamentals of acoustics* (Wiley, New York, 1982).

[63] V. Mallardo and M. H. Aliabadi, Int. J. Numer. Meth. Engng. **41**, 1527 (1998).

국문초록

비섭동계 기반 모드의 상호작용은 열린 비적분계 시스템에서 주요한 특징 중의 하나이다. 따라서 이러한 상호작용은 많은 관심을 불러일으켰으며, 변형된 미소 공진기에 시스템에서도 많이 연구되어왔다. 하지만 이전의 연구들은 대부분 상호작용의 결과에만 관심을 가졌을 뿐, 상호작용의 근간의 되는 물리 현상에 대한 연구는 상대적으로 적었다. 이 논문에서 우리는 공진 사슬에 의한 동적 터널링 이론을 변형된 미소 공진기 시스템에 적용하여 비섭동계 기반 모드들 간의 상호작용에 대해서 이해하고자 한다.

비대칭 공진기에서의 상호작용은 그 상호작용의 세기에 따라 정성적으로 강한 상호작용과 약한 상호작용의 두 가지로 분류할 수 있다. 강한 상호작용의 경우 상호작용하는 두 모드의 고유 진동수가 가장 가까워졌을 때의 후시미 함수는 위상 공간 상에서 안정된 혹은 불안정한 주기 궤도에 강하게 국소화 되어있다. 이는 강한 상호작용과 공진 사슬에 의한 동적 터널링 간의 연관성을 암시하는 것이다. 또한 강한 상호작용을 하는 모드들의 각 양자수의 차이는 연관된 공진 사슬 구조의 섬(island) 구조의 수의 정수배가 되는 것을 확인할 수 있었다. 이는 공진 사슬에 의한 동적 터널링 이론에서 예측되는 선택 규칙(selection ruel)이다.

또한, 공진 사슬에 의한 동적 터널링 이론은 연관된 상호직용의 세기가 위상 공간상에서의 공진 사슬 구조의 면적의 제곱에 비례할 것임을 예측하고 있다. 우리는 이러한 예측을 실험적으로 확인하고자 하였다. 이를 위하여 연속적으로 공진기의 변형도를 변화시킬 수 있는 액체 줄기 공진기에서 $l=2$ 와 $l=3$인 모드 그룹 사이의 교차 회피의 정도를 여러 변형도에 대하여 공진기에 의해 수정된 형광 분광학적 기술을 이용하여 측정하였다. 또한 수치 해석적인 방법을 이용하여 다

른 강한 상호작용에 대해서도 위와 같은 사실을 확인할 수 있었으며, 위상 공간 상에서 동일한 공진 사슬 구조와 연관되어있는 상호작용의 경우에 그 상호작용의 세기가 상호작용이 일어나는 고유 진동수와 비례한다는 사실을 알아냈다.

이러한 연구를 통해 공진 사슬에 의하여 유도되는 동적 터널링 이론을 실험적으로 실제 시스템에서 관측할 수 있었으며, 또한 상호작용의 고전역학적인 근본 원인을 확인할 수 있었다. 아울러 위상 공간 구조의 분석을 통해 구체적인 해밀토니안이 밝혀지지 않은 계에 대해서도 어느 정도 상호작용에 관한 정량적인 정보를 얻을 수 있게 되었다.

주요어: 변형된 공진기, 액체 줄기 공진기, 위상공간, 공진사슬에 의한 동적 터널링, 비섭동계 기반 모드의 상호작용

학번: 2006-20314